HOT-WIRE CHEMICAL
VAPOR DEPOSITION OF
POLYCRYSTALLINE SILICON

FROM GAS MOLECULE TO SOLAR CELL

HOT-WIRE CHEMICAL VAPOR DEPOSITION OF POLYCRYSTALLINE SILICON

FROM GAS MOLECULE TO SOLAR CELL

Polykristallijn silicium gedeponeerd met de
Hot-Wire CVD methode
Van gasmolecule tot zonnecel

(met een samenvatting in het Nederlands)

PROEFSCHRIFT

TER VERKRIJGING VAN DE GRAAD VAN DOCTOR AAN
DE UNIVERSITEIT UTRECHT OP GEZAG VAN DE RECTOR
MAGNIFICUS, PROF. DR. W. H. GISPEN, INGEVOLGE HET
BESLUIT VAN HET COLLEGE VOOR PROMOTIES IN
HET OPENBAAR TE VERDEDIGEN OP MAANDAG 28
OKTOBER 2002 DES VOORMIDDAGS TE 10.30 UUR

DOOR

Patrick Adrianus Thomas Theodorus van Veenendaal

GEBOREN OP 11 NOVEMBER 1973 TE HOUTEN

PROMOTOR: PROF. DR. R.E.I. SCHROPP
CO-PROMOTOR: DR. J.K. RATH

Faculteit Natuur- en Sterrenkunde
Universiteit Utrecht

There are no knowns.
There are things we know that we know.
There are known unknowns,
that is to say there are things we now know we don't know.
But there are also unknown unknowns,
things we do not know we don't know

Donald Rumsfeld

Music was my first love
And it'll be my last
Music of the future
And music of the past.
To live without my music
Would be impossible to do
'Cause in this world of troubles
My music pulls me through

Music - John Miles

Contents

Chapter 1

Introduction

1.1 Solar energy

Over the past decade, an increasing public awareness has arisen regarding the 'greenhouse-effect' and the role of fossil fuels in this effect. This notion, combined with the limited supply of fossil fuels, has led to an increase in the effort to investigate the use of renewable energy sources, such as wind, geothermal, tidal and solar energy. Despite the environmental advantages, at present, the contribution of these sources to the total energy consumption remains insignificant. In the year 2000, the contribution of renewable energy sources to the total electricity consumption in the Netherlands was 1.2% [1].

Comparing the above-mentioned renewable energy sources, the direct conversion of solar energy into electricity through photovoltaic (PV) solar cells is one of the most promising techniques. The yearly solar energy reaching the surface of the earth $(5.4 \times 10^{24}$ J) is more than ten thousand times the current energy demand of the world. Furthermore, the energy of four days sunshine corresponds to the total known global resources of oil, coal, gas and uranium together [2]!

The reason for the limited use of photovoltaic solar cells is the high cost of electricity produced by solar cells compared to electricity produced from fossil fuels. The major contributions to the cost of solar cells are the material and manufacturing costs. Therefore, over the past decades, the development of silicon based thin film solar cells has received much attention, because the

fabrication costs are low. Thin film solar cells use up to a factor of five hundred less semiconductor material and can be made with relatively low temperature processes, compared to 'wafer-based' cells. Furthermore, thin film silicon solar cells can be deposited on different low cost substrates (i.e. glass, stainless steel or plastics). At the moment, the most widely applied thin film silicon solar cells are made of amorphous silicon (a-Si:H). The main disadvantage of a-Si:H is the fact that the electronic properties degrade when the material is exposed to light: the so-called Staebler-Wronski effect [3]. This effect, although known for over three decades, is still one of the most important topics in amorphous silicon research. In order to avoid the Staebler-Wronski effect, new types of thin film silicon materials have been developed, such as protocrystalline (p-Si:H) [4], polymorphous (pm-Si:H) [5], microcrystalline (μc-Si:H) [5], heterogeneous (het-Si:H) [6] and polycrystalline silicon (poly-Si:H) [7].

1.2 Polycrystalline silicon

As was stated above, in the thin film silicon field, there are a number of known morphologies. These materials can be mostly classified by the amorphous fraction that is present in the layer. Schropp and Zeman [8] used the definitions as shown in Table 1.1 [7]. These definitions will also be used throughout this thesis.

From the middle of the 1990's, several groups have investigated the deposition of polycrystalline silicon thin films by different types of Chemical Vapor Deposition (CVD), such as Electron Cyclotron Resonance CVD (ECR-CVD) [9], Closed Chamber Cyclic CVD (CCC-CVD) [10], Plasma Enhanced CVD (PE-CVD) [11] and Hot-Wire CVD [12-15].

Table 1.1. Definitions for various morphologies of thin film silicon materials.

Identification	Symbol	Phases	Feature size
Hydrogenated amorphous silicon	a-Si:H	Single phase Amorphous	None
Hydrogenated microcrystalline silicon	μc-Si:H	two-phase amorphous and crystalline	<20 nm crystals
Hydrogenated polycrystalline silicon	poly-Si:H	Single phase crystalline with grain boundaries	>20 nm for the smallest crystal dimension
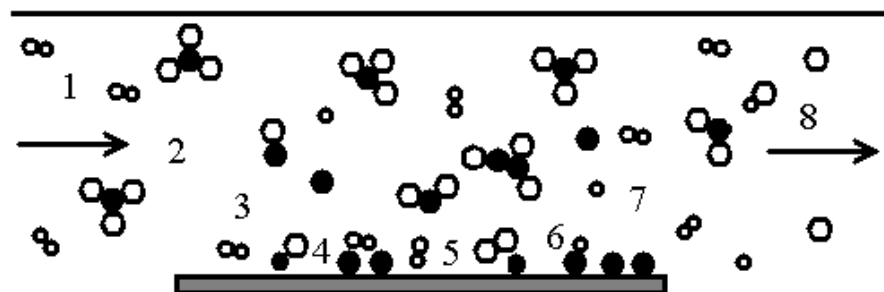
Figure 1.1 Elementary processes during CVD: 1 Supply of reactants; 2 Possible homogeneous reactions in the gas stream; 3 Diffusion of reactants to the substrate; 4 Adsorption and diffusion of reactants on the substrate; 5 Reactions at the substrate; 6 Desorption of reaction products from the surface; 7 Diffusion of reaction products from the substrate to the gas stream; 8 Removal of reaction products. Arrows denote direction of gas stream.

1.3 Chemical Vapor Deposition

The techniques listed above all have the abbreviation of CVD in their names, standing for Chemical Vapor Deposition. Chemical Vapor Deposition is a technique in which a solid material is deposited on a substrate through chemical reactions between gases. Many variants have been developed, which can be distinguished by the activation method (with heat, plasma or light), by the reaction circumstances (at low or atmospheric pressure), by the reactor type (hot or cold wall reactor) or by the nucleation type (homogeneous or heterogeneous).

In comparison to other thin film deposition techniques, such as Physical Vapor Deposition (PVD) e.g. sputtering or evaporation, CVD is probably the most complex. The complexity follows from the fact that, in general, the reaction takes place via intermediate reaction products, that the growth depends on numerous parameters, such as flow rates, reactant concentrations and temperature, and that the growth consists of multiple successive steps. The deposition rate is controlled by the kinetics, thermodynamics and by diffusion and convection controlled mass transfer. The main steps that determine the growth rate are shown in Figure 1.1.

1.4 Hot-Wire Chemical Vapor Deposition

A very promising new method to deposit silicon thin films is the Hot-Wire Chemical Vapor Deposition technique (Hot-Wire CVD). It was first introduced in 1979 and patented as 'thermal CVD' by Wiesmann [16,17].

Due to disappointing results Wiesmann et al. ceased to work on the subject further. In 1985, Matsumura introduced 'thermal CVD', described by Wiesmann, as 'catalytic CVD' (Cat-CVD) [18] for the deposition of fluorinated amorphous silicon. Mahan et al. [19] later introduced the term Hot-Wire Chemical Vapor Deposition (Hot-Wire CVD).

In Hot-Wire CVD, the reactant gases, i.e. silane (SiH_4) and hydrogen (H_2), are catalytically decomposed at the surface of a hot filament, with filament temperatures T_{fil} in the range from 1500-2000°C. The filament materials used most widely at present are tungsten (W) and tantalum (Ta) (see Chapter 3). The main advantages of Hot-Wire CVD over PE-CVD, which is currently the most applied technique to deposit thin silicon films in industry, are (i) absence of ion bombardment, (ii) high deposition rate, (iii) low equipment cost and (iv) high gas utilization (up to 80% [20]). Possible issues in Hot-Wire CVD are the control of the substrate temperature and aging of the filaments.
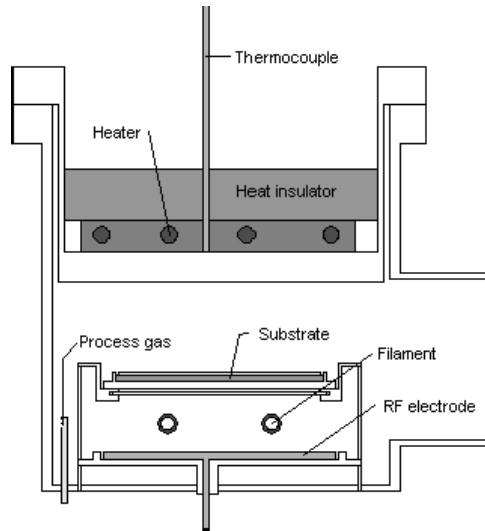
Figure 1.2 Cross-sectional view of Hot-Wire deposition chamber

With the Hot-Wire CVD technique, it is possible to deposit a wide variety of silicon morphologies and alloys, e.g. a-Si:H, µc-Si:H, het-Si:H, poly-Si:H and SiN_x, depending on the filament temperature, pressure, gas flows and substrate temperature. At Utrecht University, the main focus in Hot-Wire CVD is on the deposition of a-Si:H [21], poly-Si:H and SiN_x [22]. A cross-sectional view of a Hot-Wire deposition chamber is shown in Figure 1.2.

1.5 Aim and outline of this thesis

The subject of this thesis, as the title already indicates, is the deposition of polycrystalline silicon thin films by Hot-Wire CVD. The whole spectrum, from the reactions occurring at the hot filament to the application of polycrystalline silicon as absorber layer in solar cells, will be addressed.

Chapter 2 describes the deposition systems and characterization techniques that were used in the growth and study of the thin films. Chapter 3 starts with an overview of the research that has been performed so far on the deposition processes occurring in Hot-Wire CVD, from the decomposition of the reactant gases at the filament to the growth of the film. The second part of this chapter deals with XPS studies on filaments used in Hot-Wire CVD. Ellipsometry studies on the growth of polycrystalline silicon are described in Chapter 4. This chapter starts with a theoretical description of the technique, after which the focus shifts towards in-situ ellipsometry experiments, ending with real-time in-situ measurements during the growth of profiled polycrystalline silicon layers. Chapter 5 deals with a detailed characterization of polycrystalline silicon layers, deposited using tungsten, tantalum or rhenium as filament material. Finally, in Chapter 6 some preliminary solar cell results are presented.

Chapter 2

Experimental techniques

2.1 Deposition systems

2.1.1 PASTA

Most of the layers described in this thesis were deposited in the PASTA system (Process equipment for Amorphous Silicon Thin-film Application) [23]. Not only amorphous silicon, but a wide range of materials can be deposited in the system, such as a-SiGe, μc-Si:H, poly-Si:H and doped layers. The system consists of five process chambers and a load lock, centered on a cylindrical transport chamber. The main benefit of using a multi-chamber system is the minimization of the exchange of residual gasses and the use of a load lock prevents the central chamber from being exposed to air, thus reducing the pump down time and contamination of the layers with oxygen or water vapor. The substrates can be moved from one chamber to another by a transport system. All chambers have a background pressure of 10^{-8} mbar. Process chambers 1 through 3 are used for PECVD, while chamber 4 and chamber 5 are used for Hot-Wire CVD.
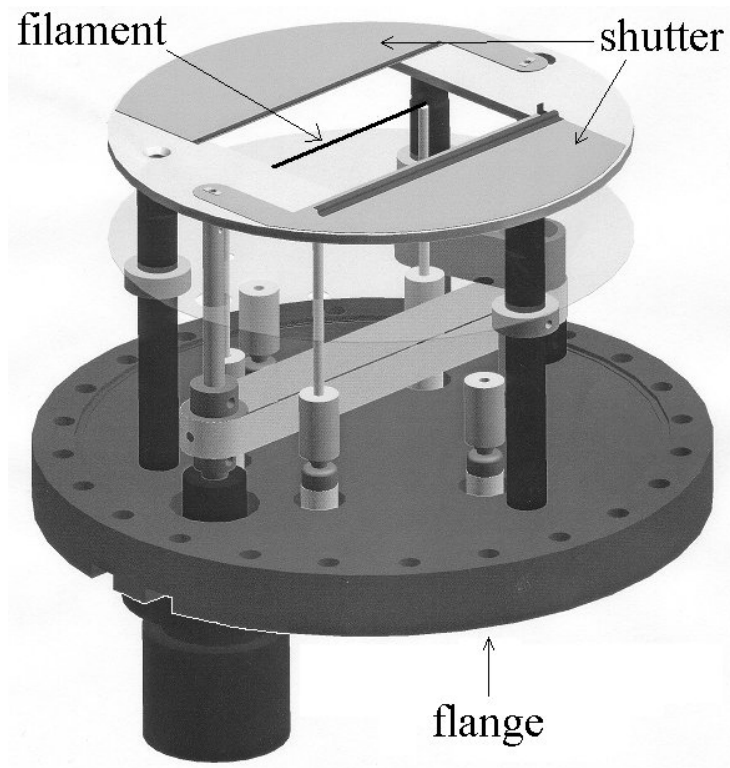
Figure 2.3 Hot-Wire assembly, designed by G.W.M. van der Mark

2.1.2 ATLAS

The ATLAS system was used to study the growth of the silicon thin films by kinetic and spectroscopic ellipsometry (see Chapter 4). It consists of two ultrahigh vacuum chambers, namely a loadlock and a reaction chamber. Originally, the ATLAS system was used for the deposition of a-Si:H films with PECVD [24], but for the purpose of the research described in this thesis, the lower r.f. electrode has been replaced by a Hot-Wire assembly, designed at Utrecht University. A schematic representation of this assembly is shown in Figure 2.1.

2.2 Characterization techniques

2.2.1 Ellipsometry

Ellipsometry is an optical technique for the characterization of, and observation of events taking place at, an interface or film between two media. It is based on the transformation of the polarization state of light when it is reflected or transmitted through the interface or film. A more thorough description of this technique will be given in Chapter 4.

2.2.2 X-ray Photoelectron Spectroscopy (XPS)

X-ray photoelectron spectroscopy (XPS) is a dedicated surface characterisation spectroscopy. It reveals the chemical composition at the surface and the chemical bound nature between the elements at the surface. XPS has been used to study the silicon content on the filaments used during deposition.

The sample is irradiated by X-ray photons, creating photoelectrons. These electrons can be detected if they have enough energy to reach the surface and leave the material. In XPS, the binding energy of the photoelectrons (E_b) can be calculated from the measured kinetic energy of the electrons (E_k) with

$$E_b = h\nu_{X-ray} - E_k - W , \qquad (2.1)$$

where $h\nu_{X-ray}$ and W are the photon energy of the used X-ray radiation and the work function of the used spectrometer, respectively.

The XPS data were obtained with a Vacuum Generators XPS system, using a CLAM-2 hemispherical analyzer for electron detection. Non-monochromatic $Al(K_\alpha)$ X-ray radiation was used for exciting the photoelectron spectra, using an anode current of 10 mA at 10 keV. The pass energy of the analyzer was set at 50 eV. The depth sensitivity of XPS is about 5 nm, so only the near-surface region is characterized.
The peak area A of the XPS spectra is given by

$$A \propto \rho\sigma\lambda_{mfp} \frac{1}{\sqrt{E_k}} , \qquad (2.2)$$

where ρ is the atomic fraction of the measured atom in the near-surface region, σ the photoelectric cross section and λ_{mfp} the inelastic mean free path of

Table 2.1 Atomic sensitivity factor (σ), inelastic mean free path of electrons (λ_{mfp}) and kinetic energy of electrons (E_k) for silicon, tantalum and tungsten.

Atomic orbital	σ [a.u.]	λ_{mfp} [Å]	E_k [eV]
Si (2p)	0.817	20.1	1384.6
Ta (4f)	8.62	20.6	1460.6
W (4f)	9.80	20.6	1451.6

electrons. The values for σ, λ_{mfp} and E_k are given in Table 2.1 for silicon (Si 2p), tantalum (Ta 4f) and tungsten (W 4f).

To compare the measurements performed on tungsten and tantalum, and to get a more quantitative value for the silicon fraction in the near surface area, the atomic ratio in the near surface region has to be calculated. This ratio can be derived from equation (2.2), resulting in

$$\frac{\rho_{Si}}{\rho_M} = \frac{A_{Si}}{A_M} \frac{\sqrt{E_{K,Si}}}{(\sigma\lambda_{mfp})_{Si}} \frac{(\sigma\lambda_{mfp})_M}{\sqrt{E_{K,M}}} = C_M \frac{A_{Si}}{A_M}, \tag{2.3}$$

where the subscript M denotes either tantalum (Ta) or tungsten (W) and C_M is a constant, which depends on the filament material. If the values for σ, λ_{mfp} and E_k, given in Table 2.1, are applied to equation (2.3), the values for C_{Ta} and C_W are 10.6 and 12.0, respectively.

2.2.3 Optical measurements

In order to determine the optical absorption coefficient α and the thickness of the layer d, reflection-transmission measurements (RT) have been performed. During these measurements the sample is irradiated with a photon beam (1.2-3.0 eV) and the reflection and transmission of that beam is measured as function of photon energy. Van den Boogaard [25] wrote a program to calculate α and d from the interference pattern. This program has been used in this thesis.

To determine the optical absorption coefficient in the low energy range (<1.2 eV), photothermal deflection spectroscopy (PDS) has been performed. The PDS setup has been described by Ullersma [26]. In general, the principle of PDS is the transformation of heat by the absorption of photons into a deflection of a laser beam. The absorbed energy is dissipated into a liquid, resulting in a gradient of refractive index. This causes the deflection of a laser beam (HeNe, λ = 632.8 nm) that passes near the sample surface. Jackson et al. [27] described the theory of PDS in detail and found the following relation between the optical absorption coefficient α and the deflection angle $\Delta\Phi$:

$$\Delta\Phi \propto L\frac{dn}{dT}I_0\alpha d \ , \tag{2.4}$$

with L, dn/dT, I_0 and d the width of the pumping beam spot, the change of the refractive index of the liquid with temperature, the pump beam intensity and the thickness of the sample, respectively. By measuring both the deflection of the probe beam at different pump beam wavelengths and the intensity of the pump beam, the relative absorption spectrum of the material is obtained. To transform this relative spectrum into an absolute spectrum, the PDS spectrum is matched to the RT spectrum.

To characterize the scattering behavior of the samples, angular resolved light scattering (ARLS) was used. With this method, the sample is irradiated by a HeNe laser beam ($\lambda = 632.8$ nm) and the transmission through as well as the reflection of the sample is measured using a photodiode that rotates around the sample, giving the angular-resolved scattering of the sample.

2.2.4 Electrical measurements

The electrical characterization consists of measuring the photo- and dark conductivity of the layers deposited. For this purpose, two silver electrodes with a length l of 20 mm at a distance w of 0.5 mm, have been deposited on the samples. The conductivity σ of the material is determined by:

$$\sigma = \frac{Iw}{Vld} \ , \tag{2.5}$$

where I, V and d are the measured current, the applied voltage (100 V) and the thickness of the film, respectively. If the measurement is performed in the dark, the dark conductivity σ_d is measured, while measuring under the solar simulator gives the photoconductivity σ_{ph}. The measurement of the dark conductivity is performed after annealing the sample at 160°C for one hour and cooling down to room temperature. If the conductivity is plotted as a function of temperature in a Arrhenius plot ($ln(\sigma)$ vs. $1/T$), the slope of this curve represents the activation energy for dark conductivity.

2.2.5 Raman spectroscopy

In order to determine the crystalline fraction of deposited layers, Raman spectroscopy has been performed. When light is incident on a sample, most of the light is scattered elastically (Rayleigh scattering). A small part of the light is scattered inelastically (Raman scattering). The inelastically scattered light has a different wavelength than that of the incident light and this difference

corresponds to the energy change within the material due to rotational or vibrational transitions, or both. A laser light beam is normally used as incident beam. The laser light thus scatters inelastically on phonons in the material, resulting in a shift in photon energy. This shift in photon energy corresponds to the energy of phonons that have been created or annihilated. The most interesting features that occur in silicon thin films are the transverse optic (TO) mode of amorphous silicon centered around 480 cm^{-1} and the TO-mode of crystalline silicon at 520 cm^{-1}. Furthermore, [28,29] the shoulder appearing at about 510 cm^{-1} is taken into consideration. This shoulder can be attributed either to a distribution of small grains or to grain boundary defects.

In order to calculate the crystalline volume fraction in the deposited layers, f_c, the method proposed by Brogueira et al. [30] has been used. In this method, the Raman spectra are fitted using three Gaussians, positioned at 480, 510 and 520 cm^{-1}. The crystalline volume fraction can than be calculated using:

$$f_c = \frac{A_{510} + A_{520}}{A_{480} + A_{510} + A_{520}},$$
(2.6)

where A_{480}, A_{510} and A_{520} are the areas of the different Gaussians. In this way, Raman spectroscopy provides information about the structural properties of the thin film silicon layers that have been deposited.

Raman measurements have been performed by using the 514.5 nm line of a Spectra Physics Ar$^+$-ion laser, a Spex triple-grating monochromator and a CCD-detector.

2.2.6 Fourier-Transform Infrared Spectroscopy (FTIR)

Information on the structural properties of the deposited films can be obtained using Fourier-transform infrared spectroscopy (FTIR). In the FTIR spectrum, several peaks occurs, due to vibrational modes of non-symmetric bonding configurations present in the film. The most important peaks considered in this thesis are the peaks at 2000 cm^{-1} and 2100 cm^{-1}. The 2000 cm^{-1} mode is the result of Si-H bonds located at compact sites [31], while the 2100 cm^{-1} mode is attributed to hydrogen on the surfaces of crystalline grains, commonly observed in case of PE-CVD polycrystalline silicon films [32].

A Digilab FTS-40 equipped with a liquid nitrogen cooled HgCdTe detector was used to measure the infrared transmission in the wavenumber range of 400 – 4000 cm^{-1} with a resolution of 2 cm^{-1}. For the purpose of FTIR measurements, samples have been deposited on polished highly resistive c-Si wafers. To analyze the FTIR spectra, a correction for multiple reflections in the substrate has been applied [33], as well as a correction for coherent reflections within the layer [34].

2.2.7 Time Resolved Microwave Conductivity (TRMC)

In order to measure the photoconductive properties of the deposited polycrystalline layers and of different regions within the polycrystalline layer, i.e. the mobility (μ) and lifetime (τ), the Time Resolved Microwave Conductivity (TRMC) technique has been utilized.

2.2.7.1 Historical background

In the late 1960's, the advantage of making a contact-free conductivity measurement using microwaves was recognized, since difficulties due to non-Ohmic contacts could in this way be eliminated [35]. Since then, TRMC has proven to be appropriate for studying the photoconductive properties of semiconductor powders [36], suspensions [37] and even thin layers [35,38-40]. Numerous studies on crystalline and amorphous silicon for photovoltaic applications have been carried out and even in-situ set-ups have been realized to monitor the material quality during the course of deposition [40,41]. More recently, TRMC investigations on microcrystalline and polycrystalline silicon have also been carried out [41-43].
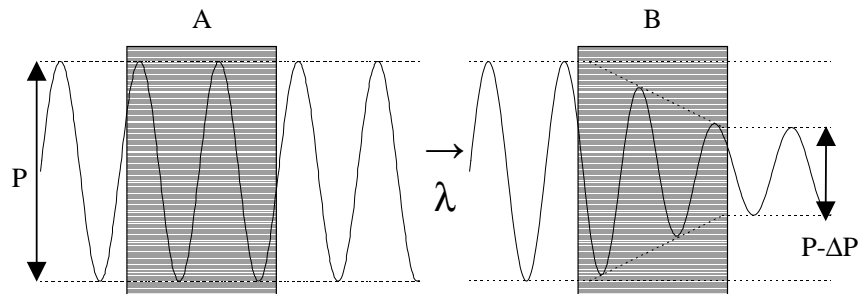
Figure 2.1 Schematical representation of interaction between microwave beam and semi-conducting material without (A) and with (B) laser irradiation. Microwave absorption by generated charge carriers results in change (ΔP) in reflected microwave power (P). λ represent the laser beam
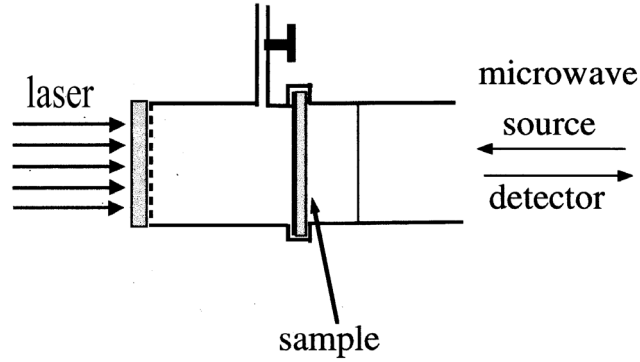
Figure 2.2 TRMC measurement cell.

2.2.7.2 TRMC principle

If a semi-conducting material is positioned in a microwave beam, the charge carriers generated upon laser irradiation absorb a part of the microwave power P. A schematic representation of this process is shown in Figure 2.1.

The change in reflected microwave power (ΔP) is related to the change in conductivity of the sample ($\Delta \sigma$) by the sensitivity factor A via

$$\frac{\Delta P}{P} = -A\Delta\sigma . \tag{2.7}$$

The A factor was calculated using the dimensions and the dielectric constants of the media present in the measurement cell. For the sample configuration shown in Figure 2.2, the calculated frequency dependence of A for a change in conductivity within the thin silicon layers used in the experiments is shown in Figure 2.3.

The A factor, was calculated using the dielectric constants of 1, 12 and 4.25 for air, poly-Si:H and Corning glass, respectively. The good agreement between the calculated frequency dependence of the A factor and the frequency dependence of experimental $\Delta P/P$ values is apparent.

The absolute value of the conductivity σ is related to the average concentration of negative and positive charge carriers, n_n and n_p, and their mobilities, μ_n and μ_p, by

$$\Delta\sigma = e(n_n\mu_n + n_p\mu_p) \tag{2.8}$$

with e the elementary charge. For $n_n = n_p = n$, equation (2.8) can be written as

$$\Delta\sigma = en\Sigma\mu , \tag{2.9}$$
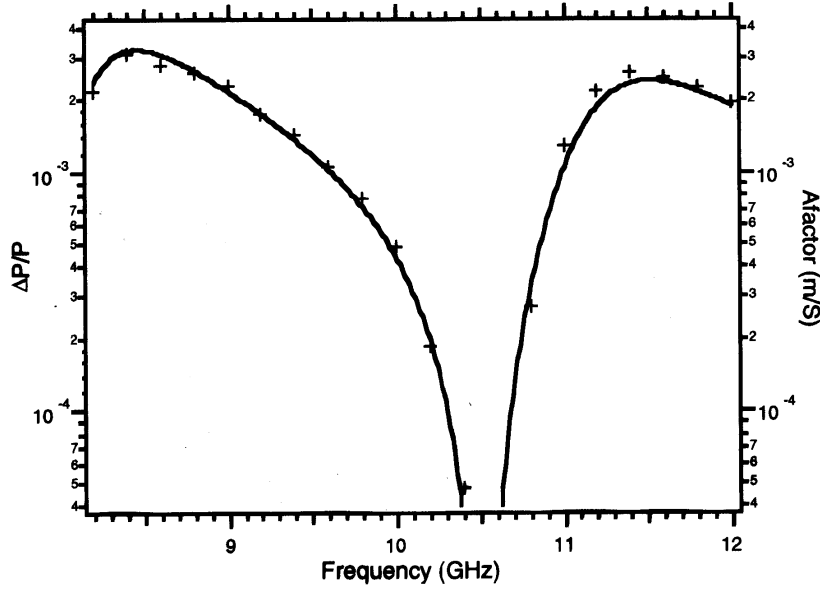
Figure 2.3 Frequency dependence of the fractional decrease in reflected microwave power (*ΔP/P*) of a 1.6 mm thick poly-Si:H film, deposited on Corning glass (+). The full line represents the calculated *A* factor. Courtesy of T.J. Savenije.

where $\Sigma\mu$ is the sum of the mobilities. The number of charge carriers formed per unit volume is proportional to the intensity of the incident light, I_0, the fraction of incident photons absorbed by the sample, (the attenuation, κ) and the efficiency for charge carrier generation, ϕ,

$$n = \frac{I_0 \kappa \phi}{L} \qquad (2.10)$$

where L is the thickness of the layer. By combining equations (2.9) and (2.10), the change in the measured conductivity can be related to the product of $\Sigma\mu$ and ϕ, by,

$$\Delta\sigma = \frac{e\phi\Sigma\mu I_0 \kappa}{L}. \qquad (2.11)$$

From equation (2.11), it can be derived that

$$\phi\Sigma\mu = \frac{\Delta\sigma L}{e I_0 \kappa} \qquad (2.12)$$

The attenuation by the sample, κ, at the laser pulse wavelength is given by

$$\kappa = 1 - \left(\frac{I_t + I_r}{I_0} \right) \quad\quad\quad (2.13)$$

where I_r and I_t are the intensities of the reflected and transmitted light, respectively.

Using equation (2.13), $\phi\Sigma\mu$ can be written as

$$\phi\Sigma\mu = \frac{\Delta\sigma L}{eI_0\left[1 - \left(\frac{I_t + I_r}{I_0} \right)\right]} \quad\quad\quad (2.14)$$

Thus, using equation (2.14), the mobility of the charge carriers can be calculated from the change in conductivity upon light excitation.

In order to determine the lifetime of the charge carriers, τ, it is essential to realize that the mobile charge carriers responsible for the conductivity are formed and decay on the timescale of the measurements. If no decay of the charge carriers occurs, $\phi\Sigma\mu$ would reach a constant value after the pulse, equal to $\phi_0\Sigma\mu$ with ϕ_0 the yield of charge carrier pairs per absorbed photon. However, charge carrier decay does occur and this decay has to be taken into account in order to determine the value of $\phi_0\Sigma\mu$. For this, a fitting procedure has been used which involves numerical integration of the differential rate equation for the charge carrier concentration, dn/dt:

$$\frac{dn}{dt} = \frac{\kappa\phi_0 I_0 \frac{d\left(\frac{I}{I_0}\right)}{dt}}{L} - \frac{n}{\tau}. \quad\quad\quad (2.15)$$

The term $d(I/I_0)/dt$ represents the temporal form of the intensity of the laser pulse, measured with a photodiode. Equation (2.15) assumes only single first order decay of the charge carriers with a mean lifetime τ. The transients calculated using (2.15) were convoluted with the 1 ns response time of the detection system.

2.2.7.3 TMRC measurements

For the TRMC measurements, the poly-Si:H samples with an area of 12 by 25 mm were positioned 36 mm from the back wall of the rectangular waveguide cell. The samples were irradiated with 3 ns pulses (FWHM) at 320 nm (3.87 eV), 500 nm (2.5 eV) and 690 nm (1.85 eV) of a Nd:YAG laser (Infinity, Coherent) equipped with an optical parametric oscillator. The incident intensity was measured using a pyroelectric power meter (LM-P5, Coherent). The beam

Table 2.2 XRD lines with accompanying peak position and lattice spacing

Diffraction line (hkl)	Peak position (2θ) [°]	Lattice spacing d [nm]
1 1 1	28.443	0.3136
2 2 0	47.303	0.1920
3 1 1	56.123	0.1637

was attenuated using metal-coated neutral density filters resulting in intensities ranging from 0.14 to 1000 μJ/cm^2.

The change in microwave power reflected by the cell on flash-photolysis was monitored using microwave circuitry and detection equipment with a resulting time response of ca 1 ns. The TRMC transients were averaged over 4 or 32 laser pulses.

2.2.8 X-ray diffraction (XRD)

X-ray diffraction has been used to study the orientation of crystallites present in the deposited films. The principle of X-ray diffraction (XRD) is the diffraction of a monochromatic X-ray beam on a crystal lattice structure. The diffraction is based on Bragg's law:

$$2d \sin \theta = \lambda_{X-ray}, \tag{2.16}$$

where d, θ and λ_{X-ray} are the lattice spacing, the angle of incidence and the X-ray wavelength, respectively. During an XRD measurement, the intensity of diffracted radiation is detected as function of 2θ. Here, the value of 2θ is varied from 10-60°. The used X-ray radiation is Cu Kα radiation, with a wavelength of 0.1542 nm. At angles where equation (2.16) complies, peaks will occur in the spectrum. These peaks represent a crystal orientation, present in the sample. A list of possible diffraction lines between 0-60° is listed in Table 2.2.

2.2.9 Solar cell characterization

The main, and most obvious, parameter that defines the quality of a solar cell is the conversion efficiency. This efficiency is defined as the ratio of the electrical output power to the optical input power. The optical input power used is the AM1.5 global spectrum, provided by a Wacom WXS-140-S solar simulator. The output power of the solar cell depends on the load.

In the cell, a number of losses can occur, e.g. pinholes, shunts and bad contacts. These losses are represented as the parallel and series resistance, R_p and R_s, respectively. Green [44] deduced that for a standard diffusion-type diode, the current density J depends on the voltage V according to

$$J = J_{ph} - J_0 \left(e^{\frac{e(V+JR_s)}{nkT}} - 1 \right) - \frac{V+JR_s}{R_p} , \qquad (2.17)$$

with J_{ph}, J_0 and n the photocurrent, the reverse-bias saturation current and the diode-ideality factor, respectively. From this equation, it follows that a high R_p and low R_s are beneficial for the performance of the device.

The performance of the solar cell is given by the open-circuit voltage V_{oc}, which is the voltage at zero current, the short-circuit current density J_{sc}, defined as the current density when the voltage equals zero, and the fill factor FF. This fill factor is defined as the ratio between the power density at the maximum power point P_{mpp} and the product of V_{oc} and J_{sc}:

$$FF = \frac{P_{mpp}}{V_{oc}J_{sc}} = \frac{V_{mpp}J_{mpp}}{V_{oc}J_{sc}} , \qquad (2.18)$$

where V_{mpp} and J_{mpp} are the voltage and current density at the maximum power point, respectively. If the power density of the incoming light P_{sol} is now taken into account, the conversion efficiency of the solar cell η is defined as

$$\eta = \frac{V_{oc}J_{sc}FF}{P_{sol}} \qquad (2.19)$$

The quantities V_{oc}, J_{sc}, FF and η are obtained by a measurement of the J-V characteristic of the solar cell under the above-mentioned solar simulator. This simulator provides an illumination intensity of 100 mW/cm^2. In order to define the cell area accurately, a mask was used during the measurements.

More detailed information about the solar cell performance can be obtained from the spectral response (SR) measurements. In this experiment the photocurrent due to a weak mdulated monochromatic probe beam is measured. From the measured photocurrent as a function of wavelength and voltage, $J_{ph}(\lambda,V)$, the external collection efficiency η_{col} is defined as

$$\eta_{col}(\lambda,V) = \frac{J_{ph}(\lambda,V)}{e\phi_{ph}(\lambda)} , \qquad (2.20)$$

where $\phi_{ph}(\lambda)$ is the incident number of photons per unit area per second at a wavelength λ on the cell.

When the SR measurement is performed under short-circuit conditions and an illumination intensity of about AM1.5, $\phi_{AM1.5}$, the short-circuit current density can be calculated using

$$J_{sc} = e\int \eta_{col}(\lambda)\phi_{AM1.5}(\lambda)d\lambda \qquad (2.21)$$

Both values of J_{sc}, calculated either from *J-V* or SR measurements, can be compared and from this comparison bottleneck-locations for the current collection can be determined.

Chapter 3

Deposition processes
in Hot-Wire CVD

3.1 Introduction

In this chapter an overview of studies regarding the different steps in the deposition and growth of silicon thin films in Hot-Wire CVD (i.e. gas decomposition, evaporated radicals, gas phase reactions and film growth) will be given. Also, the results of X-ray photoelectron spectroscopy measurements of the silicon content on the surface of the filaments used in Hot-Wire CVD will be described.

3.2 Deposition of silicon by Hot-Wire CVD

In this section, an overview of the research that has been performed by various groups around the world on the reactions that are occurring in Hot-Wire CVD (at the filament surface, in the gas phase and at the film surface) will be reviewed.

3.2.1 Filament materials

Presently, the filament materials most used are tungsten (W) and tantalum (Ta). Besides these materials, Matsumura reported on the use of molybdenum (Mo), vanadium (V) and platinum (Pt) as filament material [45]. The main conclusions of this study, with respect to the filament material, were that the film properties were independent of the filament material, but dependent on the filament temperature. More recently, Duan et al. [46] used rhenium (Re) as filament material, mostly to study the gas phase reactions occurring and the gas species produced in Hot-Wire CVD. Finally, Morrison et al. [47] reported on the deposition of microcrystalline silicon using graphite as catalyzer.

3.2.2 Decomposition at the filament surface

In 1988, Doyle et al. performed one of the first investigations on the decomposition of silane at a hot tungsten filament [48]. This investigation resulted in a linear relationship between the film growth rate (G) and the decomposition efficiency (α_d). In 1991, Horbach et al. [49] found a similar relationship as Doyle, but in a higher temperature range. At a filament temperature $T_{fil} < 1800°C$ the logarithms of both the decomposition coefficient and the growth rate are proportional to $1/T_{fil}$). At $T_{fil} > 1800°C$ they both saturate. This saturation is explained by complete silane decomposition. The dissociation of silane on a hot tungsten surface has been investigated by Tonokura et al. [50]. From this study, it followed that silane dissociates to give H and Si atoms through the following successive surface dissociation reactions: $SiH_4 \rightarrow SiH_3 + H \rightarrow SiH_2 + 2H \rightarrow SiH + 3H \rightarrow Si + 4H$. It was found that the activation energy for Si atom production is about 234 kJ/mol for the tungsten filament. This activation energy is much lower than the energy required for direct bond breaking in order to remove Si from the metal surface. For example, the bond dissociation energy of Si from the tungsten (100) surface is estimated to be about 535 kJ/mol [51]. This low activation energy leads to the conclusion that the process is catalytic of nature.

The decomposition probability of one SiH_4 molecule by one collision with the hot filament (α_d) has been determined by Honda et al. [20]. This value is derived from both the number of silane molecules colliding with the catalyzer surface and the number of deposited silicon atoms. The number of colliding silane molecules per unit time, Γ, is described as

$$\Gamma = \tfrac{1}{4} \rho v \pi D_{fil} L , \tag{3.1}$$

where ρ, v, D_{fil} and L are the density of silane molecules, the mean thermal velocity of the molecules, the diameter of the filament and the length of the

filament, respectively. The number of deposited silicon atoms per unit time, G, is described by

$$G = dN_A \pi D \int f(x)dx / M_{Si} .$$ (3.2)

Here, d, N_A, D, $f(x)$ and M_{Si} are the density of a-Si:H, Avogadro's number, the diameter of the reactor tube, the measured deposition rate and the atomic weight of silicon, respectively. The efficiency of gas use for silane, Λ, is given by

$$\Lambda = \frac{G}{F} ,$$ (3.3)

where F is the number of supplied silane molecules per unit time. The number of collisions on the catalyzer surface by one molecule, A, is described by

$$A = \frac{\Gamma}{F} .$$ (3.4)

It was found that a silane molecule collides 0.2 to 2 times with the catalyzer surface. The derived relation between the gas use efficiency Λ and the silane decomposition probability α_d is

$$1 - \Lambda = (1 - \alpha_d)^4 .$$ (3.5)

The value for α_d at a filament temperature T_{fil} of 2000°C is about 40%.

3.2.3 Evaporated radicals

At sufficiently high filament temperature, the silane is thus fully cracked into one Si and four H atoms. Only at temperatures below 1700K, SiH_2 and SiH_3 could be detected [52]. It is suggested that in this temperature regime, a Si/W alloy is formed on the filament [53]. It is presumed that this alloy affects the decomposition of silane at the filament surface. Matsumura also found that at filament temperatures above 1700K, the major species desorbed from the filament is the Si atom. The maximum production of Si atoms is observed at about 1800K. These results were obtained with W, Mo and Ta filaments. The Si atom is the only major species above T_{fil} = 1700K for all three filaments. The temperature dependence below T_{fil} = 1700K is large and different for these three filaments. Activation energies for Si atom desorption from the filament below 1700K are found to be (251±63), (96±25) and (71±20) kJ/mol for Mo, Ta and W filaments, respectively [52]. Another important observation reported by Inoue et al. [52] is the fact that the dilution of the silane gas with hydrogen does not change the signal intensities of Si, SiH_2 and SiH_3. It seems that H_2 has no effect on the catalytic decomposition processes of SiH_4.

3.2.4 Gas phase reactions

At low pressures ($<$ 5 µbar), the Si and H atoms that come from the filament thermally diffuse to the substrate [20], with minor to no gas phase reactions. Duan et al. reported on single photon ionization mass spectrometry measurements on 1.8 x 10^{-2} µbar at W filament temperatures of 1950°C [54]. The major silicon containing gas species detected is Si, with minor contributions of SiH_3 and Si_2H_x. However, these pressures are several orders lower than the pressures used during actual silicon deposition, e.g. the pressure used during the depositions described in this thesis is 0.1 mbar.

At higher pressures ($>$ 5 µbar), the silicon atom is highly reactive. It can abstract an H atom from silane, resulting in SiH and SiH_3, or it can insert into a Si-H bond [55]. Molenbroek described three possible insertion reactions, namely:

$$Si + SiH_4 \rightarrow SiH + SiH_3 \, , \tag{3.6}$$

$$Si + SiH_4 \rightarrow HSiSiH_3 * \text{ and} \tag{3.7}$$

$$Si + SiH_4 \rightarrow 2SiH_2 \, . \tag{3.8}$$
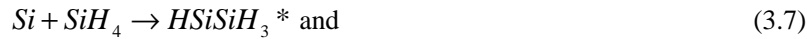
Because the first and third reactions are endothermic, they are unlikely to occur. $HSiSiH_3$ is formed through an exothermic reaction and will thus be the most probable species to exist. The formation reaction of $HSiSiH_3$ has been the subject of ab-initio molecular orbital calculations by Sakai et al. [56]. According to these calculations, triplet Si atoms as well as singlet Si atoms react with SiH_4 to yield $HSiSiH_3$. Since Si atoms produced at the hot filament should be triplets, the formation reaction is spin forbidden if $HSiSiH_3$ is in singlet manifold. There are two possibilities: (i) singlet $HSiSiH_3$ is produced by the non-adiabatic reaction pathway from $Si(^3P)$ + SiH_4 triplet surface, or (ii) triplet $HSiSiH_3$ is generated but it is relaxed to singlet manifold by collisions with a third body. It follows, that $HSiSiH_3$ is unstable and that it will react with SiH_4 in the gas phase. There are three possible reactions, namely [52]:

$$HSiSiH_3 + SiH_4 (+M) \rightarrow Si_3H_8 (+M) \tag{3.9}$$

$$HSiSiH_3 (+M) \rightarrow H_2SiSiH_2 (+M) \tag{3.10}$$

$$HSiSiH_3 + SiH_4 \rightarrow SiH_2 + Si_2H_6 \tag{3.11}$$
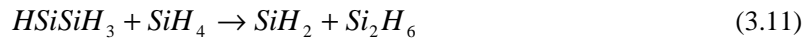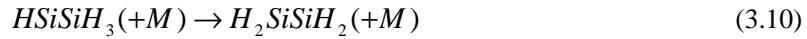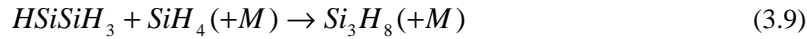
In reactions (3.9) and (3.10), M stands for a third body (e.g. an atom or molecule). Up to now, no Si_3H_8 has been detected. Therefore, Inoue et al. suggest that reaction (3.9) can be neglected. However, Molenbroek suggests that abstracting H_2 from the Si_3H_8 molecule forms Si_3H_6 [55]. The reaction product of reaction (3.10), H_2SiSiH_2, is a rather stable closed shell molecule and it has been expected to be an important precursor species for the film growth. In

the experiments described by Inoue et al. [52], the most prominent species detected is Si_2H_6. They suggested that SiH_2, produced via reaction (3.11), further reacts with SiH_4, according to

$$SiH_2 + SiH_4(+M) \rightarrow Si_2H_6(+M).$$ (3.12)

The presence of atomic hydrogen in the reactor, results in the occurrence of the following reaction:

$$H + SiH_4 \rightarrow SiH_3 + H_2.$$ (3.13)

The SiH_3 species does not react with SiH_4 and the only gas phase reaction of SiH_3 is self-recombination.

Gallagher also proposed a gas phase growth reaction, in which Si atoms react with silane [57]:

$$Si + SiH_4 \rightarrow Si_2H_4^* \rightarrow$$
$$2SiH_2 , SiH + SiH_3 , Si_2H_2 + H_2 , Si_2H_4 ,$$ (3.14)
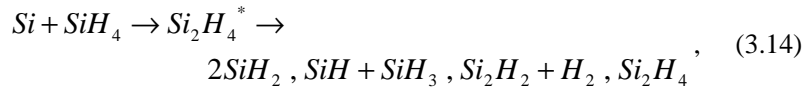
where $Si_2H_4^*$ is an unstable intermediate. Some of the reaction products will react with silane to produce more stable silanes, such as Si_2H_6 and Si_3H_6.

From a theoretical point of view, the main gas phase reaction species are thus: SiH_3, Si_2H_6, Si_3H_6 and H_2SiSiH_2. It is expected that the detection of the actual gas phase reaction species will take place in the near future.

3.2.5 Film growth

Although Matsumura concluded that the deposition process in Hot-Wire CVD is very different from that in both the conventional thermal CVD as well as in PECVD [45], Gallagher is convinced that the models used in PECVD as well as in HWCVD should be about the same [57]. The film surface will be mostly H covered, with approximately the same ratio R between the amount of dangling (Si-) and hydrogen passivated bonds (Si-H) as in the vapor. There, this ratio is $n_{radical}/n_{silane}$. This follows from the fact that the most frequent gas-surface collisions are with SiH_4, since silane is the most abundant gas in the reactor. This dynamic equilibrium reaction is given by:

Table 3.1 Reported values of surface reaction probability β

Species	β
RF-PECVD	
Si	1 [58]
SiH	1 [58]
SiH_2	0.6±0.2 [59]
SiH_3	0.1-0.4 [60-62]
Hot-Wire CVD	0.29-0.54 [63]

$$Si- + SiH_4 \leftrightarrow Si-H + SiH_3 \qquad\qquad (3.15)$$
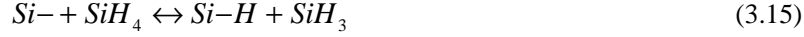
and leads to $R \approx n_{radical}/n_{silane}$. Typical values for $n_{radical}/n_{silane}$ are 10^{-4}-10^{-3}, so a similar value is expected for R. This leads to dangling bonds at an average spacing of 30-100 surface sites, or 5-15 nm. In order to grow a compact film it is necessary to overcome the tendency for the incident radicals to strike film-surface peaks more frequently than valleys. This requires not only radical diffusion over distances in excess of dangling bond separations, but also an increased affinity for settling onto valleys. Following radical-film Si-Si bonding, H_2 evolution occurs from the reaction

$$Si-H + Si-H \rightarrow Si-Si + H_2 , \qquad\qquad (3.16)$$

within the top few atomic layers of the film.

One very fundamental difference between radio frequent (RF) PECVD and Hot-Wire CVD was however disregarded by Gallagher, namely the absence of ions in Hot-Wire CVD. These ions are very important in RF-PECVD. They are essential in creating a dense a-Si:H network [64], have a significant contribution to the growth rate [64] and determine the properties of thin film silicon to a large extent [65,66]. A way to compare the two deposition techniques is to study the surface reaction probability, β. A number of groups have reported on values of β for different species and these values are listed in Table 3.1. In the Hot-Wire CVD case, the lower value was determined for the deposition of a-Si:H, while the higher value was found for μc-Si:H deposition. The difference in β between RF-PECVD and Hot-Wire CVD can have two causes [63]: (i) a different radical responsible for the growth or (ii) a changing reactivity of the surface. The first effect follows from the abundance of atomic H present in the reactor, leading to stripping of SiH_x. Furthermore, the pressure in PE-CVD is higher, resulting in more gas phase reactions. The latter effect is related to the presence of a physisorbed hydrogen layer at the surface of the growing silicon layer, as suggested by Matsuda et al. [61]. Radicals arriving at the surface will recombine with the physisorbed hydrogen, resulting in a high

Table 3.2. Reactions of Si, H and SiH_3 on the surface. Subscript (s) refers to a radical bonded to Si in the film. Abbreviation d.b. stands for dangling bond.

$$Si + SiH_{(s)} \rightarrow SiSiH_{(s)} = SiH_{(s)} + 2d.b. \qquad (3.17a)$$

$$H + SiH_{(s)} \rightarrow H_2 + d.b. \qquad (3.17b)$$

$$SiH_3 + d.b. \rightarrow SiH_{3(s)} \qquad (3.18a)$$

$$Si + d.b. \rightarrow Si_{(s)} + 3d.b. \qquad (3.18b)$$

$$H + d.b. \rightarrow SiH_{(s)} \qquad (3.18c)$$
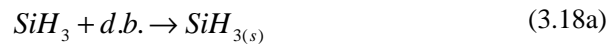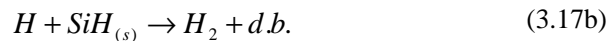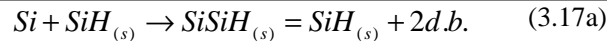
surface reaction probability. The large contributions of ions in RF-PECVD [63] will remove this layer, resulting in a lower β. Because there are no ions present in the gas phase during Hot-Wire CVD, it is likely that such a physisorbed hydrogen layer exists. This layer will then be responsible for the high surface reaction probability in Hot-Wire CVD.

Molenbroek investigated the reactions that can occur at the surface [55]. These reactions are listed in Table 3.2. Reaction (3.17a) and (3.17b) involve the reactions of Si and H with a hydrogen passivated surface, while reactions (3.18a) and (3.18b) deal with the direct reaction of SiH_3, Si and H with a dangling bond.

Reactions (3.17a) and (3.18b) result in the creation of two new dangling bonds. This means that whether Si reacts with a dangling bond or a Si-H bond, two new dangling are created in the process. If there are enough dangling bonds formed, it is possible for them to react with each other to form Si-Si bonds. Hydrogen atoms will either abstract a H to create a dangling bond (3.17b), or passivate a dangling bond (3.18c). A dangling bond can also be passivated by SiH_3 (3.18a).

Nozaki et al. [67] performed laser induced fluorescence (LIF) measurements and found that Si is the film growth precursor at low pressures (10^{-2} µbar). At higher pressures, gas phase reactions lead to a different growth precursor. Two of the proposed candidates are disilene (Si_2H_4) and SiH_3.
In summary, the most likely growth precursors are Si, SiH_3 and Si_2H_4, depending on the pressure and filament temperature.

3.3 XPS studies on the filament surface

As was already mentioned earlier, one of the possible issues in Hot-Wire CVD is the aging of the filament, which can lead to filament failure. This aging is attributed to the decomposition of silicon on the filament or the formation of a silicide-like alloy on the filament surface. In this section, the results of the XPS studies performed on different filament surfaces will be described and discussed. These measurements have been performed in order to study the silicon content on the filaments used during deposition.

3.3.1 Filament temperature

Figure 3.1 shows the filament temperature T_{fil} as function of the current through the filament I_{fil} [68], as measured in vacuum in chamber 4 of the PASTA system for filaments with a diameter of 0.5 mm. From this figure, it follows that there is a linear correlation between the filament temperature and the filament current for all three materials used namely tungsten (W), tantalum (Ta) and rhenium (Re). These correlations are also shown in Figure 3.1.

3.3.2 XPS measurements on filament surface

To study the influence of the catalytic properties of the filament material on the growth of polycrystalline silicon thin films, different wire materials have been used, namely tungsten (W) and tantalum (Ta). X-ray Photoelectron Spectroscopy (XPS) was performed on used filaments to determine the difference in the silicon coverage of the filaments. Also, Scanning Electron Microscopy (SEM) has been performed on end-of-lifetime filaments.
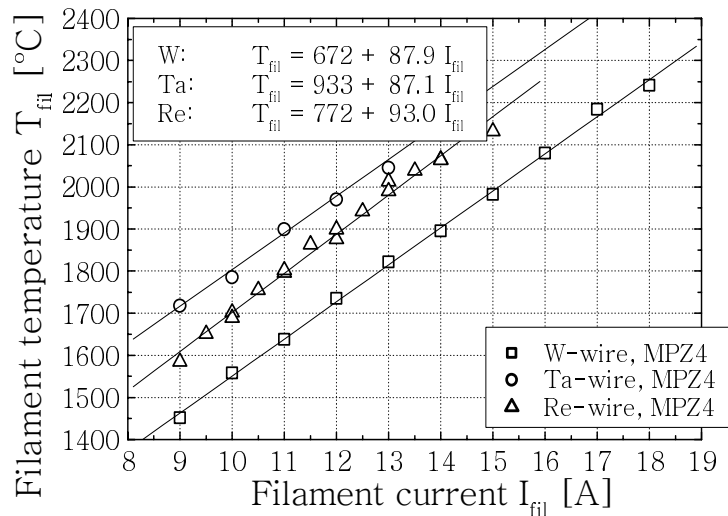

Figure 3.1. Filament temperature T_{fil} as function of filament current I_{fil}
(measured by C.M.H. van der Werf)

Table 3.2. Deposition parameters
(1 sccm = 0.0017 Pa m³/s = 4.48 x 10^{17} gas particles/s [69])

Parameter	Value
ΦSiH_4	10 sccm
ΦH_2	150 sccm
T_{fil}	1900°C
P	100μbar

The tungsten filaments were used for 10, 75, 90 and 180 minutes, while the tantalum filaments were used for 90 and 180 minutes. Each deposition started with a pristine wire, i.e. a wire that has been annealed in vacuum during 3 hours. The deposition parameters used (silane flow ΦSiH_4, hydrogen flow ΦH_2, filament temperature T_{fil} and pressure p) are listed in Table 3.2.

The measurements were performed either position or deposition time dependent. The results will be described below.

3.3.2.1 Position dependent measurements

To study the position dependence of the silicon content in the near-surface region of the filament, measurements have been performed on the center part and the outer ends of the filament.

The deposition time was 90 minutes and the deposition started with a pristine wire. From the measured XPS spectra, the areas of the Si(2p)-, W(4f)- and Ta(4f)-peaks were determined. Using equation (2.3), the atomic ratios in the near surface region were calculated. These calculated values are given in Table 3.3.

From the values of ρ_{Si}/ρ_M given in Table 3.3, it follows that the difference between the middle and the edge of the tungsten filament is much larger than in the case of a tantalum filament. The lower filament temperature at the edges causes the higher silicon content at the edge of the tungsten wire, compared to the middle. At filament temperatures below 1500°C, there is an

Table 3.3. Calculated values for the atomic ratio in the near surface region (ρ_{Si}/ρ_M) from position dependent XPS spectra for different filament materials (M).

M	Position	ρ_{Si}/ρ_M
Ta	Center	1.43 [70]
Ta	Outer ends	1.61 [70]
W	Center	2.08 [71]
W	Outer ends	4.47 [71]

increased silicide formation, leading to changes in resistance and degradation of the wire [72,73]. The much smaller difference in silicon content between the middle and edges of the tantalum filament implies that the formation of a silicide-like compound is less temperature dependent than in the case of tungsten.

3.3.2.2 Deposition time dependent measurements

In order to study the deposition time dependence of the silicon content in the near-surface region of the filaments, a deposition series was made in which the deposition times ranged from 0 to 180 minutes at standard polycrystalline silicon deposition conditions, using both tantalum and tungsten as filament material. Every filament used has been pre-annealed in vacuum for 3 hours. This pre-annealed filament was used as a reference, to see if silicon is present on the filaments prior to deposition. The XPS measurements have been performed on the center part of the filament. The values for the silicon content in the near-surface region of the filaments (ρ_{Si}/ρ_M), calculated from the measured XPS spectra, as a function of the deposition time and for different filament materials, are given in Table 3.4 and Figure 3.2. From Table 3.4 and Figure 3.2, it can be concluded that the silicon content in the near surface region

Table 3.4. Calculated values for the atomic ratio in the near surface region (ρ_{Si}/ρ_M) from deposition time (t_{dep}) dependent XPS spectra for different filament materials (M).

| M	t_{dep} (min.)	ρ_{Si}/ρ_M
Ta	0	0
Ta	90	1.43
Ta	180	1.12
W	0	0
W	10	0.60
W	75	1.24
W	90	2.08
W	180	4.15
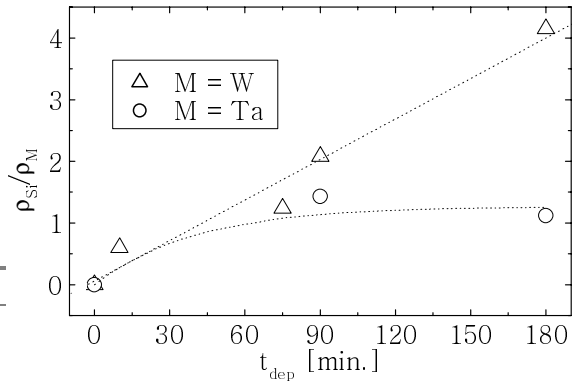
Figure 3.2. Silicon content in the near-surface region of the filament (ρ_{Si}/ρ_M) as a function of deposition time (t_{dep}), for different filament materials (M). The lines are guides to the eye.

of the tungsten filament increases linearly with time and does not saturate in this time frame, while this value on the tantalum filament saturates rather quickly.

3.3.2.3 Comparison of Ta- and W-filaments

From the results shown in Figure 3.2 and Table 3.4, it is clear that the silicon content in the near-surface region of the filament is larger in the case of a tungsten filament as compared to a tantalum filament. Two processes can be suggested: (1) the time scales for the catalytic dissociation of the reactant gases is different at a tantalum surface, compared to a tungsten one, and (2) the formation of a silicide-like alloy is inhibited more on the surface of the tantalum filament than on a tungsten filament. However, the reactions taking place at the filament described earlier in this chapter lead to the conclusion that the dissociation reactions at the filament is largely filament temperature dependent, but not depending on the filament material. The second suggested process is therefore the most likely. This is also confirmed by Duan et al. [74]. Scanning electron microscopy performed on tantalum and tungsten filaments supports this. The resulting micrographs are shown in Figure 3.3.

The most striking feature in Figure 3.3 is the presence of a different morphology at the surface of the tungsten filament. Such a layer is not present on the surface of the tantalum wire. The phase present in the surface layer, resulting in a different morphology at the surface compared to the core, is most probable resulting from the reactions taking place at the filament surface. Figure 3.3 also shows the difference in filament morphology between the tungsten and tantalum. The tungsten filament is dense, while the tantalum one is porous. It is likely that this difference in filament morphology has influence on the reactions taking place at the filament.
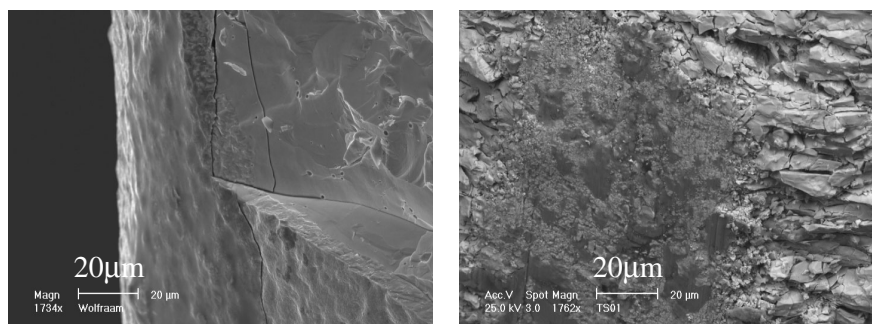

Figure 3.3. Scanning electron micrographs of W (left) and Ta (right) filament

3.3.2.4 Filament failure

A major disadvantage of using tungsten as filament material is the fact that these filaments have a rather short lifetime. Under standard polycrystalline deposition conditions, the filaments have to be cleaned at high temperature after about one hour of deposition, in order to remove the silicon/silicide that is present on the filament. Combining the results of the XPS measurements performed on the filaments with the phase diagrams of Si-Ta and Si-W (Figure 3.4), an indication for the failure mechanism of W filaments can be made. In order to compare the XPS results with the phase diagram, the values for ρ_{Si}/ρ_M have to be converted to ratios of mass. This is achieved by multiplying the calculated value of ρ_{Si}/ρ_M by the ratio of the atomic masses of silicon and tantalum, or silicon and tungsten. With this method, it is assumed that the silicon content in the near-surface region of the filament is homogenous.

The largest measured values of ρ_{Si}/ρ_W and ρ_{Si}/ρ_{Ta} are 4.2 and 1.6, respectively. Converting these values to mass percentage results in silicon mass percentages on the surface of the Ta and W filaments of 20% and 40%, respectively. From Figure 3.4, it follows that if a tungsten filament is kept at a temperature of 1900°C, and the filament has a silicon mass percentage of 40%, a liquid phase can occur. Ruihua et al. [75] has also suggested the occurrence of this liquid phase. The presence of a liquid phase will increase the tension in the filament, due to a decrease in surface area. It is also possible that the liquid phase corrodes the filament. In the tantalum case, this is less likely.
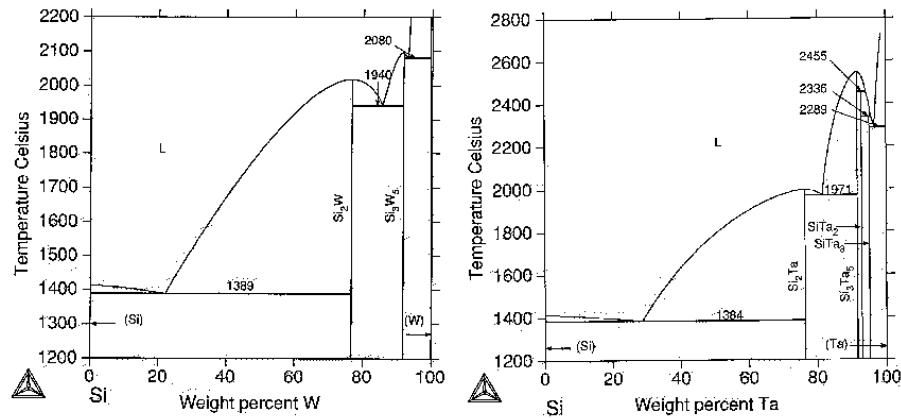

Figure 3.4 Phase diagrams of Si-Ta and Si-W [76]

3.4 Conclusions

In this chapter an overview of studies regarding the different steps in the deposition and growth of silicon thin films in Hot-Wire CVD has been given. Studies on the decomposition of silane on the filament indeed showed that the process is catalytic of nature. Also, it was shown that the growth rate is proportional to the decomposition probability. This decomposition probability is ~40% at a filament temperature of 2000°C. At filament temperature above 1800°C, silane is decomposed into Si and 4H. At lower filament temperatures, also SiH_2 and SiH_3 have been detected as decomposition products. The dominant gas phase reactions are the reaction of Si and H with silane, resulting in SiH_3, Si_2H_6, Si_3H_6 and H_2SiSiH_2. The precursors dominating the film growth are Si, SiH_3 and Si_2H_4, depending on pressure and filament temperature. Numerous groups around the world are expanding their research activities in this field.

Furthermore, XPS measurements have been performed on tantalum and tungsten filaments used during the deposition of thin film poly-Si:H. Measurements at various positions along the length of the filament show larger silicon contents at the ends of the tungsten filament, as compared to the middle. The lower filament temperature causes this. In contrast, the difference in silicon content between the middle and edge of the tantalum filament is insignificant. Deposition time dependent measurements show an increase in silicon content of the tungsten filament with time, while the silicon content on the tantalum filament saturates rather quickly. Two processes are suggested as an explanation for these significant differences between W and Ta: (1) the catalytic dissociation of the reactant gases at a tantalum surface is different from that at a tungsten surface, and (2) the formation of a silicide-like alloy is inhibited more on the surface of the tantalum filament than on a tungsten filament. From the W-Si and Ta-Si phase diagrams follows that silicide-like alloys can occur with melting temperatures as low as 1400°C. However, these low-melting phases occur at very high Si percentages. After combining the XPS measurements with the Ta-Si and W-Si phase diagrams, it can be concluded that the presence of a liquid phase is more likely to occur in the case of a tungsten filament. Whether or not this liquid phase is present is unclear.

Chapter 4

Ellipsometry studies

4.1 Introduction

Ellipsometry is an optical technique for the characterization of interfaces or films and observation of events taking place there. It is based on the transformation of the polarization state of light when it is reflected at or transmitted through the interface or film. Two factors make ellipsometry particularly attractive: (1) its essentially non-perturbing character, hence its suitability for in-situ measurements, and (2) its remarkable sensitivity to minute interfacial effects. The term ellipsometer, from which the technique of ellipsometry derives its name, was first used by Rothen [77] to denote an optical instrument for the measurement of thin surface films by the reflection of polarized light.

In this chapter, the theoretical background, working principle and results of the ellipsometry studies performed are given.

4.2 Theoretical background

As the name already suggests, the ellipsometry technique is based on the elliptical polarization of a light wave. The elliptical polarization is the most

general state of polarization of a strictly monochromatic light wave. For a complete specification of the ellipse, the following features of the ellipse have to be known: (i) the orientation in space of the plane of the ellipse of polarization, (ii) the azimuth, ellipticity and handedness of the ellipse in that plane, (iii) the amplitude of the ellipse and (iv) the absolute temporal phase. The azimuth is the angle between the major axis of the ellipse and the positive x-direction. The ellipticity is the ratio of the length of the major and the minor axis of the ellipse. The handedness determines the sense in which the ellipse is described (clockwise or counter-clockwise). Generally, the handedness is incorporated in the definition of the ellipticity. It is positive for clockwise and negative for counter-clockwise polarization. [78-80].

As was stated earlier, the ellipsometry technique is based on the *transformation* of the polarization state of light when it is reflected at or transmitted through an interface or film. When a light wave enters a discontinuity in the refractive index, as found at the interface between two different media (0 and 1), the parallel and perpendicular reflection coefficients (r_{01p} and r_{01s}) depend on the orientation of the electric field. This dependence is given by the Fresnel equations:

$$r_{01p} = \frac{N_1 \cos\phi_0 - N_0 \cos\phi_1}{N_1 \cos\phi_0 + N_0 \cos\phi_1} \text{ and} \qquad (4.1a)$$

$$r_{01s} = \frac{N_0 \cos\phi_0 - N_1 \cos\phi_1}{N_0 \cos\phi_0 + N_1 \cos\phi_1}, \qquad (4.1b)$$

where N_x is the refractive index in medium x, given by $N = n - ik$, and angles ϕ_0 and ϕ_1 are related according to Snell's law:

$$n_0 \sin\phi_0 = n_1 \sin\phi_1. \qquad (4.2)$$

The principle of ellipsometry is based on the measurement of the change in polarization when light reflects on a surface, due to the difference in the reflection for the p- and s-direction. The complex ration ρ between the p- and s-reflection coefficients is used to express this change of polarization

$$\rho = \frac{r_p}{r_s}. \qquad (4.3)$$

Both the phase and amplitude ratio from the p- and s-waves are of interest. Fortunately, the two reflection coefficients are *independent*. Therefore two independent parameters of the surface can be determined, for instance the real and imaginary part of the refractive index. Equation (4.3) can be rewritten as

$$\rho = \frac{r_p}{r_s} = \tan\Psi e^{i\Delta}, \qquad (4.4)$$

where Ψ and Δ are the two ellipsometric angles which characterize the polarization effects of the surface. Ψ is the angle whose tangent gives the ratio of the amplitude attenuation for the p and s polarisations, while Δ gives the difference between the phase shifts experienced by the p and s polarisations. They depend on the angle of incidence, the wavelength, the optical constants and the morphology of the film.

4.3 Polarization modulated ellipsometry (PME)

The different ellipsometric systems can be categorized in the way the state of polarization of a light wave is modified, namely through (1) reflection or refraction, (2) transmission and (3) scattering. Only the reflection ellipsometry will be considered here. The main reflection ellipsometric systems are the Rotating Analyzer Ellipsometer (RAE), the Rotating Polariser Ellipsometer (RPE) and the Polarization Modulated Ellipsometer (PME). The ellipsometric system considered in this thesis is the PME. The advantages of PME over RAE and RPE are a good signal-to-noise ratio at all wavelengths, unambiguous values of Ψ and Δ and a good background correction. The main disadvantage of PME is the lack of measuring speed; a full spectrum (1.5-5.0 eV) is measured in 3 minutes.
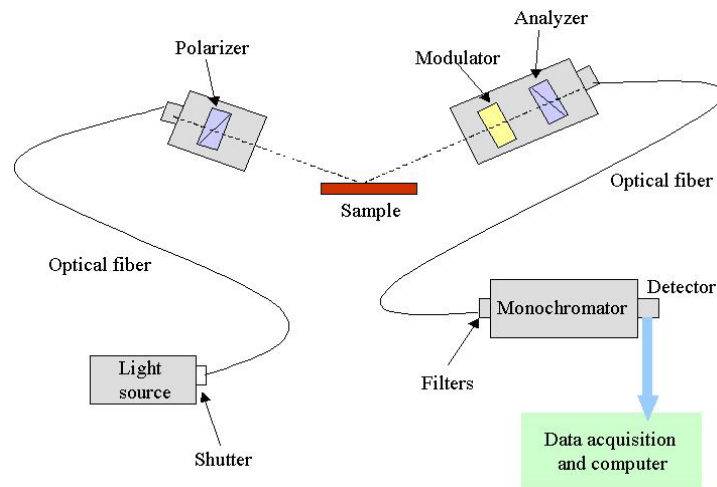
Figure 4.1 Measurement arrangement of PME (courtesy of Jobin Yvon)

4.3.1 Ellipsometric arrangement

The measurement arrangement of PME is shown in Figure 4.1. The experimental set-up is arranged in the *PSMA* order (Polariser, Sample, Modulator and Analyzer). Within PME, two configurations are used, namely the II and the III configuration. In the II configuration, P=45°, M=0° and A=45°, while in the III configuration P=90°, M=45° and A=45°. The measurements described in this thesis have been done in the II configuration.

The hart of the PME set-up is the Photoelastic Modulator (PEM). It is a rectangular shaped fused silica cemented with a piezo-electric quartz crystal (Figure 4.2). This piezoelectric crystal is activated by a 50 kHz sinusoidal signal, which induces a time varying birefringence through the silica bar, thus creating an optical anisotropy in the silica bar. The effect of the birefringence is to generate a periodic relative phase shift $\delta(t)$ between orthogonal components of the transmitted beam. This relative phase shift has the following general form:

$$\delta(t) = A \sin \omega t , \tag{4.5}$$

where ω is the resonant angular frequency, given by $2\pi f$ (f=50kHz) and A is the modulation amplitude.
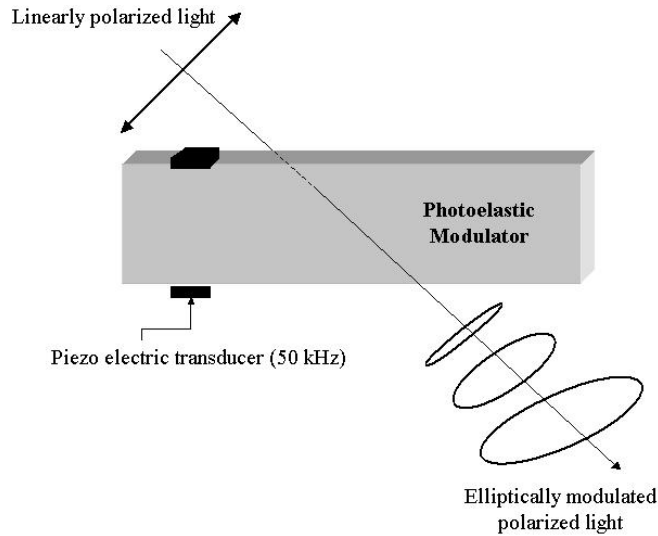
Figure 4.2 Schematic representation of the photoelastic modulator
(courtesy of Jobin Yvon)

4.3.2 Measurement and calculation

If equation (4.5) is considered, then the detected signal I generally looks like:

$$I = I_0(1 + I_\omega \cos \delta(t) + I_{2\omega} \sin \delta(t)), \tag{4.6}$$

where I_0 is the incident intensity and I_ω and $I_{2\omega}$ are the fundamental and second-harmonic components of the detected photocurrent, respectively. In configuration II, as used in the performed experiments, I_ω and $I_{2\omega}$ are given by

$$I_\omega = \sin 2\Psi \sin \Delta \text{ and} \tag{4.7}$$

$$I_{2\omega} = -\sin 2\Psi \cos \Delta, \text{ respectively.} \tag{4.8}$$

During the measurements, I_ω and $I_{2\omega}$ are measured as a function of photon energy.

To calculate the pseudo-dielectric function ε from the calculated values of Ψ and Δ equations (4.1a) and (4.1b) can be rewritten as

$$r_{01p} = \frac{\tan(\phi_0 - \phi_1)}{\tan(\phi_0 + \phi_1)} \text{ and} \tag{4.9}$$

$$r_{01s} = \frac{-\sin(\phi_0 - \phi_1)}{\sin(\phi_0 + \phi_1)}, \tag{4.10}$$

using Snell's law, giving in equation (4.2). The pseudo-dielectric function ε is than given by:

$$\varepsilon = \sin \phi^2 \left(1 + \left(\frac{1-\rho}{1+\rho}\right)^2 \tan \phi^2\right), \tag{4.11}$$

where ϕ is the angle of incidence of the light beam. If equations (4.4) and (4.11) are combined, the pseudo-dielectric constant as a function of the ellipsometric angles Ψ and Δ is given by

$$\varepsilon = \sin \phi^2 \left(1 + \left(\frac{1 - (\tan(\Psi)e^{i\Delta})}{1 + (\tan(\Psi)e^{i\Delta})}\right)^2 \tan \phi^2\right). \tag{4.12}$$

From equation (4.12), it can be deduced, that ε has two components, a real and an imaginary part, ε_r and ε_i, respectively. From ε_r and ε_i, the real and imaginary part of the refractive index can be deduced, using

$$\varepsilon_r = n^2 - k^2 \text{ and} \tag{4.13}$$

$$\varepsilon_i = 2nk. \tag{4.14}$$

During the measurements, I_ω and $I_{2\omega}$ are measured as a function of photon energy and the software used for the measurements directly calculates Ψ, Δ, ε_r, ε_i, n and k.

Table 4.1 System specifications of UVISEL ellipsometer
for spectroscopic measurement

Light source	75 W arc Xe lamp
Beam diameter	1 mm
Spectral range	230-840 nm
Spectral resolution	0.5 nm
Measurement time	3 min.
Reproducibility Ψ	0.01°
Reproducibility Δ	0.02°

These calculated values represent the value for the *total system*, thus substrate and layer. It is thus possible for the pseudo-dielectric constant to be negative.

4.3.3 Ellipsometry set-up

The ellipsometer used was a UVISEL spectroscopic phase modulated ellipsometer (Jobin Yvon). The specifications of this system are listed in Table 4.1. The main components of the system are the modulator and analyzer. The modulator contains the polarizer. The ellipsometer is attached to the ATLAS system, as shown in Figure 4.3, in such a way that the complete ellipsometer system can be moved up and down, in order to align the light beam and obtain the largest signal. The highest sensitivity of the system is obtained when working near the Brewster angle of materials. This angle ϕ_B for a material with a refractive index n is defined by

$$\tan\phi_B = n. \tag{4.15}$$

The measurements are performed at an incident beam angle of 72°. The system can operate in two modes, namely spectroscopic and kinetic.

4.3.3.1 Spectroscopic ellipsometry

In spectroscopic ellipsometry, the light beam, when leaving the analyzer, is directed into a monochromator, and the values for Ψ and Δ are measured as a function of photon energy. The main parameters to be adjusted are the spectral limits, the energy increment and the integration time. The settings used in this study are a photon energy ranging from 1.5 to 5.0 eV with an increment of 0.05
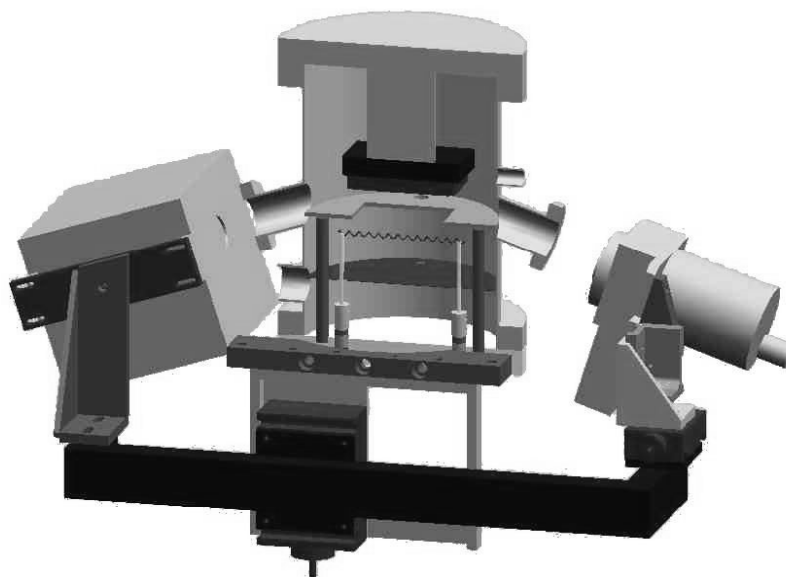
Figure 4.3 Ellipsometry set-up

eV and an integration time of 200 ms. Spectroscopic ellipsometry was used to characterize deposited layers. It is possible to determine the thickness and layer composition by fitting the measured data. This procedure will be described later.

4.3.3.2 Kinetic ellipsometry

During kinetic ellipsometry, the values of Ψ and Δ are measured for only *one* photon energy. The photon energy used during kinetic ellipsometry is usually 3.4 eV [81,82], because by using this energy, interface sensitivity can be achieved. An energy of 3.4 eV provides information about the nucleation and coalescence occurring at the substrate/film interface during the initial phase of the film deposition. The time interval used during the kinetic measurements is 1 s.

The representation of a kinetic ellipsometry experiment is given as a plot of the imaginary part of the measured dielectric constant of the system (i.e. substrate and film), ε_i, as a function of the real part, ε_r, with time as the implicit parameter.

4.4 Data interpretation

The interpretation of the ellipsometry data can be done in two ways: qualitative and quantitative. The qualitative interpretation of the data can be done by examining the measured imaginary part of the dielectric constant, ε_i, as function of photon energy. In such a spectrum, a number of qualitative aspects of the measured layer can be deduced. The low (<3 eV), middle (3-4.3 eV) and high (>4.3 eV) energy parts of the spectrum give insight in the thickness, optical density and roughness of the layer, respectively. Furthermore, the appearance of crystalline features at photon energies of 3.4 and 4.2 eV can give an indication of the crystallinity of the layer.

In order to get more quantitative information from the measured data, fitting of this data is required. The data generated during the spectroscopic ellipsometry measurement is fitted with the standard ellipsometry software supplied with the ellipsometer, i.e. ELLI43 by Jobin-Yvon. This program can calculate the spectral dependencies of the ellipsometric angles Ψ and Δ and the pseudo-dielectric function ε of a reflecting multi-layer system with surface roughness, which is in any ambient and on a substrate. The program supposes that the substrate, each of the layers, the roughness and the ambient can consist of three material components. In such a case, the effective dielectric function of the total system (i.e. substrate, layer, roughness, ambient) is calculated with an effective medium model, by using standard values for ε (delivered with ELLI43) for the different components of the layers. In this case, Bruggeman effective medium approximation (EMA) is used [83]. This model describes a composite of aggregated phases or random-mixture microstructure. The measured dielectric function is fitted using the following equation:

$$\sum_j f_j \left(\frac{\varepsilon_j - \varepsilon_{av}}{\varepsilon_j + 2\varepsilon_{av}} \right) = 0 , \tag{4.16}$$

with f_j being the volume fraction of the j-th medium, ε_j its dielectric constant and ε_{av} the dielectric constant of the mixture.

In order to fit the spectroscopic ellipsometry data, a layered structure was taken into consideration, as shown in Figure 4.4. The fitting program calculates the measure of discrepancy as defined by Pearson's chi-square statistics [84]:

$$X^2 = \sum_i \frac{(F_i - M_i)^2}{M_i} , \tag{4.17}$$

d_3	roughness	f_{c3}, f_{a3}, f_{v3}
d_2	bulk material	f_{c2}, f_{a2}, f_{v2}
d_1	incubation layer	f_{c1}, f_{a1}, f_{v1}
	Corning glass	

Figure 4.4 Model used to fit spectroscopic data. d_1, d_2, d_3 f_c, f_a and f_v are the thickness of the incubation, bulk and roughness layer and the crystalline, amorphous and void fractions, respectively. Thicknesses not to scale.

where F_i and M_i are the fit value and the measured value for the i-th data point, respectively. The fitting procedure is an iterative process, in which the thickness of the different layers and their composition is changed in such a way, that X^2 is minimized.

The interpretation of the kinetic ellipsometry data is much more difficult than in the spectroscopic case. The plot of ε_i as a function of ε_r can give information on the growth processes occurring at the substrate. It is for instance possible to look at the convergence of initial nucleation clusters. This phenomenon is reflected as a lobe-cusp feature in the $(\varepsilon_i, \varepsilon_r)$ curve [85].

4.5 Performed experiments

The experiments described here have all been performed using tantalum filaments.

In order to study the influence of pausing the deposition, for performing spectroscopic ellipsometry measurements on the film that is deposited, two amorphous silicon layers have been deposited (pressure p: 20 μbar, silane flow ΦSiH_4: 60 sccm, substrate temperature T_{sub}: 350°C, filament current I_{fil}: 12 A). In the first case, a layer was deposited continuously for 5 minutes, ending with a spectroscopic measurement. During the deposition of the second layer, four
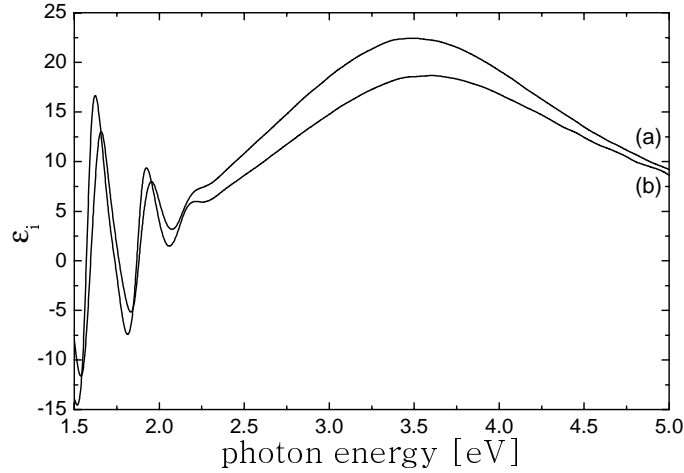
Figure 4.5 Spectroscopic ellipsometry data for a-Si:H films on Corning glass.
(a) 1x5 minutes; (b) 5x1 minute deposition.

deposition breaks were introduced after every minute of deposition. During
each break, a spectroscopic ellipsometry measurement was performed. The
results of the ellipsometry measurements for both deposited layers are shown in
Figure 4.5. From this figure, it follows that the layer deposited discontinuously
is thicker and has a lower optical density and larger surface roughness, as
compared to the continuously grown film. These phenomena are also observed
in the deposition of microcrystalline silicon. The lower optical density is
probably caused by the presence of multiple incubation layers, which are less
dense than bulk material. The cause of the larger growth rate and surface
roughness are not yet understood.

Spectroscopic ellipsometry studies have been performed after
depositions with changing silane flow (ΦSiH_4). The other parameters (pressure
p, hydrogen flow ΦH_2, substrate temperature T_{sub} and filament current I_{fil}) were
kept constant. The used values for these parameters are listed in Table 4.2.

Table 4.2 Deposition parameters used during ellipsometric studies

Parameter	Value
Pressure, p	100 µbar
Hydrogen flow, ΦH_2	150 sccm
Substrate temperature, T_{sub}	400°C
Filament current, I_{fil}	11.5 A
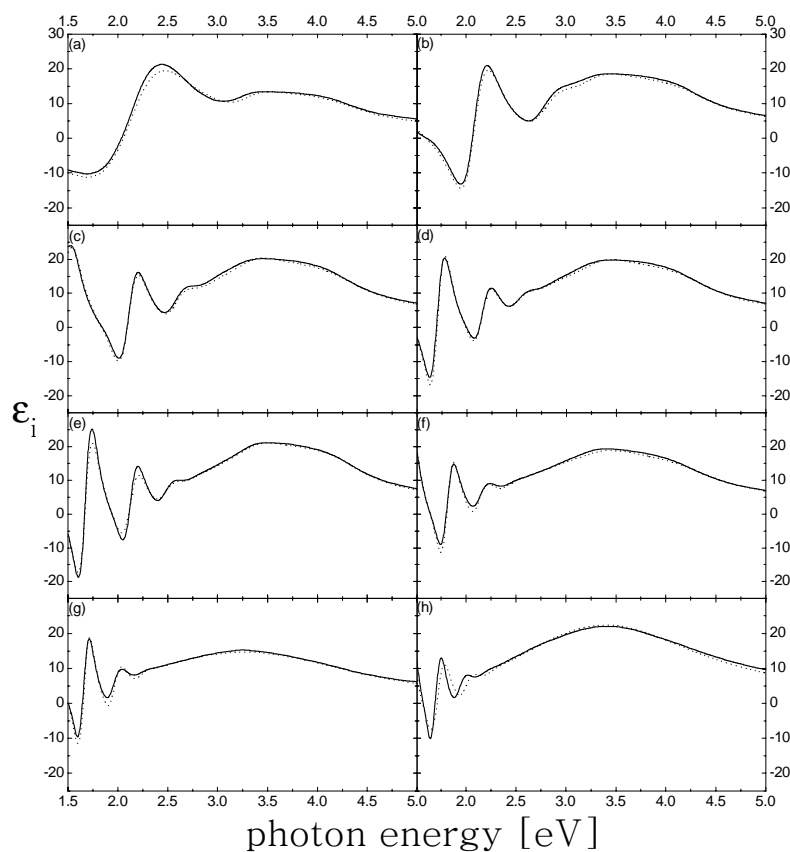
Figure 4.6 Spectroscopic ellipsometry data (solid line) and fitting results (dotted line) for films deposited on Corning glass for 10 minutes. Deposition parameters: pressure p: 100 µbar, substrate temperature T_{sub}: 400°C, filament current I_{fil}: 11.5 A, hydrogen flow ΦH_2: 150 sccm, silane flow ΦSiH_4: (a) 2 sccm, (b) 4 sccm, (c) 6 sccm, (d) 8 sccm, (e) 10 sccm, (f) 12.5 sccm, (g) 15 sccm, (h) 20 sccm.

The silane flow was changed from 2 to 20 sccm. Two deposition series have been performed in which the deposition time and deposited film thickness were kept constant at 10 minutes and about 30 nm, respectively.

The results of the spectroscopic ellipsometry measurements of the 10 minutes deposition series are shown in Figure 4.6. Qualitatively, from this

Table 4.2 Fitting results obtained with model as shown in Figure 4.4 for the 10 min. deposition series. Relative errors in d and f are 1% and 5%, respectively.

ΦSiH_4 [sccm]	d_1 [nm]	f_{c1} [%]	f_{a1} [%]	f_{v1} [%]	d_2 [nm]	f_{c2} [%]	f_{a2} [%]	f_{v2} [%]	d_3 [nm]	f_{c3} [%]	f_{a3} [%]	f_{v3} [%]
2	18.1	1	36	63	37.1	62	13	25	5.7	36	0	64
4	0.4	46	51	3	111.2	53	33	14	5.5	28	25	47
6	0.1	0	100	0	182.2	56	35	9	4.7	26	25	49
8	n/a	n/a	n/a	n/a	242.9	49	42	8	4.5	43	4	53
10	2.1	0	100	0	248.0	55	37	8	4.1	51	0	49
12.5	0.3	0	98	2	308.5	26	65	9	4.9	29	21	50
15	n/a	n/a	n/a	n/a	342.7	11	78	11	9.1	0	53	47
20	43.8	0	71	29	271.3	0	100	0	3.7	0	50	50

figure, it can be deduced that the thickness increases and the crystalline fraction decreases with increasing silane flow. Also plotted in Figure 4.6 are the fitting results obtained by using the model as shown in Figure 4.4. The fitting results are given in Table 4.2.
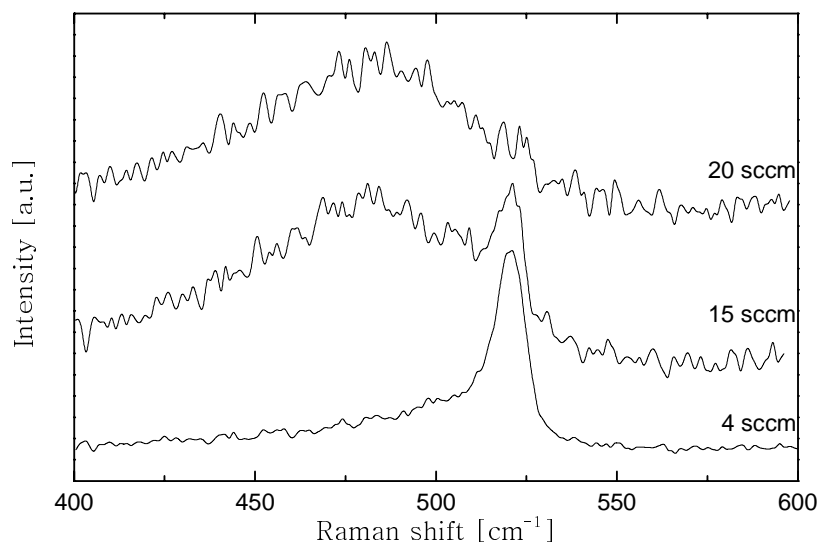

Figure 4.7 Raman spectra for different silane flows.

Table 4.3 Crystalline volume fraction f_c as function of silane flow ΦSiH_4, calculated from Raman spectroscopy. For comparison, the crystalline fraction of the bulk layer f_{c2}, as calculated from the ellipsometry data, is listed.

ΦSiH_4 (sccm)	f_c (Raman)	f_{c2} (ellipsometry)
2	0.91±0.09	0.62±0.02
4	0.65±0.01	0.53±0.03
6	0.63±0.05	0.56±0.03
8	0.64±0.05	0.49±0.02
10	0.60±0.06	0.55±0.03
12.5	0.55±0.06	0.26±0.01
15	0.18±0.08	0.11±0.01
20	0.05±0.07	0±0

The crystallinity of the deposited layer has also been verified using Raman spectroscopy. Three typical Raman spectra are shown in Figure 4.7. The values of f_c, as calculated with equation 2.6, are shown in Table 4.3. It is clear from this table that the values for the crystalline volume fraction are larger when calculated from Raman spectroscopy, as compared to the ellipsometry results but that the general trend is the same: the crystalline volume fraction decreases with increasing silane flow. The larger values of f_c, as calculated from the Raman spectroscopy results, can be explained by the fact that Raman spectroscopy is mainly surface sensitive, with a measuring thickness of up to 100 nm. It is generally known, that the crystalline fraction at the surface of a film is larger than in the bulk, due to crystal growth.

The deposition rate as a function of the silane flow is shown in Figure 4.8. From this figure, it can be concluded that there is some kind of transition from poly– or microcrystalline to amorphous growth. This transition occurs at a silane flow of about 9 sccm.

Table 4.4 Deposition time for ~30 nm layer thickness t_{30nm} for different silane flows ΦSiH_4.

ΦSiH_4 [sccm]	t_{30nm} [s]
2	600
4	206
6	131
8	113
10	81
12.5	64
15	57
20	46
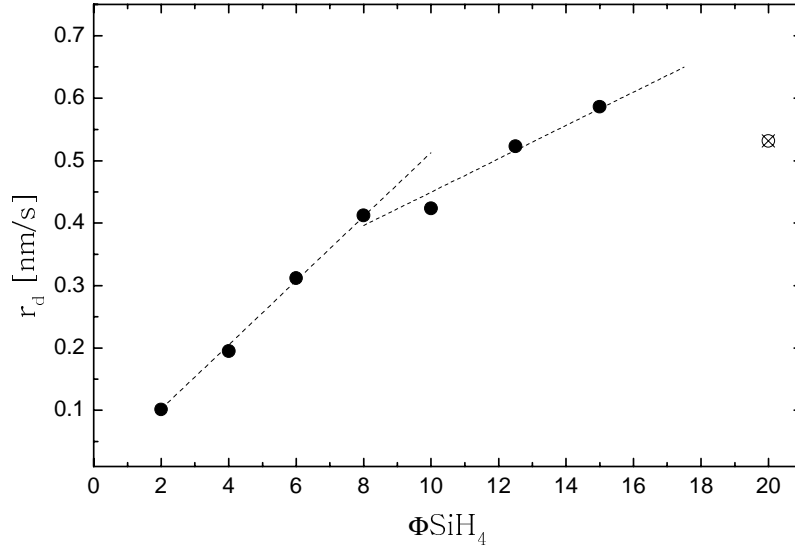
Figure 4.4 Deposition rate r_d as function of silane flow ΦSiH_4.
The lines are guides to the eye.

From a simple fit of the thickness of the layers, using only a *single amorphous* layer, the time to deposit a layer of about 30 nm (t_{30nm}) was calculated. These times are given in Table 4.4.

Table 4.5 Fitting results obtained with model as shown in Figure 4.4 for ~30 nm
deposition series. Relative errors in d and f are 1% and 5%, respectively.

ΦSiH_4 [sccm]	d_1 [nm]	f_{c1} [%]	f_{a1} [%]	f_{v1} [%]	d_2 [nm]	f_{c2} [%]	f_{a2} [%]	f_{v2} [%]	d_3 [nm]	f_{c3} [%]	f_{a3} [%]	f_{v3} [%]
2	18.1	1	36	63	37.1	62	13	25	5.7	36	0	64
4	1.4	0	96	4	30.3	69	14	17	5.1	1	51	48
6	0.1	0	97	3	32.9	38	54	8	3.1	0	53	47
8	7.2	0	84	16	30.3	51	43	6	3.6	38	12	50
10	9.5	0	60	40	23.9	21	79	0	4.0	22	29	49
12.5	n/a	n/a	n/a	n/a	27.3	5	94	1	3.5	0	57	43
15	1.6	0	92	8	25.7	0	100	0	2.4	0	51	49
20	0.9	0	65	35	27.3	0	100	0	2.4	0	57	43

The results of the spectroscopic ellipsometry measurements after the ~30 nm depositions are shown in Figure 4.9, together with the fitting results obtained by using the model as shown in Figure 4.4. The fitting results of these measurements are shown in Table 4.5.
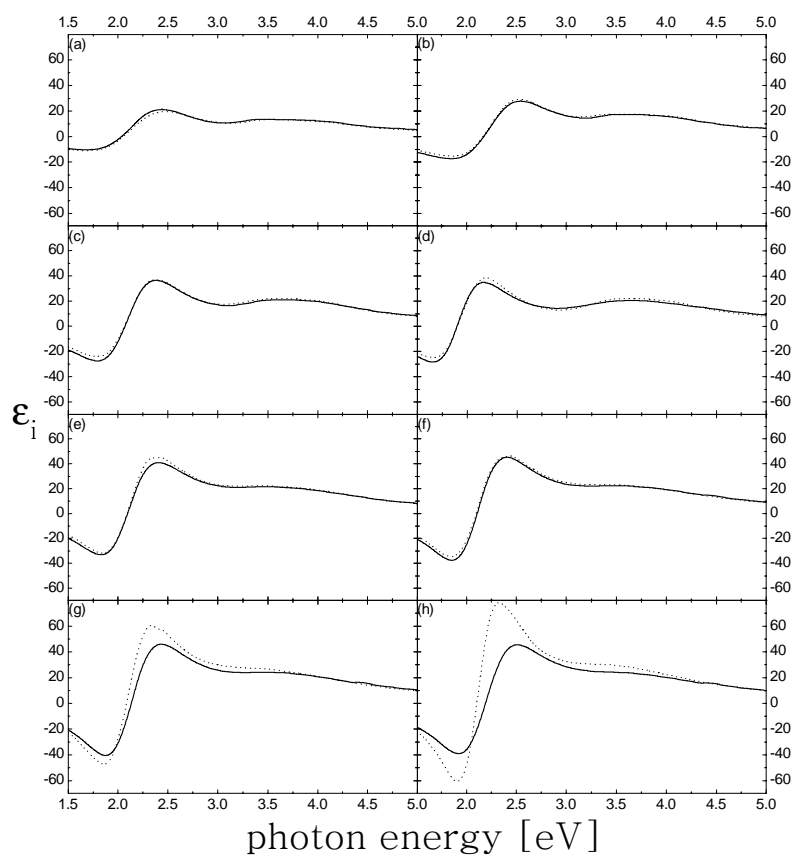
Figure 4.9 Spectroscopic ellipsometry data (solid line) and fitting results (dotted line) for films deposited on Corning glass. Deposition times are given in Table 4.3. Deposition parameters: pressure p: 100 µbar, substrate temperature T_{sub}: 400°C, filament current I_{fil}: 11.5 A, hydrogen flow ΦH_2: 150 sccm, silane flow ΦSiH_4: (a) 2 sccm, (b) 4 sccm, (c) 6 sccm, (d) 8 sccm, (e) 10 sccm, (f) 12.5 sccm, (g) 15 sccm, (h) 20 sccm.

Also investigated was the influence of the use of a seed layer on the deposited layer. For this purpose, the material deposited with 2 sccm silane and 150 sccm hydrogen was used as seed layer. After 10 minutes of deposition, the silane flow was increased to either 15 or 20 sccm and the layer was grown to a thickness that was about the same as the films deposited without the seed layer. The spectroscopic ellipsometry results are shown in Figure 4.10, together with the fitting results and the ellipsometry results of the layers deposited without seed layer. The thicknesses and composition of the layer, following from the ellipsometry fits are listed in Table 4.6.
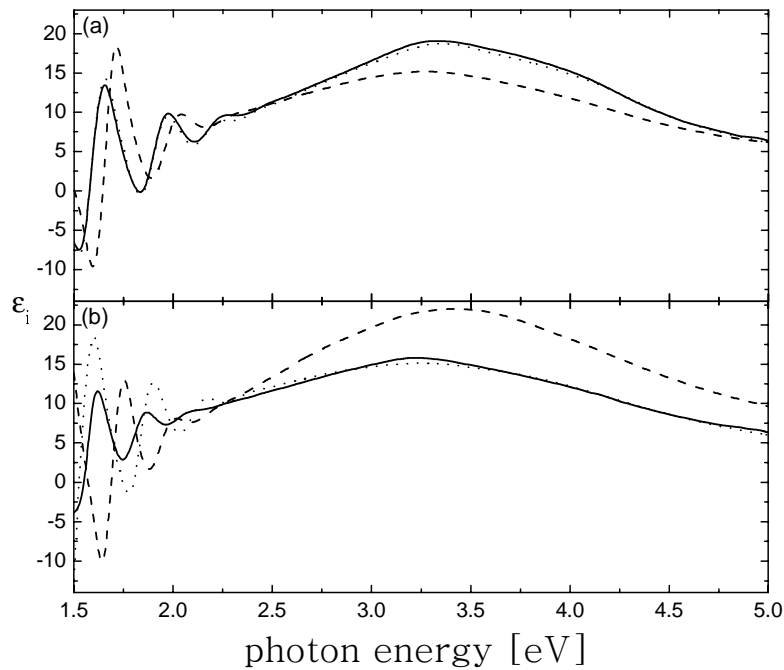

Figure 4.10 Spectroscopic ellipsometry data (solid line) and fitting results (dotted line) for films deposited using seed layer on Corning glass. Deposition parameters: pressure p: 100 µbar, substrate temperature T_{sub}: 400°C, filament current I_{fil}: 11.5 A, hydrogen flow ΦH_2: 150 sccm, silane flow ΦSiH_4: (a) 2 sccm for 600 s, followed by 15 sccm for 520 s and (b) 2 sccm for 600 s, followed by 20 sccm for 540 s. The dashed lines are the results of the continuously grown layers with ΦSiH_4: (a) 15 sccm and (b) 20 sccm.

Table 4.6 Fitting results obtained with model as shown in Figure 4.4 for the layers deposited using a seed layer. For comparison, also the fitting results of the continuous grown layers are given.

ΦSiH_4 [sccm]	d_1 [nm]	f_{c1} [%]	f_{a1} [%]	f_{v1} [%]	d_2 [nm]	f_{c2} [%]	f_{a2} [%]	f_{v2} [%]	d_3 [nm]	f_{c3} [%]	f_{a3} [%]	f_{v3} [%]
2->15	42.6	44	22	34	331.3	**59**	41	0	8.0	19	37	45
15	n/a	n/a	n/a	n/a	342.7	**11**	78	11	9.1	0	53	47
2->20	40.6	40	44	16	320.6	**30**	70	0	11.5	0	58	42
20	43.8	0	71	29	271.3	**0**	100	0	3.7	0	50	50

From Figure 4.10, it follows that there is a large influence of the seed layer on the final values of ε_i of the layers. This also follows from the fitting results, using the model shown in Figure 4.4. The seed layer was put into the model as incubation layer. The fitting results are given in Table 4.5.

These layers have also been characterized by Raman spectroscopy. The results of these measurements are shown in Figure 4.11. The general trend of these results confirms the spectroscopic ellipsometry data, although the values do differ, again due to the surface sensitivity of Raman spectroscopy.
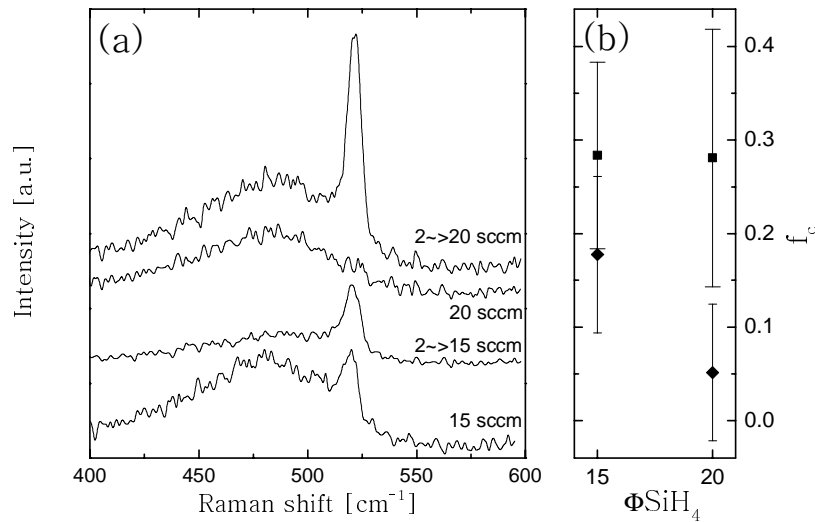

Figure 4.11 Results of Raman spectroscopy for layers deposited with and without the use of a seed layer. (a) Raman spectra of the different layers, (b) crystalline volume fraction f_c as function of silane flow, calculated from the Raman spectra, using equation 2.6. Diamonds: without seed layer; squares: with seed layer.
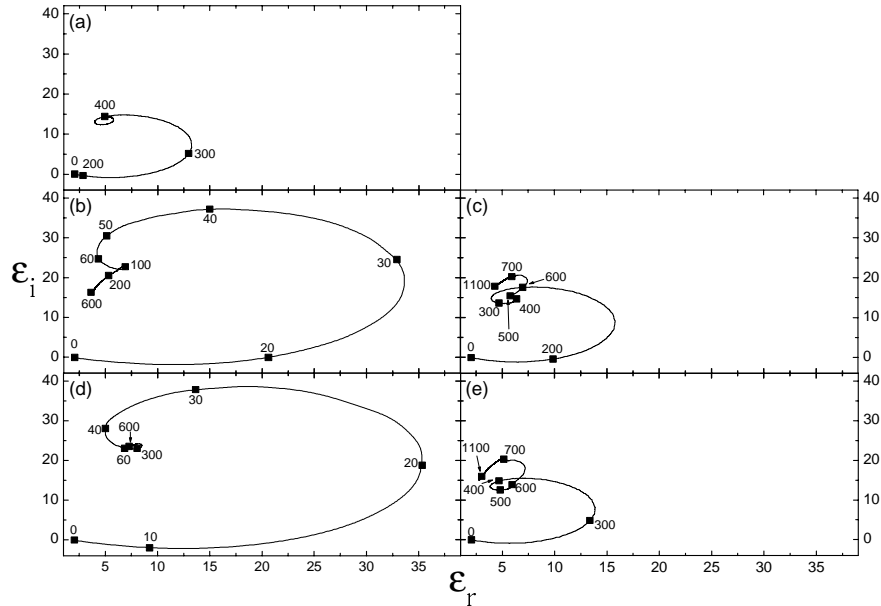
Figure 4.12 Kinetic ellipsometry trajectories for films deposited on Corning glass. Deposition parameters: pressure p 100 μbar, substrate temperature T_{sub} 400°C, filament current I_{fil} 11.5 A, hydrogen flow ΦH_2 150 sccm, silane flow ΦSiH_4: (a) 2 sccm for 600 s, (b) 15 sccm for 600 s, (c) 2 sccm for 600 s, followed by 15 sccm for 520 s, (d) 20 sccm for 600 s and (e) 2 sccm for 600 s, followed by 20 sccm for 540 s. The points are labeled with the deposition time in s.

The effect of the seed layer on the growth of the layer has also been studied by kinetic ellipsometry using a photon energy of 3.4 eV. Figure 4.12 shows the results of these measurements, represented as $(\varepsilon_r, \varepsilon_i)$ trajectories. When the trajectories of the films deposited using no incubation layer (Figure 4.12 (a,b,d)) are compared, two significant differences between the highly crystalline layer deposited at $\Phi SiH_4 = 2$ sccm and the more amorphous-like layers deposited at $\Phi SiH_4 = 15$ and 20 sccm are observed. First of all, the deposition using high silane flows starts immediately at $t = 0$ s, while in the first 200 s of the deposition using 2 sccm silane, no observable growth occurs. The other difference between the high and low flow samples is the much larger amplitude of both ε_i and ε_r in the high silane flow case, when compared to the

layer deposited at low silane flow. This higher amplitude is characteristic for amorphous growth.

Figure 4.12(b) (ΦSiH_4 = 15 sccm) also shows a very distinct lobe feature at t = 100 s. This lobe is not present in trajectory of the film deposited at ΦSiH_4 = 20 sccm. Collins and Cavese [86] attributed this lobe to the convergence of initial growth structures and the presence of this lobe is considered to be necessary for high-quality a-Si:H. According to Collins et al. [86], the absence of the lobe in Figure 4.12(d) can have two causes: (1) the initial growth structures form but do not converge, leaving voids at the interface or (2) no individual growth structures are formed, i.e. a uniform film will grow. Looking at the large value for f_{v1} for the sample deposited at ΦSiH_4 = 20 sccm (Table 4.2), it can be assumed that the initial growth structures do not converge, resulting in a large void content at the substrate-film interface.

Looking at the samples deposited using the layer deposited with ΦSiH_4 = 2sccm as seed layer (Figure 4.12 (c,e)), it is clear that the trajectories of the first 600 s of (seed layer) deposition are similar to the trajectory of the sample deposited at ΦSiH_4 = 2 sccm (Figure 4.12(a)). Furthermore, after the change from low to high silane flow, which occurs at t = 600 s, there still is not much difference between both samples, although the final values for ε_i and ε_r are somewhat larger for the 15 sccm SiH$_4$ case. The final part of the trajectories (t > 700 s) has been attributed to the evolution of surface roughness [87].

4.6 Conclusions

In this chapter, the deposition of *polycrystalline* silicon layers by Hot-Wire CVD using *tantalum* as filament material has been investigated using spectroscopic and kinetic ellipsometry. Ellipsometry is a very useful tool for the characterization of films. Two factors make ellipsometry particularly attractive: (1) its essentially non-perturbing character, hence its suitability for in-situ measurements, and (2) its remarkable sensitivity to minute interfacial effects. The spectroscopic ellipsometry data was fitted using a three-layer model (Figure 4.4), while the kinetic ellipsometry data was interpreted qualitatively.

Spectroscopic ellipsometry studies on a series of films deposited at increasing hydrogen dilution, i.e. decreasing silane flow with constant hydrogen flow, revealed that the crystallinity of the layers increased, as was found both by spectroscopic ellipsometry and Raman spectroscopy of completed films. The growth rate decreases with increasing hydrogen dilution.

The deposition of profiled layers, using a highly crystalline, 40 nm thick, seed layer deposited at a silane/hydrogen ratio of 2/150, was studied by both spectroscopic and kinetic ellipsometry. These studies showed that by using a seed layer, the crystalline fraction in the bulk of layers deposited at amorphous deposition conditions (low hydrogen dilution) could at least be increased up to 30%. Furthermore, the crystalline fraction of a layer, originally exhibiting a crystalline fraction of 10%, could with this method be increased to 60%.

Chapter 5

Materials

5.1 Introduction

For thin film silicon solar cells, polycrystalline layers with so-called 'device-quality' properties are needed to obtain cells with reasonably good properties. These 'device-quality' properties according to Schropp and Zeman [8], are listed in Table 5.1.

Table 5.1 Criteria for 'device quality' polycrystalline silicon films [8].

	Property	Requirement
Minimum set	Crystalline fraction (Raman)	90 %
	Orientation of the grains (XRD)	mostly (220)
	Band gap, indirect	1.0-1.1 eV
	100mW/cm^2 photoconductivity	$> 10^{-5}$ S/cm
	Dark conductivity	$< 10^{-7}$ S/cm
	Photosensitivity	> 100
	Activation energy	~0.55 eV
Additional characteristics	Hall mobility activation energy	< 0.02 eV
	Minority carrier diffusion length	> 500nm
	Mobility-lifetime product at 600 nm	$\geq 1 \times 10^{-7}$ cm^2/V
	Defect density (ESR; $g = 2.005$)[*]	$\leq 1 \times 10^{17}$ cm^{-3}

[*] For *intrinsic* material

Table 5.2 Typical deposition conditions (filament temperature T_{fil}, substrate temperature T_{sub}, silane flow ΦSiH_4, hydrogen flow ΦH_2 and pressure p) used for Hot-Wire deposition of amorphous and polycrystalline intrinsic silicon films [7].

Parameter [units]	a-Si:H	poly-Si:H
T_{fil} [°C]	1850	1800
T_{sub} [°C]	430	530
ΦSiH_4 [sccm]	90	10
ΦH_2 [sccm]	0	150
p [mbar]	0.02	0.1

In this chapter, the material properties important for solar cells (e.g. photo- and dark conductivity) of the layers that have been deposited by Hot-Wire CVD will be given, grouped by the filament material used, i.e. tungsten (W), tantalum (Ta) and rhenium (Re).

5.2 Silicon deposited using W as filament

5.2.1 Historical overview

The research at Utrecht University on thin film polycrystalline silicon deposited by Hot-Wire CVD using W as filament material started in 1996. A thorough study of the influence of the different deposition parameters was performed. Rath et al. [88,89] reported on the deposition of both intrinsic amorphous (a-Si:H) [21] and polycrystalline (poly-Si:H) films. Typical deposition conditions are listed in Table 5.2.

Schropp et al. [7] characterized the materials using a wide range of techniques, e.g. Raman spectroscopy, X-ray diffraction, atomic force microscopy (AFM) and electron spin resonance (ESR). A list of typical material properties is given in Table 5.3. These properties fall within the range as specified in Table 5.1.

The major drawback of the 'device-quality' polycrystalline silicon material described above is the presence of an amorphous incubation layer. It is not possible to either measure or optimise the electronic properties of this incubation layer. The presence of this layer was confirmed by Raman spectroscopy and cross sectional transmission electron microscopy (XTEM) [90]. In the transmission electron micrograph (shown in Figure 5.1), the

Table 5.3 Typical material properties of Hot-Wire deposited amorphous (a-Si:H) and polycrystalline (poly-Si:H) intrinsic silicon films [88]

Property [units]	a-Si:H	poly-Si:H
Crystalline fraction [%]	0	95
Average grain size [nm]	-	70
Deposition rate [nm/s]	2	0.55
Hydrogen content [%]	9	0.47
Photoconductivity [S/cm]	3×10^{-5}	2×10^{-5}
Dark conductivity [S/cm]	2×10^{-10}	1.5×10^{-7}
Bandgap [eV]	1.7 (direct)	1.1 (indirect)
Activation energy for dark conductivity [eV]	0.85	0.54

amorphous incubation phase is clearly visible. Also observable in this figure is the presence of large crystals, growing conically in the (220) direction from the amorphous incubation layer. These crystals grow perpendicular to the substrate, resulting in the absence of grain boundaries in the plane parallel to the substrate.

In order to avoid the incubation layer and deposit a fully crystalline silicon layer, higher hydrogen dilution ($\Phi SiH_4/\Phi H_2 = 0.7/150$) has been applied, as was found in Chapter 4. This higher dilution resulted in *fully* crystalline material, which was verified by Raman spectroscopy and XTEM. The cross sectional transmission electron micrograph is shown in Figure 5.2. This figure clearly shows the absence of any amorphous phase and XRD showed the presence of *randomly* oriented grains. The deposition rate of this material is lower than the 'device-quality' material. The large amount of (atomic) hydrogen present in the reactor is likely to be the cause of the growth of the fully crystalline layer, since it etches weak Si-Si bonds, resulting in crystalline instead of amorphous material.
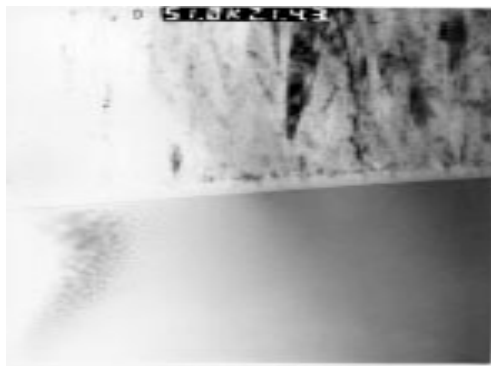

Figure 5.1 XTEM image of polycrystalline silicon on glass with incubation phase
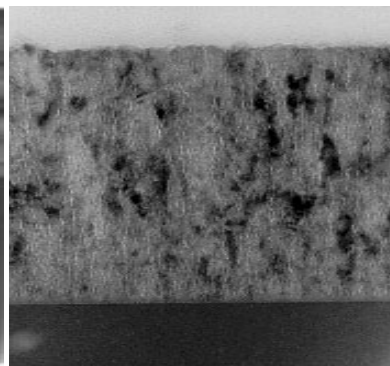
Figure 5.2 XTEM image of fully crystalline silicon on glass

The properties of the material deposited at high hydrogen dilution are poor, showing high dangling bond density (3 x 10^{18} cm^{-3}) and incorporation of oxygen due to a porous structure. This material is not suited for application in a solar cell.

From hereon, the fully crystalline material deposited using high hydrogen dilution will be called Poly1 and the device quality material with the amorphous incubation phase Poly2.

Besides the structural difference between Poly1 and Poly2, visible in XTEM, another important difference is seen in the FTIR spectra of the two materials (see Figure 5.3). It is clear, that Poly1 has a distinct peak at 2100 cm^{-1}, while the peak in Poly2 is located around 2000 cm^{-1}. There is still a lot of controversy about the interpretation of the infrared data. The vibration at 2100 cm^{-1} is attributed to the Si-H bonds at the crystal surface. The splitting of this peak, as visible in Figure 5.3, is still under discussion. Various configurations have been proposed: (1) Si-H bonds on different grain surfaces [15,91], (2) different bonding configurations (mono- or dihydride bonds on different surfaces in silicon crystallites) [92] and (3) optically anisotropic Si-H monolayers [93]. Rath et al. [31] performed hydrogen diffusion and effusion experiments to clarify the observation of the stretching vibration mode at 2000 cm^{-1} in Poly2, instead of at 2100 cm^{-1} commonly reported in the literature for microcrystalline silicon films [32]. The results of these effusion experiments proved that the 2000 cm^{-1} mode in Poly2 is due to Si-H bonds in the crystalline region.
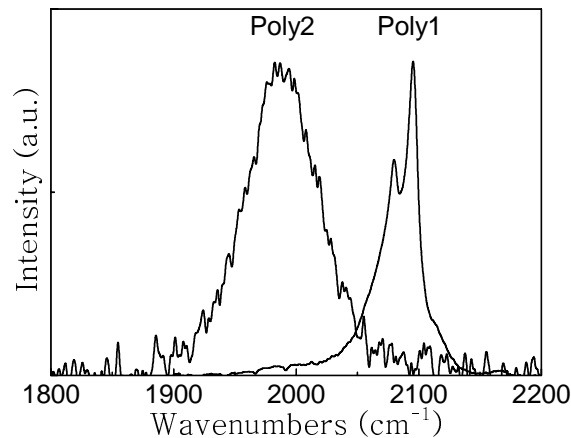
Figure 5.3 FTIR spectra of Poly1 and Poly2 layers
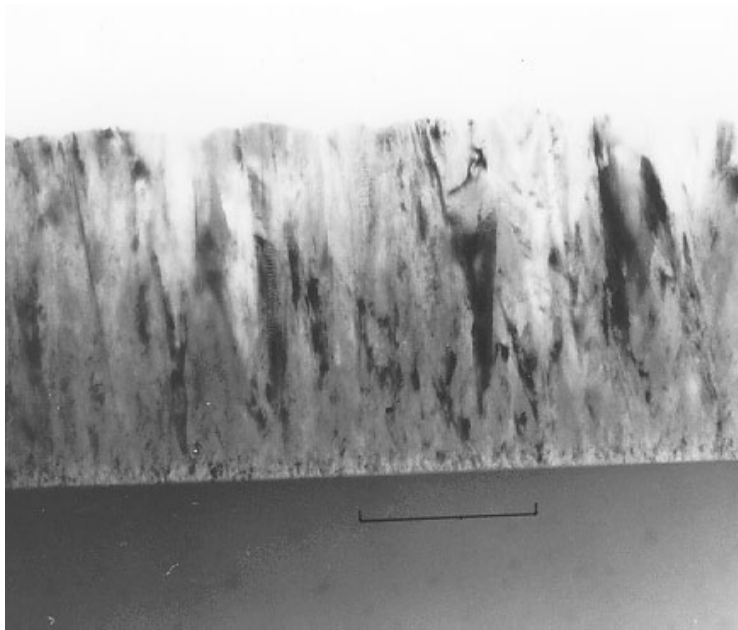
Figure 5.4 XTEM image of profiled layer on glass. Scale bar: 500 nm

In order to combine the advantages of both Poly1 (fully crystalline layer) and Poly2 ('device-quality'), a profiled layer has been used [94]. During the deposition of this profiled layer, the deposition parameters are changed from Poly1 to Poly2 conditions. In practice, the hydrogen dilution is decreased from 99% to 90% by instantly increasing the silane flow. The resulting layer consists of a thin seed layer (~20 nm Poly1) onto which the Poly2 layer is deposited. The profiled layer indeed has device quality properties without the presence of an amorphous phase, as is shown in the cross sectional electron transmission electrograph given in Figure 5.4.

5.2.2 Optical absorption of poly-Si:H

Reflection-transmission measurements (RT) and photothermal deflection spectroscopy (PDS) have been used to measure the optical absorption coefficient α of different materials (i.e. a-Si:H, Poly1, Poly2 and profiled Poly1/Poly2). The results of these measurements are shown in Figure 5.5.
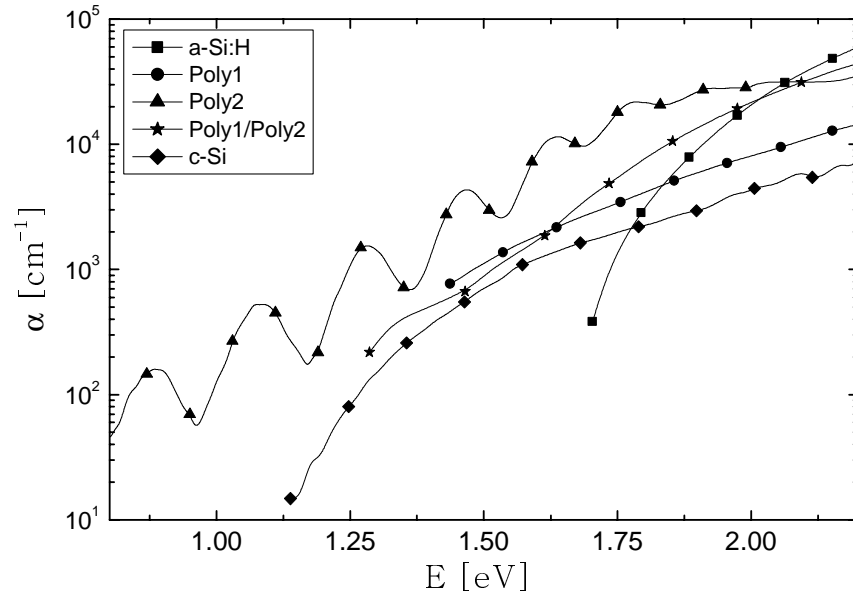
Figure 5.5 Optical absorption coefficient α of different types of silicon as function of
photon energy E, measured with PDS and RT, except for c-Si [95]

From this figure, it is obvious that a-Si:H has a larger bandgap,
compared to poly-Si:H or c-Si. Furthermore, the absorption coefficient of Poly1
is lower than that of Poly2 and more in the order of c-Si. The profiled layer,
consisting of 1.5 μm Poly2 deposited on top of ~50 nm Poly1, exhibits values
of α in between the value for Poly1 and Poly2. The absorption coefficient of
Poly2 exhibits large interference fringes, probably due to (1) internal reflection
in a part of the layer or (2) surface roughness.

The most striking result shown in this figure is the greatly enhanced
value of the absorption coefficient of Poly2 compared to c-Si. The origin of this
enhanced absorption has been the subject of speculation. The following aspects
have been proposed as circumstances enhancing the absorption: (1) surface
scattering, (2) internal scattering, (3) effective medium in a multiphase system
and (4) strain in the bulk [96]. These aspects are discussed below [97].

In order to study the influence of the surface scattering on the optical
absorption, angular resolved light scattering (ARLS) measurements were
performed, both on as-deposited and polished layers. Polishing of the layers was
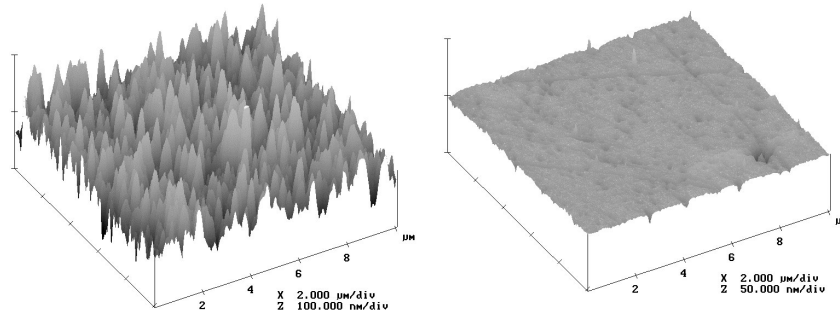
Figure 5.6 3D-AFM-representation of as-deposited (left) and polished (right) Poly2.
X- and Y-axis: 2 μm/div, Z-axis: as-deposited: 100 nm/div; polished: 50 nm/div

performed using 100 nm diamond particles on a mechanical polishing machine. The surface roughness of the layers was determined by atomic force microscopy. The AFM-results are shown in Figure 5.6. From this figure, it follows that the polishing treatment decreases the rms surface roughness from 50 nm in the as-deposited case to about 5 nm for the polished layer. During the polishing treatment, the thickness of the Poly2 layer decreased from 1.3 μm to 1 μm.
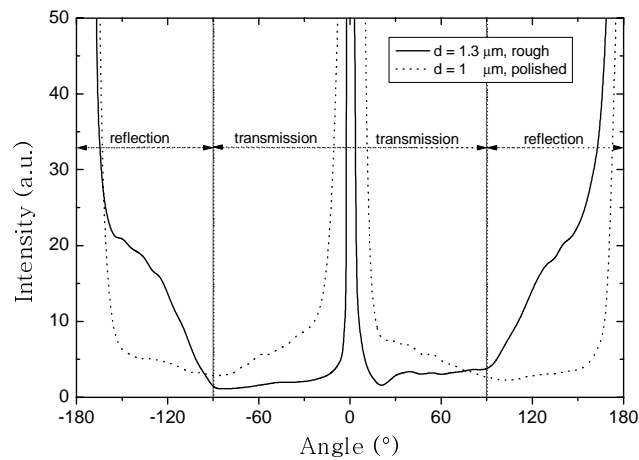

Figure 5.7 Angular resolved light scattering for as-deposited and polished Poly2.
The measurements have been normalized to the signal at an angle of 0°.

The results of the angular resolved light scattering measurements for the as-deposited and polished Poly2 layers are shown in Figure 5.7. From this figure, it follows that the as-deposited film shows a significant diffused reflection, which correlates to the surface texture of Poly2. Polishing of the film reduces the diffused reflection as a result of a decreasing surface roughness. However, the transmittance is mostly specular. Polishing of the film does not significantly affect the angular dependence of the transmittance. This is a result of the high absorption in the bulk of the film due to which the diffused part is mostly absorbed in the film. Figure 5.8 shows the optical absorption coefficient for the as-deposited and polished film. From this figure, it follows that the interference fringes, present in the as-deposited sample, disappear after polishing. This suggests that the interference fringes are indeed due to the surface texture of the as-deposited film. Combining Figures 5.7 and 5.8, it can be suggested that polishing the as-deposited Poly2 does not change the optical absorption coefficient significantly. This indicates that the influence of surface scattering on the enhanced absorption is only minor. However, from the angular resolved light scattering measurements, it follows that the reflection has a negative effect; namely the loss due to diffused reflection.
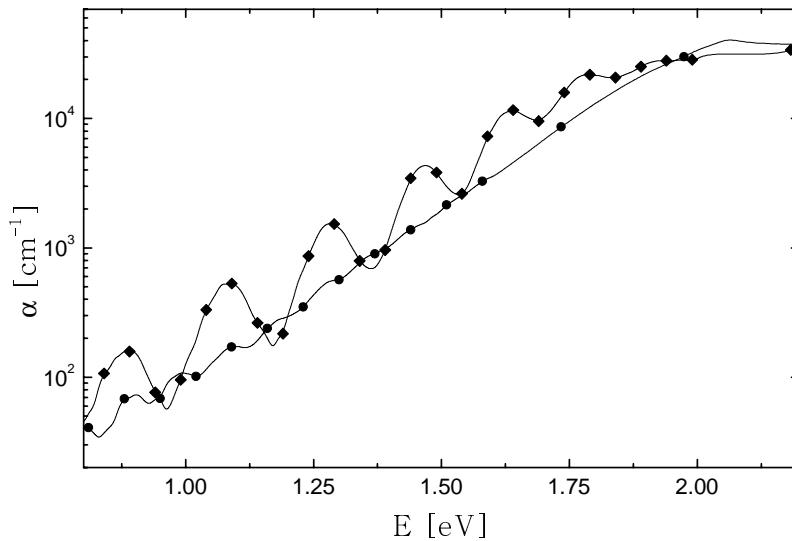
Figure 5.8 Optical absorption coefficient α as function of photon energy E for as-deposited (diamonds) and polished (circles) Poly2 films on glass
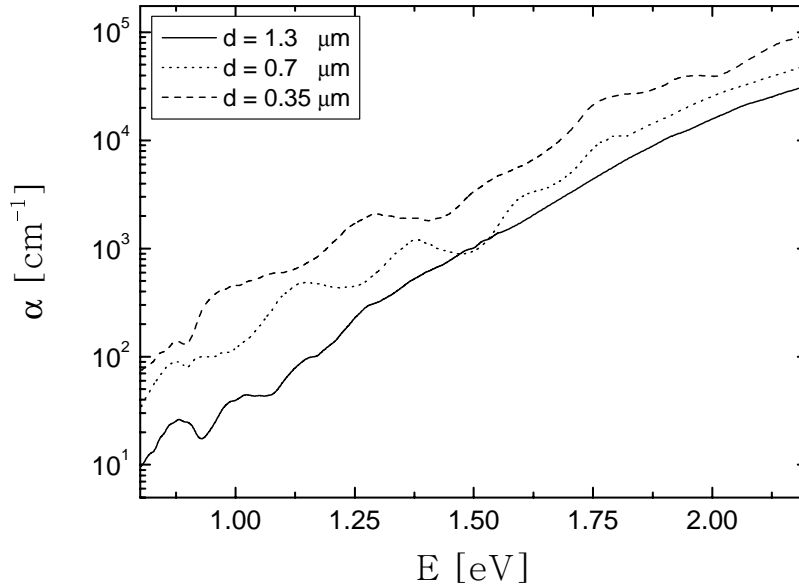
Figure 5.9 Thickness dependence of the absorption coefficient α versus
photon energy E in profiled Poly1/Poly2 on glass.

As was already concluded from Figure 5.2, there is an amorphous incubation layer present at the substrate/film interface. This incubation phase could result in a higher absorption coefficient. However, from Figure 5.5, it is clear that the difference between Poly2 and the profiled layer (Poly1/Poly2) is only minor, in spite of the fact that no amorphous incubation layer is present in the profiled layer. The enhanced absorption coefficient can thus not be attributed to the presence of an amorphous phase.

The thickness dependence of the absorption coefficient in a profiled Poly1/Poly2 layer has also been studied to determine the influence of the incubation layer on the optical absorption coefficient. This dependence is shown in Figure 5.9. This figure shows a monotonic increase of the optical absorption coefficient with decreasing thickness over the entire energy range.

The exponential tail region in poly-Si at 1.1 eV has been correlated to strain in the film. Vaněček et al. [29] reported a value of less than 50 meV for this slope in μc-Si:H. This energy is interpreted as a disorder-induced broadening of the indirect absorption edge of c-Si [98]. The thickness

dependence of the slope of the optical absorption coefficient at 1.1 eV, calculated from Figure 5.9, is shown in Figure 5.10. An increase of the slope from 151 meV to 192 meV is found. These high values compared to the values for μc-Si:H [29] are due to larger strain in the layer. The occurrence of strain in the film is confirmed by Raman spectroscopy. The Raman spectrum of the profiled Poly1/Poly2 layer is shown in Figure 5.11. In the spectrum, a small contribution of amorphous silicon (480 cm^{-1}) is visible, which was already expected form the XTEM (see Figure 5.4). The Raman spectrum measured from the front side shows a peak at 520 cm^{-1}, characteristic for crystalline silicon. The spectrum measured through the glass (backside) shows a slightly shifted crystalline peak and a shoulder at 490-500 cm^{-1}. The shift in the crystalline peak position and the shoulder at 490-500 cm^{-1} can be attributed either to a distribution of small grains or to grain boundary defects (strained Si-Si bonds). The distribution of small grains or the grain boundary defects can be the cause of the high value of the tail slope (Figure 5.10). It is inferred that the
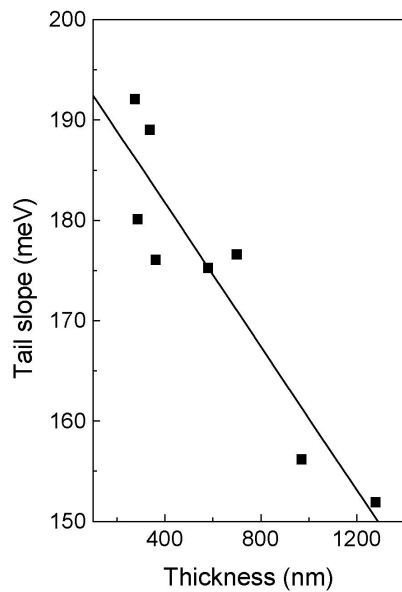

Figure 5.10 Thickness dependence of the slope of the optical absorption coefficient at 1.1 eV. The line is a guide to the eye.
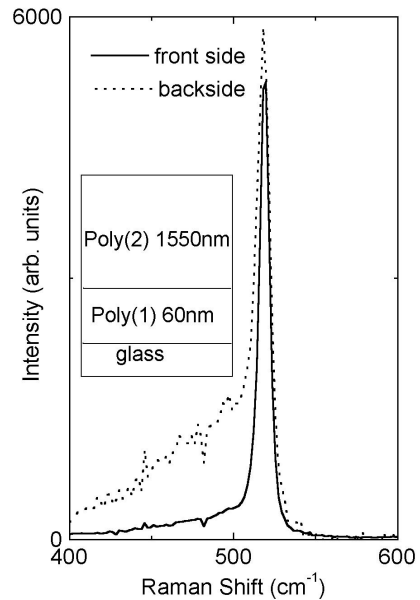
Figure 5.11 Raman spectrum of profiled Poly1/Poly2 on glass from back- and front side.

Table 5.3 Penetration depths $d_{1/e}$ for different wavelengths λ in silicon

λ [nm]	α [cm^{-1}]	$d_{1/e}$ [nm]
320	1.5 x 10^6	7
500	2 x 10^4	500
690	4 x 10^3	2500

interface between the Poly1 seed layer and the Poly2 layer has a high density of strained bonds, whose influence gradually decrease with increasing Poly2 layer thickness.

5.2.3 Time-resolved microwave conductivity studies

Another method to get more insight into the influence of the amorphous incubation phase or the use of a seed layer is the use of time-resolved microwave conductivity [99,100], as described in section 2.2.7. During these experiments, three different wavelengths have been used to excite layers of Poly1 (50 nm), Poly2 (~1500 nm) and profiled Poly1/Poly2 (~1600 nm). The wavelengths used were 690 nm (1.8 eV), 500 nm (2.5 eV) and 320 nm (3.9 eV). For each of these wavelengths, the penetration into the silicon layer is different and depends on the absorption coefficient of the material at a given wavelength. The 1/e penetration depths ($d_{1/e}$) for the wavelengths used are given in Table 5.3. The different penetration depths give the opportunity to get information on the properties of charge carriers at different depths within the sample.

The samples were irradiated both from the front and backside. The measured microwave conductivity transients are shown in Figure 5.12. The majority of the transients could be fitted using equation (2.15), using only one lifetime τ. A somewhat better fit could in some cases be achieved by including a small contribution from a second, longer-lived component ($\tau_2 \approx 40$ ns). The differences between different batches of samples prepared were less than 20% [100].

The time-resolved microwave conductivity measurements have also been performed by the LPICM-group of the Ecole Polytechnique de Palaiseau [101], on the same samples. These experiments have been performed at an irradiation wavelength of 512 nm. These results were indeed fitted using two lifetimes (τ_1 and τ_2).
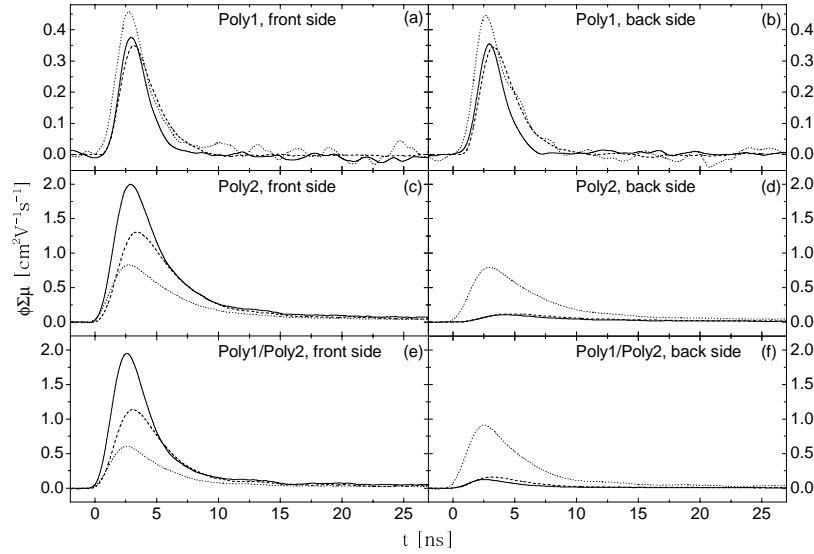
Figure 5.12 TRMC transients for poly-Si:H thin films using wavelengths of 320 nm (full line), 500 nm (dashed line) and 690 nm (dotted line). (a): Poly1, front side, (b): Poly1, backside, (c): Poly2, front side, (d): Poly2, backside, (e): Poly1/Poly2, front side and (f): Poly1/Poly2, backside. Note the different y-axis for the Poly1 layer.

Table 5.4 Charge carrier mobility $\Sigma\mu$ and lifetimes τ determined for poly-Si:H samples studied during front and backside illumination at 320, 500 and 690 nm. Light intensity is 20 μJ/cm^2, except for measurements on Poly1 and for the samples irradiated from backside at 320 nm, where the intensity is 80 μJ/cm^2.

	320 nm		500 nm		690 nm	
	$\Sigma\mu$ [cm^2/Vs]	τ [ns]	$\Sigma\mu$ [cm^2/Vs]	τ [ns]	$\Sigma\mu$ [cm^2/Vs]	τ [ns]
Front						
Poly1	≥ 1.1[a]	≤ 1.0[a]	≥ 1.1[a]	≤ 1.0[a]	≥ 1.4[a]	≤ 1.0[a]
Poly2	3.8	2.3	2.8	2.5	1.8	2.3
Poly1/Poly2	4.0	1.8	2.8	2.0	2.5	1.8
Back						
Poly1	≥ 1.0 [a]	≤ 1.0[a]	≥ 1.3 [a]	≤ 1.0[a]	≥ 1.5[a]	≤ 1.0[a]
Poly2	0.14	5.0	0.19	5.5	1.7	2.5
Poly1/Poly2	0.23	2.3	0.38	2.0	2.3	1.7

[a] Lower limit due to the 1 ns time resolution of the detection system

Table 5.5 Charge carrier mobilities ($\Sigma\mu$) and lifetimes (τ_1 and τ_2) determined for different polycrystalline samples upon front side illumination at 512 nm, measured at Ecole Polytechnique de Palaiseau (LPICM).

	512 nm [101]		
	$\Sigma\mu$ [cm^2/Vs]	τ_1 [ns]	τ_2 [ns]
Poly1	0.25	1.9	-
Poly2	6.9	7.5	80
Poly1/Poly2	5.5	2.3	120

5.2.3.1 Discussion of Poly1 TRMC results

As is evident from Figure 5.12(a) and 5.12(b), the conductivity transients of the Poly1 sample are independent of the used wavelength and of the illumination mode (front or backside). From this, it can be concluded that the morphology of Poly1 is uniform throughout the layer, which was already expected from the XTEM-image in Figure 5.3. In all cases, the conductivity transients follow the shape of the laser pulse convoluted with the overall response time of the detection system of ~1 ns. For this reason, only an upper limit for the mobility and a lower limit for the lifetime can be deduced (see Table 5.4). The values for $\Sigma\mu$ and τ, as measured at LPICM do not differ significantly.

The short lifetime in Poly1 is attributed to small, randomly oriented crystals and the resulting presence of a high density of charge carrier trapping sites at grain boundaries [99,100].

5.2.3.2 Discussion of Poly2 TRMC results

From Figure 5.12(c) and 5.12(d), it is clear that there is a large difference between the transients for front and back side illumination. Furthermore, the magnitude of the transients is seen to be strongly dependent on the wavelength used. These results prove that there is a spatial dependence of both the mobility and lifetime of the generated charge carriers.

The lifetime of the charge carriers has been determined from convolution fits to the transients. The values obtained for $\Sigma\mu$ and τ, assuming mono-exponential decay, are listed in Table 5.4.

The results for front side illumination show a decrease in $\Sigma\mu$ from 3.8 to 1.8 cm^2/Vs on increasing the depth of penetration, i.e. increasing the wavelength of the light. These values are comparable to values reported by others [40,41]. The gradual decrease in mobility can be explained by the fact

that the grain size within Poly2 increases in the growth direction. The largest grains are therefore closest to the surface and support higher charge carrier mobility.

The conductivity transient found upon backside illumination with $\lambda =$ 320 nm is more than one order of magnitude smaller than that found for front side illumination at the same wavelength. This is in agreement with the finding that the incubation layer in Poly2 is amorphous. This amorphous incubation layer can also explain the fact that there is not much difference between the transients at 320 nm and 500 nm, since the absorption coefficient of amorphous silicon at 500 nm is much larger compared to polycrystalline silicon. This larger absorption results in a smaller penetration depth. Thus, both the transients for 320 nm and 500 nm result only from charge carriers formed within the amorphous incubation layer. This follows also from the values of $\Sigma\mu$ and τ (Table 5.4), which do not differ a lot. The longer lifetime of ~5 ns in the amorphous layer, found upon illumination from the backside at 320 and 500 nm, can be explained by the lower mobility, lower defect density and a lower trapping rate in that layer. Light with a wavelength of 690 nm is almost uniformly absorbed throughout the sample. The transients for front and back side illumination at this wavelength are therefore of similar magnitude and the values for $\Sigma\mu$ and τ are also very similar.

5.2.3.3 Discussion of Poly1/Poly2 TRMC results

The transients of the profiled Poly1/Poly2 sample upon front side illumination with the different wavelengths (Figure 5.12(e) and 5.12(f)) and the derived values for $\Sigma\mu$ and τ can be seen to be very similar to those of Poly2. This indicates that the morphology of the top of the profiled layer and the top of the Poly2 are alike and thus do not depend on the initial incubation layer.

When the transients for backside illumination of Poly1/Poly2 and Poly2 are compared, it follows that these are also similar. This could be expected for the 690 nm measurements because the whole layer is probed in that case, but it is not expected for the other wavelengths, because that light is absorbed mostly in the incubation layer, which is either Poly1 (in the profiled Poly1/Poly2) or an amorphous layer (in Poly2). The transients measured at 320 and 500 nm look in fact more like those found for the amorphous incubation layer of Poly2 than for Poly1, as shown in Figure 5.12(b). The mobility values determined for Poly1/Poly2 are significantly lower than the lower limit found for Poly1, although they are almost double the value for the amorphous incubation layer in Poly2. A possible explanation is that the initial layer formed during or after changing the deposition conditions from Poly1 to Poly2 introduces a large

number of grain boundary defects leading to strained Si-Si bonds. Evidence of the existence of such a layer was given by Raman spectroscopy (section 5.2.2). Rapid diffusion of mobile carriers from the Poly1 layer into this strained region can therefore explain the lower mobilities.

5.2.4 Low temperature Poly-Si

The layers described so far (Poly1, Poly2, Poly1/Poly2) have all been deposited at a substrate temperature of 530°C. In order to study the influence of the substrate temperature on the material deposited, the substrate temperature T_{sub} has been lowered from 530°C to 480°C and 430°C, while maintaining the same deposition parameters as used during Poly2 deposition. The material properties of these layers are listed in Table 5.6. From this table, it follows that the films deposited at lower substrate temperature show higher activation energy for dark conductivity. Especially the layer deposited at a substrate temperature of 430°C shows amorphous-like activation energy of 0.766 eV. Indeed, X-ray diffraction (XRD) as well as Raman spectroscopy revealed a very small crystalline fraction. For this material, also the photosensitivity (1.3×10^4) points towards a large fraction of amorphous material. XRD measurements on the material deposited at a substrate temperature of 480°C showed exclusively (220) crystal orientation, while the XTEM measurement (Figure 5.13), shows columnar packed crystals in the (220) orientation with very little amorphous tissue (<5%). The XTEM image is taken of a profiled film, without an amorphous incubation layer. The selective area diffraction pattern (SADP) confirms the high crystallinity and grains.

Table 5.6 Material properties (activation energy for dark conductivity (E_a), dark- and photo-conductivity (σ_d, σ_{ph}), photosensitivity (σ_{ph}/σ_d)) and crystal orientation (XRD) as function of substrate temperature (T_{sub}). For comparison, the properties of 'device-quality' polycrystalline silicon (DQ-poly-Si) are also listed.

T_{sub} [°C]	430°C	480°C	530°C	DQ-poly-Si
E_a [eV]	0.766	0.582	0.55	0.53-0.57
σ_d [S/cm]	1.6×10^{-8}	2.9×10^{-6}	1.5×10^{-7}	$< 1.5 \times 10^{-7}$
σ_{ph} [S/cm]	2.1×10^{-4}	1.5×10^{-4}	2.0×10^{-5}	$> 1.5 \times 10^{-5}$
σ_{ph}/σ_d	1.3×10^4	5.0×10^1	1.3×10^2	$>10^2$
XRD	-	(220)	(220)	mostly (220)
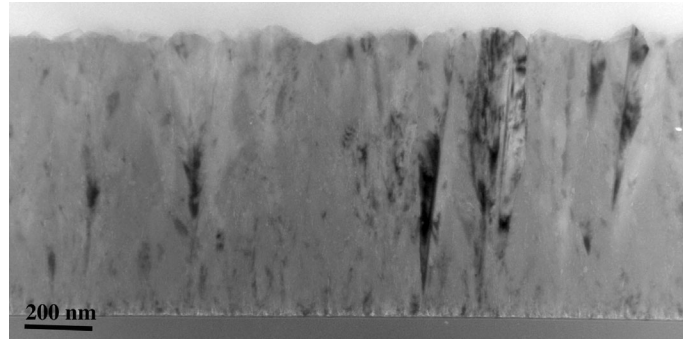
Figure 5.13 Cross-sectional transmission electron micrograph
of material deposited at a substrate temperature of 480°C

5.3 Silicon deposited using Ta as filament

The main disadvantage of W as filament material is the short lifetime, due to the large increase of silicon on the filament surface, as was already shown in Chapter 3. To extend the filament lifetime, tantalum (Ta) has also been used as filament. The lifetime indeed increased by several orders of magnitude.

To study the deposition of polycrystalline silicon using tantalum as filament material, a hydrogen dilution series was performed. The deposition conditions are listed in Table 5.7. It should be noted that, compared to the W case, the filament temperature was rather high. The sample deposited at the highest hydrogen dilution ($\Phi SiH_4/H_2 = 0.7/150$) was used to produce Poly1-like material, whereas the aim of the other depositions was to produce Poly2. The properties of the layers are shown in Table 5.8. As is clear

Table 5.7 Deposition parameters (filament temperature T_{fil}, substrate temperature T_{sub}, silane flow ΦSiH_4, hydrogen flow ΦH_2 and pressure p) used for Hot-Wire deposition of polycrystalline silicon films using Ta filaments

Parameter [unit]	Value
T_{fil} [°C]	1930
T_{sub} [°C]	515
ΦSiH_4 [sccm]	0.7-10
ΦH_2 [sccm]	150-250
p [mbar]	0.1

Table 5.8 Material properties (thickness (d), growth rate (r_d) band gap (E_g), dark- and photo-conductivity (σ_d, σ_{ph}), photosensitivity (σ_{ph}/σ_d) and activation energy for dark conductivity (E_a)) for different silane-to-hydrogen ratios ($\Phi SiH_4/\Phi H_2$). For comparison, the properties of 'device-quality' polycrystalline silicon (DQ-poly-Si) are also listed.

$\Phi SiH_4/\Phi H_2$	0.7/150	10/250	10/200	10/150	DQ-poly-Si
d [nm]	450	1670	1630	1580	
r_d [nm/s]	0.08	0.58	0.57	0.55	
E_g [eV]	1.10	1.27	1.27	1.17	1.0-1.1
σ_d [S/cm]	-	3.1×10^{-6}	3.6×10^{-6}	1.0×10^{-6}	$< 1.5 \times 10^{-7}$
σ_{ph} [S/cm]	-	2.2×10^{-5}	9.4×10^{-6}	9.8×10^{-6}	$> 1.5 \times 10^{-5}$
σ_{ph}/σ_d	-	7	2.6	9.6	$>10^2$
E_a [eV]	0.569	0.618	0.627	0.587	0.53-0.57

from this table, the layers deposited within this hydrogen dilution series do not qualify for the term "device quality". For all samples, the photosensitivity is too low, mostly due to a too high value for the dark conductivity. If the values of the activation energy for dark conductivity and the band gap are compared, it can be concluded that the deposited materials are of intrinsic nature.
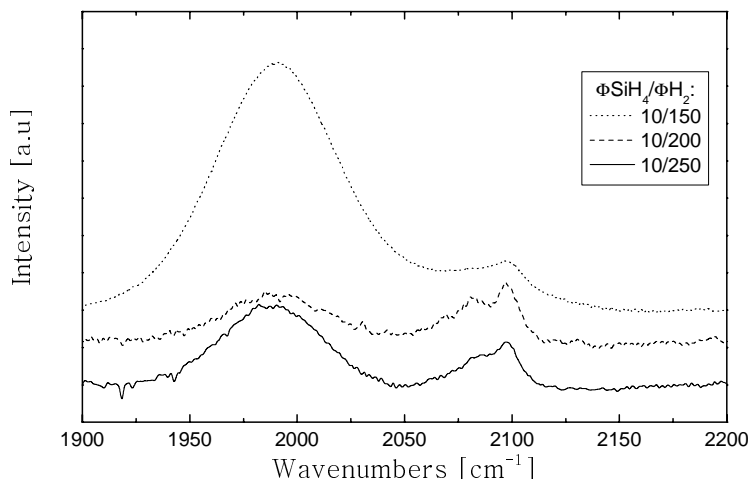

Figure 5.14 FTIR spectra of silicon films, deposited by Hot-Wire CVD using tantalum filaments with different silane-to hydrogen ratios $\Phi SiH_4/\Phi H_2$.

The deposited layers have also been characterized using Fourier-transform infrared spectroscopy (FTIR). The FTIR spectra are shown in Figure 5.14. It is clear that all the layers show peaks at both the 2000cm^{-1} and the 2100cm^{-1}, in contrast to Poly1 and Poly2, deposited using W filaments (see Figure 5.3).

5.4 Silicon deposited using Re as filament

Another possible filament material with increased lifetime could be rhenium, since the diffusion coefficient of silicon in rhenium is higher than in tungsten of tantalum. However, the lifetime of the rhenium filaments used was limited to several hours. This could be caused by the fact that large amounts of silicon diffuse into the filament, possibly resulting in a phase with a low melting point. No evidence to either support or invalidate this hypothesis is available.

Using rhenium as filament, a filament temperature series has been made using a silane-to-hydrogen ratio of 1:15, at a substrate temperature of 530°C and a pressure of 0.1 mbar. The resulting material properties are listed in Table 5.9. From this table, it follows that the films deposited using rhenium as filament material, show high activation energy for dark conductivity, when compared to the values for 'device-quality' polycrystalline silicon given in Table 5.1. This indicates the presence of a significant amount of amorphous material in the layer. The most relevant device property is the fact that XRD characterizations of these samples *all* showed exclusively (220) orientation. [102], with only minor (111) contribution for the sample deposited at the highest filament temperature of 1975°C.

Table 5.9. Properties of silicon layers deposited using rhenium as filament material for different filament temperatures (deposition rate (r_d), activation energy for dark conductivity (E_a), photo- and dark-conductivity (σ_d and σ_{ph}), photosensitivity (σ_{ph}/σ_d) and the peaks present in the XRD-spectrum).

T_{fil} [°C]	r_d [nm/s]	E_a [eV]	σ_d [S/cm]	σ_{ph} [S/cm]	σ_{ph}/σ_d	XRD
1725	0.78	0.639	8.9×10^{-7}	1.2×10^{-5}	14	(220)
1775	0.94	0.644	2.4×10^{-6}	1.5×10^{-5}	6	(220)
1800	0.77	0.659	2.0×10^{-6}	1.1×10^{-5}	5	(220)
1880	0.96	0.589	1.0×10^{-6}	3.8×10^{-6}	4	(220)
1975	1.1	0.589	1.4×10^{-6}	3.0×10^{-6}	2	(220) (111)

Looking at the values of the photosensitivity in Table 5.9, it can be expected that materials more interesting for use in solar cells (i.e. higher values of σ_{ph}/σ_d) should be deposited at even lower filament temperatures.

5.5 Conclusions

To conclude, the material properties of several layers deposited by Hot-Wire CVD using tungsten, tantalum and rhenium as filament material, have been studied.

The most extensively studied layers were deposited using tungsten as filament material at a filament temperature of 1800°C. "Device-quality" material, consisting of a thick Poly2 layer deposited on top of a thin Poly1 seed layer and deposited at a substrate temperature of 530°C, showed an enhanced optical absorption coefficient, compared to crystalline silicon. This enhancement was related to strained bonds at the Poly1/Poly2 interface. These layers have also been characterized using Time Resolved Microwave Conductivity (TRMC), giving the spatially resolved photoconductive properties of the layers, in the plane parallel to the substrate. Decreasing the substrate temperature resulted in an increase in activation energy for the dark conductivity. The layer deposited at a substrate temperature of 430°C showed amorphous-like values for the activation energy and the photosensitivity. XRD measurements on the material deposited at a substrate temperature of 480°C showed exclusively (220) crystal orientation, while the XTEM measurement (Figure 5.13), showed columnar packed crystals in the (220) orientation with very little amorphous tissue (<5%).

Using tantalum as filament material at a filament temperature of 1930°C, a hydrogen dilution series was carried out. The layers deposited do not qualify for the term "device quality". For all samples, the photosensitivity is too low, mostly due to a too high value for the dark conductivity. From the experience with tungsten and rhenium as filament material, the filament temperature is thought to be too high. This would mean that the filament temperature should be decreased in order to get better quality films.

Using rhenium as filament material, a filament temperature series was performed. The deposited layers showed high dark conductivity, probably due to the presence of amorphous tissue and a large amount of grain boundary defects. The orientation of the crystals present in the layers was, except for the layer deposited at the highest filament temperature of 1975°C, *exclusively* (220).

Chapter 6

Solar cells

6.1 Introduction

In contrast to wafer-based solar cells, which consists mostly of a p-n-structure, thin film silicon solar cells deposited at relatively low temperatures ($<600°C$) consist of three layers: an intrinsic layer, a p-doped layer and an n-doped layer. The use of the intrinsic layer is necessary because of the high defect density present in the doped layers. These defects are dopant induced. The p-n-junction in a wafer-based device results in the generation of an electric field. The charge carriers are generated in a field free region and *diffuse* towards the field, where they are separated and collected. In thin film solar cells, the charge carriers are created in the photoactive undoped i-layer and are transported through drift towards the contacts (p- and n-layer). Two structures are common in the thin film solar cell field, i.e. the superstrate or p-i-n- and the substrate or n-i-p-structure. In the superstrate structure, the p-i-n cell is deposited on glass coated with a transparent conductive oxide (TCO), like SnO_2:F, ZnO:Al or In_2O_3:Sn ("ITO") and light enters the cell through the glass, whereas in the substrate structure, the n-i-p cell is deposited on a (non-transparent) substrate, such as stainless steel, and light enters the cell from the top. A schematical representation of both structures is shown in Figure 6.1. The cells described in this thesis are deposited in the n-i-p configuration. The main reason to use this
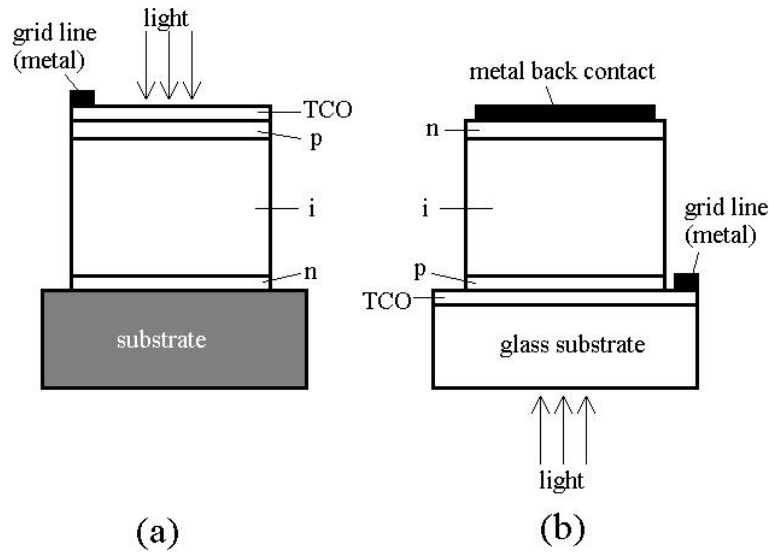
Figure 6.1 Schematic representation of (a) an n-i-p solar cell and (b) a p-i-n solar cell

configuration is the use of higher substrate temperatures in Hot-Wire CVD, as compared to PECVD, which is likely to result in the diffusion of dopant atoms from the doped layers to the i-layer. Since the diffusion of boron atoms proceeds much faster than the diffusion of phosphorous atoms [103], the n-i-p cell structure is favored over the p-i-n structure, because the i-layer is deposited on the n-layer, containing phosphorous. Furthermore, at the substrate temperatures used, the stability of the TCO is an issue.

The solar cells described in this chapter were deposited in the PASTA system (see section 2.1.1) on plain stainless steel substrates. This substrate also acts as the back electrode of the cell. It should be mentioned that no additional back reflector (e.g. textured ZnO/Ag) has been used. On this substrate an n-μc-Si:H layer was deposited by PECVD with a thickness of about 50 nm. After this, the i-layer is deposited by Hot-Wire CVD. The thickness of this layer is ~1.5 μm. On top of this layer, a p-μc-Si:H layer is deposited by PECVD, with a thickness of about 20 nm. After the deposition of the p-layer, at a substrate temperature of about 200°C, the top contact is deposited. For this purpose, an indium-doped tin oxide (ITO) layer with a thickness of ~80 nm is deposited by means of reactive thermal evaporation. Since the sheet resistance of the ITO layers is rather high (~100 $\Omega/\square$), a gold grid is deposited on top of the ITO, in order to reduce the effect of external series resistance on the fill factor.

Table 6.1 Deposition parameters and material properties (substrate temperature (T_{sub}), filament temperature (T_{fil}), silane flow (ΦSiH_4), hydrogen flow (ΦH_2), pressure (p), activation energy of dark conductivity (E_a), dark- and photoconductivity (σ_d, σ_{ph}) and photosensitivity (σ_{ph}/σ_d)) of layers used as intrinsic layer in n-i-p solar cells.

Filament material	Ta	W	W
T_{sub} [°C]	515	530	480
T_{fil} [°C]	1930	1800	1800
ΦSiH_4 [sccm]	10	10	10
ΦH_2 [sccm]	150	150	150
p [mbar]	0.1	0.1	0.1
E_a [eV]	0.587	0.55	0.582
σ_d [S/cm]	1.0×10^{-6}	1.5×10^{-7}	2.9×10^{-6}
σ_{ph} [S/cm]	9.8×10^{-6}	2.0×10^{-5}	1.5×10^{-4}
σ_{ph}/σ_d	9.6×10^{0}	1.3×10^{2}	5.0×10^{1}

6.2 Used i-layers

Considering the deposited layer described in Chapter 5, three different materials have been used as the intrinsic layer in solar cells. The deposition parameters and material properties of these materials are listed in Table 6.1. It should be mentioned that a highly crystalline seed layer, deposited at high hydrogen dilution, has been used as incubation layer to avoid the occurrence of the amorphous incubation phase observed in these layers.

6.3 Preliminary solar cell results

The *J-V* characteristic of the solar cell with the i-layer deposited using tantalum (Ta) as filament material is shown in Figure 6.2. In order to avoid current from outside the cell area, a mask is used. The cells all had an area of 0.16 mm^2 and, reckoning with the gold grid, an effective area of 0.13 mm^2. Also in this figure, the solar cell parameters (open circuit voltage V_{oc}, short circuit current density J_{sc}, fill factor *FF*, efficiency η and series and parallel resistance (R_s, R_p)) are listed. From the shape of the *J-V* curve, it can be concluded that there are
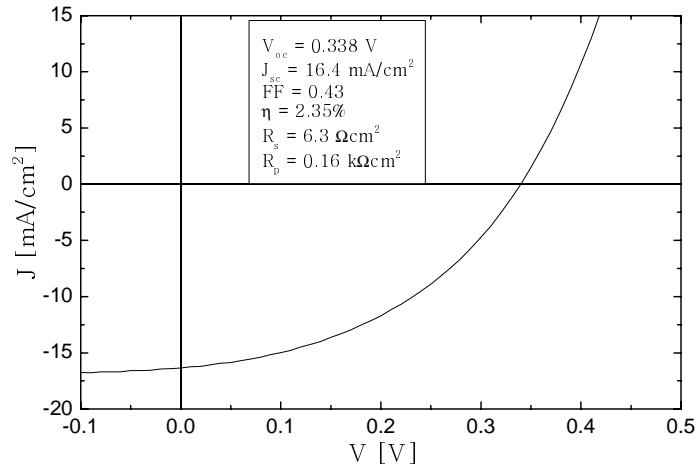
Figure 6.2 *J-V* curves of n-i-p solar cell with i-layer deposited using Ta filaments, measured under 100 mW/cm^2 illumination. Active cell area is 0.13 mm^2.
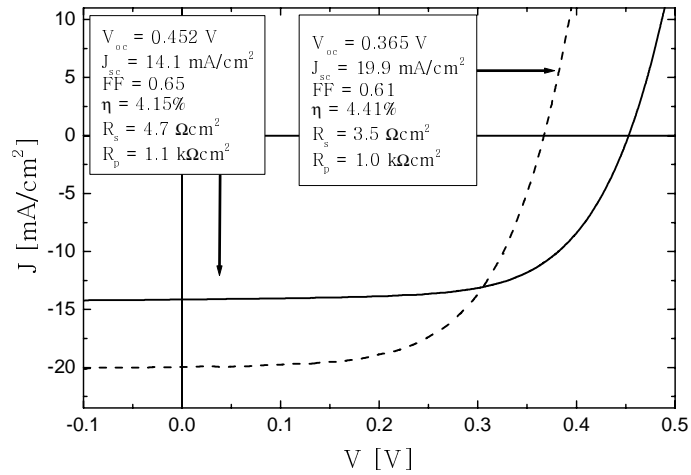

Figure 6.3 *J-V* curves of n-i-p solar cell with i-layer deposited using W filaments, measured under 100 mW/cm^2 illumination. Substrate temperature is 480°C (full line) [102] and 530°C (dashed line) [104]. Active cell area is 0.13 mm^2.
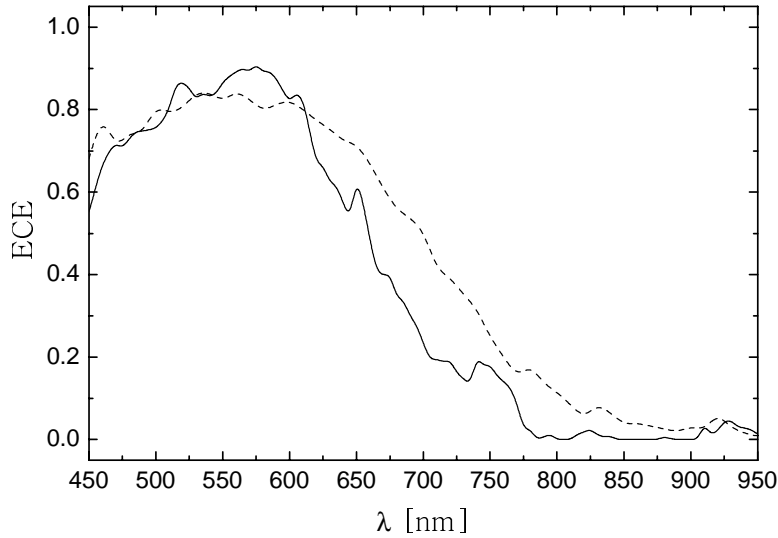
Figure 6.4 External collection efficiency (ECE) as function of wavelength of n-i-p solar cells with i-layer deposited using W filaments. Substrate temperature is 480°C (full line) and 530°C (dashed line). Active cell area is 0.13 mm^2.

considerable losses in the cell, primarily in V_{oc} and FF. The J_{sc} is good, while the parallel resistance is low and the series resistance is high.

Figure 6.3 shows the *J-V* characteristics of the cells with the i-layer deposited using W as filament material. The thickness of the i-layer of the cell deposited at 530°C was 1.22 µm, while the i-layer thickness of the cell deposited at 480°C was only about 600 nm. This difference in thickness is the main reason for the lower value of *J$_{sc}$* for the low temperature cell, compared to the high temperature cell. The spectral response of the cells (Figure 6.4) also indicates that the low temperature cell lacks carrier generation in the long-wavelength region ($\lambda > 650$ nm), which is related to the thickness difference. The most striking difference between the two cells cell is the difference in open circuit voltage. Lowering the substrate temperature leads to an increase in *V$_{oc}$* of more than 20%. This increase will be discussed below.
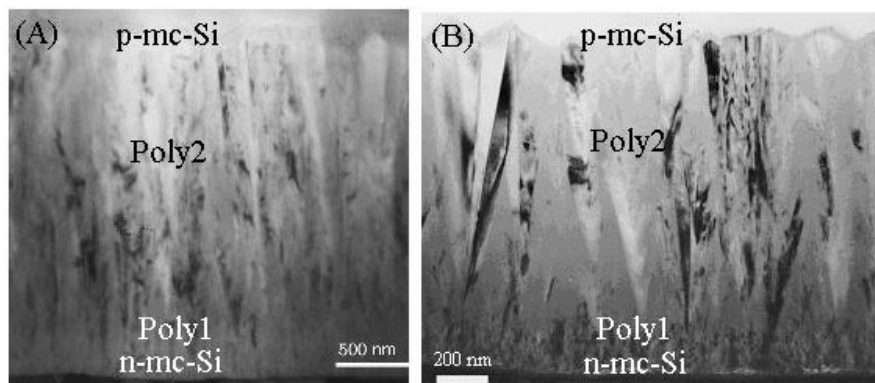
Figure 6.5 Cross-sectional transmission electron micrograph of n-i-p cell on stainless steel substrate. (A): substrate temperature 480°C, scale bar: 500 nm, note that the micrograph is taken at a *different spot* than the cell described in this section; (B): substrate temperature 530°C, scale bar: 200 nm.

6.3.1 Influence of substrate temperature on V_{oc}

It has been suggested that the increase in V_{oc} with decreasing substrate temperature is mainly a result of smaller i-layer thickness, since the open circuit voltage is a function of recombination. In a thin cell, there is less recombination due to a larger field [44]. However, Rath et al. reported on AMPS (Analysis of Microelectronic and Photonic Devices) simulations that showed that the influence of decreasing the i-layer thickness from 1.2 µm to 600 nm results in a maximal increase in V_{oc} of 0.01 V [105], which is much less than the increase observed in the cell deposited at 480°C, as compared to the cell deposited at 530°C.

Cross-sectional transmission electron microscopy studies of the cells have been performed to elucidate the difference in V_{oc}. Figure 6.5 shows the resulting micrographs. In first instance, the micrographs look the same. However, micrographs taken at larger magnification (Figure 6.6) show distinct cracks in the n-layer of the cell deposited at 530°C, parallel to the substrate. In the cell deposited at 480°C, these cracks are not observed. The presence of cracks may result in a decrease in V_{oc}. The origin of these cracks can be attributed to (1) stress introduced in the n-layer by the deposition of the i-layer and (2) interaction of Hot-Wire generated atomic hydrogen with the plasma-
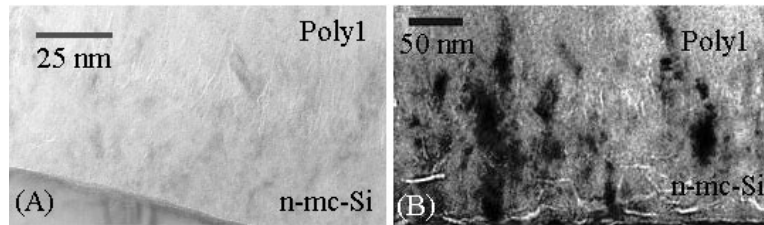
Figure 6.6 Cross-sectional transmission electron micrograph of n/i
interface. (A): substrate temperature: 480°C, scale bar: 25 nm; (B):
substrate temperature: 530°C, scale bar: 50 nm.

deposited n-layer. Stress in the n-layer can be introduced during the deposition
of the i-layer, since the deposition temperature of the i-layer (530°C) is larger
than that of the n-layer (250°C). The interaction of Hot-Wire generated atomic
hydrogen has been studied by van Veen et al. [106], using deuterated silane. It
was concluded that atomic deuterium (or hydrogen in the case of non-deuterated
silane) penetrates the n-layer. It is however unlikely that this effect is very
dependent on the substrate temperature, especially with a temperature difference
as little as 50°C. It can thus be concluded that the cracks visible in Figure 6.6(B)
originate from thermal stress.

Other possible reasons for the low V_{oc} for the solar cell deposited at a
substrate temperature of 530°C could be the highly defective Poly1 incubation
layer and the diffusion of metal atoms from the stainless steel substrate through
the n-layer. The Poly1 layer leads to recombination and, following AMPS
simulations, to a lower V_{oc} [105]. The diffusion of metal atoms (e.g. Fe, Cr, Mn)
into the cell can be inhibited by lowering of the substrate temperature and by
the incorporation of a buffer layer, e.g. ZnO.

Figure 6.7 nicely shows a very smooth i/p interface and the native
surface texture of Poly2.
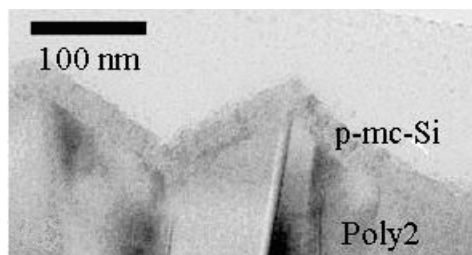
Figure 6.7 Cross-sectional transmission electron micrograph op i/p
interface of solar cell deposited at 530°C. Scale bar: 100 nm

6.4 Conclusions and perspectives

In this chapter, preliminary solar cell results were given. The highest efficiency obtained was 4.41% for an n-i-p cell on stainless steel, with the i-layer deposited by Hot-Wire CVD, using tungsten as filament material. The i-layer thickness of this cell was 1.22 μm and consisted of a profiled layer of Poly1 and Poly2. The doped layers have been deposited by PECVD. The relatively low value for the open circuit voltage of 0.365 V is probably due to cracks in the n-layer (T_{sub} = 250°C), due to thermal stress because of the high deposition temperature of the i-layer (T_{sub} = 530°C).

Recent solar cells made at a deposition temperature for the i-layer to 480°C, using tungsten as filament material, the open circuit voltage increased by more than 20%, to 0.452 V. Due to a much thinner i-layer (600 nm), the current of the cell was low. XTEM studies showed no cracks in the n-layer. It is expected that using a thicker i-layer can increase the short circuit current.

Incorporation of an i-layer deposited by Hot-wire CVD using tantalum as filament material thus far yielded an efficiency of 2.35%. This cell had a reasonable short circuit current (16.4 mA/cm^2), but low fill factor (0.43) and open circuit voltage (0.338 V). It is probably still possible to increase the efficiency of the cell by choosing another deposition regime (e.g. lower filament temperature).

There are a number of possibilities to increase the efficiency of the deposited cells. Firstly, a textured surface (i.e. Ag/textured ZnO) can be used as back reflector to increase the effective path length of the light, thus increasing the current. Furthermore, a temperature and/or Hot-Wire hydrogen resistant n-layer will lead to a higher value of the open circuit voltage. A possibility to deposit such a layer is by using PE-CVD at high temperature or Hot-Wire CVD. At this moment, studies into the deposition of n-layers by Hot-Wire CVD are performed at Utrecht University.

References

[1]   Nieuwsblad Stromen, **20**, 9 November 2001

[2]   R.E.I. Schropp, "Met Nieuwe Energie", oration at the Utrecht University, 28 May 2001

[3]   D.L. Staebler, C.R. Wronski, Appl. Phys. Lett. **31**, 292 (1977)

[4]   R.J. Koval, J. Koh, Z. Lu, L. Jiao, R.W. Collins, C.R. Wronski, Appl. Phys. Lett. **75**, 1553 (1999)

[5]   P. Roca i Cabarrocas, J. Non-Cryst. Sol. **266-269**, 31 (2000)

[6]   A.M. Brockhoff, Ph.D. thesis, Utrecht University (2001)

[7]   R.E.I Schropp, K.F. Feenstra, E.C. Molenbroek, H. Meiling, J.K. Rath, Phil. Mag. B **76-3**, 309 (1997)

[8]   R.E.I. Schropp, M. Zeman, "Amorphous and microcrystalline silicon solar cells, Modeling, Materials and Device Technology" Kluwer Academic Publishers (1998)

[9]   P. Müller, E. Conrad, T.R. Omstead, P. Kember, Conference Proceedings of the 13th European Photovoltaic Solar Energy Conference (1995), 1742

[10]   S. Koynov, S. Grebner, P. Radojkovic, E. Hartmann, R. Schwarz, L. Vasilev, R. Krankenhagen, I. Sieber, W. Henrion, M. Schmidt, J. Non-Cryst. Sol. **198-200** (1996) 1012

[11]   S. Hamma, P. Roca i Cabarrocas, J. Non-Cryst. Sol. **227-230** (1998) 852

[12]   H. Matsumura, A. Heya, R. Iizuka, A. Izumi, A.-Q. He, N. Otsuka, Mat. Res. Soc. Symp. Proc. **452** (1997) 983

[13]   D. Peiró, J. Bertomeu, C. Voz, J.M. Asensi, J. Puigdollers, J. Andreu, Conference Proceedings of the 14th European Photovoltaic Solar Energy Conference (1997), 1428

[14]   Q. Wang, E. Iwaniczko, A.H. Mahan, D.L. Williamson, Mat. Res. Soc. Symp. Proc. **507** (1998) 903

[15]   J.K. Rath, H. Meiling, R.E.I. Schropp, Jpn. J. Appl. Phys. **36** (1997) 3706

[16]   H.J. Wiesmann, A.K. Ghosh, T. McMahon, M. Strongin, J. Appl. Phys. **50** (1979) 3752

[17]   H.J. Wiesmann, US Patent 4 237 150, December 2, 1980

[18]   H. Matusmura, H. Tachibana, Appl. Phys. Lett. **47** (1985) 833

[19]   A.H. Mahan, J. Carapella, B.P. Nelson, R.S. Crandall, I. Balberg, J. Appl. Phys. **69** (1991) 6728

[20]   N. Honda, A. Masuda, H. Matsumura, J. Non-Cryst. Sol. **266-269** (2000) 100

[21]   K.F. Feenstra, Ph.D. thesis, Utrecht University (1998)

[22]   B. Stannowski, Ph.D. thesis, Utrecht University (2002)

[23]   A. Madan, P. Rava, R.E.I. Schropp, B. von Roedern, Appl. Surf. Sci. **70/71**, 716 (1993)

[24]   R.A.C.M.M. van Swaaij, Ph.D. thesis, Utrecht University (1994)

[25]   M.J. van den Boogaard, Ph.D. thesis, Utrecht University (1992)

[26]   E.H.C. Ullersma, Ph.D. thesis, Utrecht University (1998)

[27]   W.B. Jackson, N.M. Amer, A.C. Boccara, D. Fournier, Appl. Opt. **20** (1981) 1333

[28]   Z. Iqbal, S. Vijayalakshmi, H. Grebel, NanoStruc. Mat. **12** (1999) 271

[29]   M. Vaněček, A. Poruba, Z. Remeš. N. Beck, M. Neslădek, J. Non-Cryst. Sol. **227-230** (1998) 967

[30]   P. Brogueira, J. P. Conde, S. Arekat, V. Chu, J. Appl. Phys. **79-11** (1996) 8748

[31]   J.K. Rath, R.E.I. Schropp, W. Beyer, J. Non-Cryst. Sol. **266-269** (2000) 190

[32]   J. Meier, P. Torres, R. Platz, S. Dubail, U. Kroll, J.A. Anna Selvan, N. Pellaton Vaucher, Ch. Hoh, D. Fischer, H. Keppner, A. Shah, K.-D. Ufert, P. Giannoules, J. Koeler, in: M. Hack, E.A. Schiff, S. Wagner, R. Schropp, A. Matsuda (Eds.), Amorphous Silicon Technology, vol. **420** (1996) 879.

[33]   M.H. Brodsky, M. Cardona, J.J. Cuomo, Phys. Rev. B **16** (1977) 3556

[34]   N. Maley, Phys. Rev. B **46** (1992) 2078

[35]   J. A. Naber and D. P. Snowden, Rev. Sci. Instr **40** (9), 1137 (1969).

[36]   S. S. Collier, A. K. Weiss, and R. F. Reitehel, PhotoGraphic Sci. and Eng. **20** (2) 54-59 (1976).

[37]   J. M. Warman, M. P. de Haas, M. Grätzel, and P. P. Infelta, Nature **310**, 305 (1984).

[38]   M. Kunst and H. Tributsch, Chem. Phys. Lett. **105** (2), 123 (1984).

[39]   M. Kunst and G. Beck, J. Appl. Phys. **60** (10), 3558-66 (1986).

[40]   H. C. Neitzert, W. Hirsch, C. Swiatkowski, S. Schroetter, and M. Kunst, J. Non-Cryst. Solids **137-138** (Pt. 1), 487-490 (1991).

[41]   R. Brenot, P. Bulkin, P. Roca i Cabarrocas, B. Drevillon, and R. Vanderhaghen, J. Non-Cryst. Solids **230** (Part B), 1001-1005 (1998).

[42]   R. Brenot, R. Vanderhaghen, B. Drevillon, I. French, and P. Roca i Cabarrocas, Thin Solid Films **296** (1-2), 94-97 (1997).

[43]   J. Schmidt and A. G. Aberle, J. Appl. Phys. **81** (9), 6186-6199 (1997).

[44]   M.A. Green, Solar Cells, Prentice Hall (1992)

[45]   H. Matsumura, J. Appl. Phys. **65** (11), 4396 (1989)

[46]   H.L. Duan, G.A. Zaharias, S.F. Bent, Mat. Res. Soc. Symp. Proc. **664** (2001) A3.1.1

[47]   S. Morrison, A. Madan, Proc. of 17th EPVSEC (2001), to be published

[48]   J. Doyle, R. Robertson, G.H. Lin, M.Z. He, A. Gallagher, J. Appl. Phys. **64** (6) 3215 (1988)

[49]   C. Horbach, W. Beyer, H. Wagner, J. Non-Cryst. Sol. **137&138** (1991) 661

[50]   K. Tonokura, K. Inoue, M. Koshi, Thin Solid Films, in press

[51]   Y. Wang, R. Pollard, J. Electrochem. Soc. **142** (1995) 1712

[52]   K. Inoue, S. Tange, K. Tonokure, M. Koshi, Thin Solid Films **395** (2001) 42

[53]   H. Matsumura, Jpn. J. Appl. Phys. **37** (1998) 3175

[54]   H.L. Duan, G.A. Zaharias, S.F. Bent, Thin Solid Films **395** (2001) 36

[55]   E.C. Molenbroek, Ph.D.-thesis, University of Colorado (1995)

[56]   S. Sakai, J. Deisz, M.S. Gordon, J. Phys. Chem. **93** (1989) 1888

[57]   A. Gallagher, Thin Solid Films **395** (2001) 25

[58]   P. Ho, W.G. Breiland, R.J. Buss, J. Chem. Phys. **91** (1989) 2627

[59]   M. Hertl, J. Jolly, J. Phys. D: Appl. Phys. **33** (2000) 381

[60]   D.A. Doughty, J.R. Doyle, G.H. Lin, A. Gallagher, J. Appl. Phys. **67** (1990) 6220

[61]   A. Matsuda, T. Goto, Mater. Res. Soc. Symp. Proc. **164** (1990) 3

[62]   W.M.M. Kessels, M.C.M. van de Sanden, R.J. Severens, D.C. Schram, J. Appl. Phys. **87** (2000) 3313

[63]   E.A.G. Hamers, A. Fontcuberta i Morral, C. Niikura, R. Brenot, P. Roca i Cabaroccas, J. Appl. Phys. **88** (2000) 3674

[64]   E.A.G. Hamers, W.G.J.H.M. van Sark, J. Bezemer, H. Meiling, W.F. van der Weg, J. Non-Cryst. Sol. **26** (1998) 205

[65]   P. Roca i Cabaroccas, P. Morin, V. Chu, J. Conde, J.Z. Liu, H.R. Park, S. Wagner, J. Appl. Phys. **69** (1991) 2942

[66]   A. Matsuda, K. Kumagai, K. Tanaka, Jpn. J. Appl. Phys. **22** (1983) L-34

[67]   Y. Nozaki, K. Kongo, T. Miyazaki, M. Kitazoe, K. Horii, H. Umemoto, A. Masuda, H. Matsumura, J. Appl. Phys. **88** (2000) 5437

[68]   C.M.H. van der Werf, private communications

[69]   K.M.H. Maessen, Ph.D.-thesis, Rijksuniversiteit Utrecht (1988)

[70]   H. Matsumura, A. Masuda, A. Izumi, Mat. Res. Soc. Symp. Proc. **557** (1999) 67

[71]   A.H. Mahan, A. Mason, B.P. Nelson, A.C. Gallagher, Mat. Res. Soc. Symp. Proc. **609** (2001) A6.6.1

[72]   P.A.T.T. van Veenendaal, O.L.J. Gijzeman, J.K. Rath, R.E.I. Schropp, Thin Solid Films **395** (2001) 194

[73]   P.A.T.T. van Veenendaal, J.K. Rath, O.L.J. Gijzeman, R.E.I. Schropp, Polycrystalline Semiconductors VI - bulk materials, thin films, and devices, in: O. Bonnaud, T. Mohammed-Brahim, H.P. Strunk, J.H. Werner (Eds.), Series 'Solid State Phenomena', Scitech Publ., Uettikon am See, Switzerland (2001) 53

[74]   H.L. Duan, G.A. Zaharias, S.F. Bent, to be published in Mat. Res. Soc. Symp. Proc. **715**

[75]   Scientific Group Thermodata Europe, www.sgte.org

[76]   W. Ruihua, L. Zhiqiang, L. Li, L. Jahe, Sol. Energy Mater. Sol. Cells **62** (2000) 193

[77]   A. Rothen, Rev. Sci. Instr. **16** (1945) 26

[78]   R.M.A. Azzam, N.M. Bashara, Ellipsometry and polarized light, North Holland Personal Library, Elsevier Science B.V. (1987)

[79]   H.G. Tompkins, A User's Guide to Ellipsometry, Academic Press (1992)

[80]   L.C. Jacobs, private communications

[81]   R.W. Collins, Appl. Phys. Lett. **48-13** (1986) 843

[82]   R.O. Dusane, S. Bauer, B. Schröder, H. Oechsner, Thin Solid Films **395** (2001) 121

[83]   D.A.G. Bruggeman, Ann. Phys. **24** (1935) 636

[84]   J.A. Rice, Mathematical Statistics and Data Analysis, Duxbury Press (1995)

[85]   B Drévillon, Prog. Cryst. Growth Charact. **27** (1993) 1

[86]   R.W. Collins, J.M. Cavese, J. Non-Cryst. Sol. **97-98** (1989) 269

[87]   A. Canillas, E. Bertram, J.L. Andújar, B. Drévillon, J. Appl. Phys. **68** (1990) 2752

[88]   J.K. Rath, M. Galetto, C.H.M. van der Werf, K.F. Feenstra, H. Meiling, M.W.M. van Cleef, R.E.I. Schropp, Technical Digest Int. PVSC-9 Conf., Miyazaki, Japan (1996) 227

[89]   J.K. Rath, K.F. Feenstra, D. Ruff, H. Meiling, R.E.I. Schropp, Mat. Res. Soc. Symp. Proc. **452** (1996) 977

[90]   J.K. Rath, F.D. Tichelaar, H. Meiling, R.E.I. Schropp, Mat. Res. Soc. Symp. Proc. **507** (1998) 879

[91]   T. Saitoh, H. Hiraki, Jpn. J. Appl. Phys. **24** (1985) L491

[92]   U. Kroll, J. Meier, A. Shah, S. Mikhailov, J. Weber, J. Appl. Phys. **80** (1996) 4971

[93]   D. Stryahilev, F. Diehl, B. Schroeder, J. Non-Cryst. Sol. **266-269** (2000) 166

[94]   J.K. Rath, F.D. Tichelaar, R.E.I. Schropp, Sol. State Phen. **67-68** (1998) 465

[95]   M.A. Green, private communications

[96]   F. Diehl, B. Schröder, H. Oechser, Mat. Res. Soc. Symp. Proc. **507** (1998) 819

[97]   P.A.T.T. van Veenendaal, J.K. Rath, R.E.I. Schropp, Proceedings of the 16th European Photovoltaic Solar Energy Conference (2000) 458

[98]   G.D. Cody, J. Non-Cryst. Sol. **141** (1992) 3

[99]   P.A.T.T. van Veenendaal, T.J. Savenije, J.K. Rath, R.E.I. Schropp, Thin Solid Films **403-404** (2002) 175-178

[100]   T.J. Savenije, P.A.T.T. van Veenendaal, M.P. de Haas, J.M. Warman, R.E.I. Schropp, J. Appl. Phys. **91-9** (2002) 5671

[101]   R. Vanderhaghen, private communications

[102]   P.A.T.T. van Veenendaal, C.M.H. van der Werf, J.K. Rath, R.E.I. Schropp, J. Non-Cryst. Sol. **299-302** (2002) 1184

[103]   C.E. Nebel, R.A. Street, W.B. Jackson, N.M. Johnson, J. Non-Cryst. Sol. **164-166** (1993) 203

[104]   J.K. Rath, A.J.M.M. van Zutphen, H. Meiling, R.E.I. Schropp, Mat. Res. Soc. Symp. Proc. **467** (1997) 445

[105]   J.K. Rath, F.A. Rubinelli, M. van Veghel, C.H.M. van der Werf, Z. Hartman, R.E.I. Schropp, 16th EPVSEC (2000) 462

[106]   M.K. van Veen, RE.I. Schropp, Thin Solid Films **403-404** (2002) 135

Summary

Over the past decade, an increase in the effort to investigate the use of renewable energy sources, such as wind, geothermal, tidal and solar energy, has occurred. Despite the environmental advantages, at present, the contribution of these sources to the total energy consumption remains small. The direct conversion of solar energy into electricity through photovoltaic (PV) solar cells is one of the most promising techniques, due to the abundance of solar energy reaching the surface of the earth. The use of photovoltaic solar cells is limited by the high cost of electricity produced by solar cells compared to electricity produced from fossil fuels. The major contributions to the cost of solar cells are the material and manufacturing costs. Therefore, over the past decades, the development of silicon based thin film solar cells has received much attention, because the fabrication costs are low.

A promising material to be used in thin film solar cells is polycrystalline silicon (poly-Si:H), since this material does not degrade when exposed to light. This so-called Staebler-Wronski effect (light-induced degradation) is the main disadvantage of amorphous silicon. Poly-Si:H can be deposited by a wide spectrum of chemical vapor deposition techniques.

A relatively new technique to deposit poly-Si:H is Hot-Wire Chemical Vapor Deposition (Hot-Wire CVD). In Hot-Wire CVD, the reactant gases are catalytically decomposed at the surface of a hot filament. The filament materials used most widely at present are tungsten (W) and tantalum (Ta). The main advantages of Hot-Wire CVD over PE-CVD, which is currently the most widespread applied technique to deposit thin silicon films in industry, are (i) absence of ion bombardment, (ii) high deposition rate, (iii) low equipment cost and (iv) high gas utilization. Possible issues in Hot-Wire CVD are the control of the substrate temperature and aging of the filaments.

This thesis deals with the full spectrum of deposition, characterization and application of polycrystalline silicon thin films, i.e. from the gas molecule to solar cell.

In Chapter 2, the used deposition systems and the characterization techniques are described.

Chapter 3 gives an overview of studies regarding the different steps in the deposition and growth of silicon thin films in Hot-Wire CVD. Studies on the decomposition of silane on the filament showed that the process is catalytic of nature and that at filament temperature above 1800°C, silane is decomposed into Si and 4H. The dominant gas phase reactions are the reaction of Si and H with silane, resulting in SiH_3, Si_2H_6, Si_3H_6 and H_2SiSiH_2. The precursors dominating the film growth are Si, SiH_3 and Si_2H_4, depending on pressure and filament temperature. Also in this chapter, X-ray photoelectron spectroscopy (XPS) results on tantalum and tungsten filaments used during the deposition of thin film poly-Si:H were discussed. The position dependent measurements show larger silicon contents at the ends of the tungsten filament, as compared to the middle, due to a lower filament temperature. The difference in silicon content between the middle and edge of the tantalum filament is insignificant. Deposition time dependent measurements show an increase in silicon content of the tungsten filament with time, while the silicon content on the tantalum filament saturates rather quickly. Two processes are suggested: (1) the catalytic dissociation of the reactant gases is different at a tantalum as opposed to a tungsten surface, and (2) the formation of a silicide-like alloy is inhibited more on the surface of the tantalum filament than on a tungsten filament.

In Chapter 4, the deposition of polycrystalline silicon layers by Hot-Wire CVD using tantalum as filament material has been investigated using spectroscopic and kinetic ellipsometry. The spectroscopic ellipsometry data was fitted using a three-layer model. Spectroscopic ellipsometry studies on a series of films deposited at increasing hydrogen dilution revealed that the crystallinity of the layers increased, as was also found by Raman spectroscopy. The deposition of profiled layers, using a highly crystalline seed layer was studied by both spectroscopic and kinetic ellipsometry. Both studies showed that by using a seed layer, deposited at high hydrogen dilution, layers with a higher crystalline volume fraction could be deposited using a high silane flow, which normally leads to amorphous silicon layers.

Polycrystalline silicon thin films deposited using tungsten, tantalum and rhenium as filament material, are characterized in Chapter 5. "Device-quality" polycrystalline layers have been deposited using tungsten as filament material. The materials deposited using tantalum and rhenium at the filament temperatures investigated, showed properties that are less than "device-quality", mostly due to the presence of a significant amount of amorphous tissue.

Finally, in Chapter 6, preliminary solar cell results are given. The highest efficiency obtained was 4.41% for a n-i-p solar cell with a thickness <1.5 μm. on stainless steel without the use of a back reflector. Approaches to

increase the solar cell performance are (i) using a lower substrate temperature, thus increasing the open circuit voltage, (ii) incorporating a textured back reflector (e.g. ZnO/Ag) to inhibit metal diffusion from the stainless steel into the cell and increasing the effective pathway of the light, resulting in a higher current and (iii) by using a more stable n-layer, which can be deposited by Hot-Wire CVD.

Samenvatting

In de loop van het afgelopen decennium is de inspanning om duurzame energiebronnen, zoals wind, geothermisch, getijde en zonne-energie, te onderzoeken toegenomen. De bijdrage van deze duurzame energiebronnen aan de totale energie consumptie blijft echter miniem, ondanks de voordelen voor het milieu. De omzetting van zonne-energie in elektriciteit met behulp van photovoltaïsche (PV) zonnecellen is een van de meest belovende technieken, doordat er een overvloed aan zonne-energie het oppervlak van de aarde bereikt. Het gebruik van zonnecellen wordt beperkt door de hoge kosten van elektriciteit, opgewekt met zonnecellen, vergeleken met elektriciteit opgewekt uit fossiele brandstoffen. De belangrijkste bijdragen in deze hoge kosten zijn het gebruikte materiaal en de fabricagekosten. Vandaar dat gedurende de afgelopen decennia de ontwikkeling van dunne film silicium zonnecellen, waarbij de fabricagekosten laag zijn, veel aandacht heeft gekregen.

Een veelbelovend materiaal voor gebruik in dunne film zonnecellen is polykristallijn silicium (poly-Si:H), omdat dit materiaal niet degradeert als het wordt blootgesteld aan licht. Dit zogenaamde Staebler-Wronski effect is het voornaamste nadeel van amorf silicium. Poly-Si:H kan gedeponeerd worden met een wijd scala aan technieken waarbij het materiaal wordt gevormd door chemische vorming uit damp.

Een relatief nieuwe methode om poly-Si:H te deponeren is Hot-Wire Chemical Vapor Deposition of chemische vorming uit damp met behulp van een hete draad (Hot-Wire CVD). Bij Hot-Wire CVD worden de gebruikte gassen katalytisch ontleed aan het oppervlak van een hete draad. De meest toegepaste draadmaterialen zijn wolfraam (W) en tantaal (Ta). De grootste voordelen van Hot-Wire- CVD, vergeleken met de momenteel in de industrie meest toegepaste techniek om dunne film silicium films te deponeren, PE-CVD, zijn (i) het niet optreden van een ionenbombardement, (ii) hoge depositie snelheid, (iii) lage kosten voor depositie apparatuur en (iv) efficiënt

gasverbruik. Mogelijke vraagstukken aangaande Hot-Wire CVD zijn de controle van de substraattemperatuur en het verouderen van de draden.

In dit proefschrift wordt het gehele spectrum van depositie, karakterisering en toepassing van polykristallijn silicium dunne films behandeld, oftewel van gasmolecule tot zonnecel.

In Hoofdstuk 2 worden de gebruikte depositiesystemen en karakterisatie technieken beschreven.

Hoofdstuk 3 geeft een overzicht van studies naar de verschillende stappen in de depositie en groei van silicium dunne lagen met behulp van Hot-Wire CVD. Studies naar de ontleding van silaan aan een hete draad hebben aangetoond dat het proces katalytisch is en dat bij filament temperaturen hoger dan 1800°C, silaan ontleedt in Si en 4H. De overheersende gasfasereacties zijn de reacties van Si en H met silaan, resulterend in SiH_3, Si_2H_6, Si_3H_6 en H_2SiSiH_2. De dominerende radicalen voor filmgroei zijn Si, SiH_3 en Si_2H_4, afhankelijk van druk en filamenttemperatuur. Tevens worden in dit hoofdstuk resultaten van XPS metingen aan tantaal en wolfraam draden, die gebruikt zijn tijdens de depositie van dunne film poly-Si:H, behandeld. De metingen toonden een hoger silicium gehalte aan de uiteinden van de wolfraam draden, in vergelijking tot het midden, veroorzaakt door een lagere filamenttemperatuur. Het verschil in silicium gehalte tussen het midden en de uiteinden van de tantaal draden is gering. Metingen als functie van de depositietijd tonen een tijdsafhankelijke toename van het silicium gehalte bij wolfraam draden, terwijl het silicium gehalte bij tantaal draden snel verzadigt. Twee mogelijke processen zijn geopperd: (1) de katalytische ontleding van de gebruikte gassen verloopt anders op een tantaal dan op een wolfraam oppervlak, en (2) de vorming van een silicide-achtige verbinding wordt meer belemmerd op een tantaal, dan op een wolfraam oppervlak.

In Hoofdstuk 4 wordt de depositie van polykristallijn silicium lagen met behulp van Hot-Wire CVD, gebruikmakend van tantaal als draadmateriaal, onderzocht met behulp van spectroscopische en kinetische ellipsometrie. De resultaten van de spectroscopische ellipsometrie zijn gefit met een drie-lagen model. Spectroscopische ellipsometrie metingen aan een reeks films lieten zien dat de kristalliniteit van de lagen toeneemt met toenemende waterstofverdunning, wat ook volgde uit Raman spectroscopie. De depositie van geprofileerde lagen, waarbij een kiemlaag met hoge kristalliniteit wordt gebruikt, is bestudeerd met zowel spectroscopische als kinetische ellipsometrie. Uit beide studies volgt dat met behulp van deze kiemlaag, kristallijnere lagen kunnen worden gedeponeerd onder depositiecondities welke normaliter resulteren in amorfe lagen.

De karakterisatie van polykristallijne silicium dunne films gedeponeerd met wolfraam, tantaal en rhenium als filamentmateriaal, wordt behandeld in

Hoofdstuk 5. "Device-quality" polykristallijne lagen zijn gedeponeerd met wolfraam als filamentmateriaal. De materialen die zijn gedeponeerd met tantaal en rhenium filamenten hebben, bij de gebruikte draadtemperaturen, eigenschappen die niet voldoen aan de "device-quality"-maatstaf, veelal door de aanwezigheid van een significante hoeveelheid amorf materiaal.

Tenslotte worden in Hoofdstuk 6 de resultaten van enkele voorlopige zonnecellen gegeven. Het hoogste rendement dat is bereikt was 4.41% voor een n-i-p zonnecel met een dikte van minder dan 1.5 µm, zonder gebruikmaking van een reflecterend substraat. Een toename in de prestatie van de zonnecel kan worden bereikt door (i) gebruik te maken van lagere substraattemperaturen om de open-klem-spanning te vergroten, (ii) toepassing van een getextureerd reflecterend substraat (bijv. ZnO/Ag) om de diffusie van metalen uit het roestvast stalen substraat in de zonnecel tegen te gaan en voor het vergroten van de effectieve lichtweg, wat resulteert in een hogere stroom en (iii) het gebruik van een stabielere n-laag, die gedeponeerd kan worden met behulp van Hot-Wire CVD.

List of publications

P.A.T.T. van Veenendaal, J.K. Rath, R.E.I. Schropp, "Origin of enhanced absorption coefficient in HWCVD poly-Si:H films", Proceedings of the 16th European Solar Energy Conference (2000) 458

P.A.T.T. van Veenendaal, J.K. Rath, O.L.J. Gijzeman, R.E.I. Schropp, "The influence of the use of different catalysers in Hot Wire CVD for the deposition of polycrystalline silicon thin films", Polycrystalline Semiconductors VI – Materials, Technologies, and Large Area Electonics, in: O. Bonnaud, T. Mohammed-Brahim, H.P. Strunk, J.H. Werner (Eds.), Series 'Solid State Phenomena' **80-81**, 53 (2001), Scitech Publ., Uettikon am See, Switzerland

P.A.T.T. van Veenendaal, O.L.J. Gijzeman, J.K. Rath, R.E.I. Schropp, "The influence of different catalysers in Hot Wire CVD for the deposition of polycrystalline silicon thin films", Thin Solid Films **395**, 194 (2001)

P.A.T.T. van Veenendaal, T.J. Savenije, J.K. Rath, R.E.I. Schropp, "Microwave mobility in profiled poly-Si thin films deposited on glass by Hot-Wire CVD", Thin Solid Films **403-404** (2002) 175

P.A.T.T. van Veenendaal, C.M.H. van der Werf, J.K. Rath, R.E.I. Schropp, "Influence of grain environment on open circuit voltage of hot-wire chemical vapour deposited Si:H solar cells", J. Non-Cryst. Sol. **299-302** (2002) 1184

P.A.T.T. van Veenendaal, R.E.I. Schropp, "Processes in silicon deposition by Hot-Wire Chemical Vapor Deposition", to be published in Current Opinion in Solid State and Materials Science **6** (2002).

P.A.T.T. van Veenendaal. G.W.M. van der Mark, J.K. Rath, R.E.I. Schropp, "Spectroscopic ellipsometry studies of Hot-Wire deposited polycrystalline silicon on glass", submitted to Thin Solid Films.

R.E.I. Schropp, B. Stannowski, A.M. Brockhoff, P.A.T.T. van Veenendaal, J.K. Rath, "Hot Wire CVD polycrystalline silicon semiconducting thin films for application in thin film transistors and solar cells", Mater. Phys. Mech. **1**(2), (2000) 73.

J.K. Rath, B. Stannowski, P.A.T.T. van Veenendaal, M.K. van Veen, R.E.I. Schropp, "Application of hot-wire chemical vapor-deposited Si:H films in thin film transistors and solar cells", Thin Solid Films **395**, 320 (2001)

R.E.I. Schropp, C.H.M. van der Werf, M.K. van Veen, P.A.T.T. van Veenendaal, R. Jiminez, Z. Hartman, J. Löffler, J.K. Rath, "Thin film a-Si/poly-Si multibandgap tandem solar cells with both absorber layers deposited by hot wire CVD", Mat. Res. Soc. Symp. Proc. **664** (2001) A15.6.1

M.K. van Veen, P.A.T.T. van Veenendaal, C.H.M. van der Werf, J.K. Rath, R.E.I. Schropp, "a-Si:H/poly-Si tandem cells deposited by Hot-Wire CVD", J. Non-Cryst. Sol. **299-302** (2002) 1194

T.J. Savenije, P.A.T.T. van Veenendaal. M.P. de Haas, J.M. Warman, R.E.I. Schropp, "Spatially resolved photoconductive properties of profiled polycrystalline silicon thin films", J. Appl. Phys. **91** (2002) 5671

C.H.M. van der Werf, A.J. Hardeman, P.A.T.T. van Veenendaal, M.K. van Veen, J.K. Rath, R.E.I. Schropp, "Investigation of scaling-up issues in hot-wire CVD of polycrystalline silicon", to be published in Thin Solid Films

C.H.M. van der Werf, P.A.T.T. van Veenendaal, M.K. van Veen, A.J. Hardeman, M.Y.S. Rusche, J.K. Rath, R.E.I. Schropp, "The influence of the feedstock gas on the filament temperature in Hot-Wire CVD", submitted to Thin Solid Films.

Dankwoord

Wie had ruim vier geleden gedacht dat ik als vreemde eend in de bijt (meer chemicus dan fysicus, Ir. in plaats van Drs. en Junior Onderzoeker) nog eens een boekje zou schrijven? Ik in ieder geval niet. Toch is het gelukt, met dank aan de volgende mensen…

Mijn promotor, Ruud Schropp, wil ik bedanken voor de inspanningen die hij heeft geleverd om mij te transformeren van projectmedewerker tot promovendus, zowel letterlijk als figuurlijk. Verder wil ik hem danken voor de vrijheid die hij mij geboden heeft om mijn onderzoek in te richten, hetgeen geresulteerd heeft in een grote diversiteit. Mijn co-promotor, Jatindra Rath, wil ik bedanken voor de dagelijkse begeleiding. Zijn kennis van poly-Si is ongeëvenaard. Frans Habraken, Richard van de Sanden (ETP, TUEindhoven) en Alfons van Blaaderen (SCM, Universiteit Utrecht) dank ik voor het kritisch lezen van mijn manuscript. De theoretische kijk van Ernst van Faassen zorgde ervoor dat ik altijd mijn ogen openhield tijdens het fitten van ellipsometrie-data. De Nederlandse Organisatie voor Energie en Milieu (NOVEM), en in het bijzonder Frank Witte, wil ik bedanken voor de financiële ondersteuning.

Onderzoek doen als promovendus doe je niet alleen! Karine van der Werf wil ik bedanken voor het groeien van talloze laagjes in de PASTA. Haar kennis van silicium gaat een 'nederige' technicus ver te boven. De beste manier om een opstelling te leren kennen is door haar uit elkaar te halen. Gerard van der Mark vond het niet erg dat ik dit bij de ATLAS in de praktijk bracht; destructief onderzoek blijft toch boeiend... Samen met Wim de Kruif deelde ik de verantwoordelijkheid voor de RT-opstelling, de meest overgedimensioneerde opstelling van de vakgroep: wat een monochromator! Ik twijfel er overigens niet aan dat wij in Ruurd Lof de ideale opvolger voor Wim hebben gevonden. Meestal wisten Gert Hartman, Jochen Löffler of Raul Jimenez Zambrano tijd te maken om mijn cellen te bedekken met een laagje ITO. Jullie zorgden ervoor dat mijn nipjes ook echte zonnecellen werden, al had ik wel gouden snelwegen

nodig om ze te laten werken. Voor SEM of TEM plaatjes kon ik terecht bij Pim van Maurik (Cel Biologie, Universiteit Utrecht) en Frans Tichelaar (National Center for HREM, TUDelft), terwijl Liesbeth van Steensel (PCI, Universiteit Utrecht) met veel enthousiasme AFM plaatjes maakte. XPS metingen zijn uitgevoerd door Ad Mens (ICC, Universiteit Utrecht), die tussen heftige katalytische reacties door naar Si speurde op mijn Ta en W filamenten. Het tactisch en strategisch inzicht van Onno Gijzeman (ICC, Universiteit Utrecht) zorgde ervoor dat de juiste draden werden onderzocht. Verder ben ik blij dat er glühwein wordt geschonken op de Quantsol conferentie; het leverde fantastische TRMC metingen op met Tom Savenije (RC, IRI, TUDelft). Raman metingen zijn uitgevoerd door Harry Donker (TAC, TUDelft), Aad Gordijn en Sander Hardeman. 'Mijn' student Sander, ook al kwam je voor mij eigenlijk op een te laat tijdstip en zijn je resultaten hier niet opgenomen, je hebt jouw onderzoek grondig en doeltreffend aangepakt.

Je voudrais remercier Pere Roca i Cabaroccas de me donner l'occasion d'apprendre les détails sur l'ellipsometry pendant mon séjour de 4 semaines au Laboratoire de Physique des Interfaces et des Couches Minces (LPICM) de l'Ecole Polytechnique à Palaiseau. En outre, je voudrais remercier tous autres membres de LPICM, particulièrement Jean-Eric Bourée et Régis Vanderhaghen pour la discussion fécond et mes camarades de chambre: Anna, Billel, Chisato et Régis pour l'atmosphère plaisante.

Verder wil ik de rest van de Hot-Wire club (Anke, Bernd en Marieke) bedanken voor de nuttige discussies. Mijn buurmeisje Anke had altijd de (surrogaat-)thee klaar. Bernd, Duitse degelijkheid is een positieve eigenschap. Marieke, met jouw onverzettelijkheid komt die poly-Si/a-Si tandem er heus wel. Luc Jacobs zorgde ervoor dat we naast keepen (TUB-PCM) nog een gemeenschappelijke interesse kregen: ellipsometrie. Hij heeft mij de basiskennis bijgebracht, al is 3 weken wel erg kort. Met Aad en Jochen was het plezierig werken aan en discussiëren over de ellipsometer als ATLAS-familie. Ervaring met de ellipsometer heb ik opgedaan tijdens de vele metingen voor Arja.

Riny, samen met jouw 'heksenkring' gaf je mij de mogelijkheid om mijn bijnaam als 'Het Orakel' in ere te houden. Staat die E nou echt voor Eucalypta?

Een belangrijke plaats binnen de vakgroep (en in ieder geval voor het verbeteren van mijn financiële situatie) was Café OL060, later verhuisd naar RvdG106B. Frank Achten liet mij de koelkast na toen hij uitvloog, waarvoor mijn dank. Ondanks dat niet iedereen het eens was met de monopoliepositie en het aantal dB's van het Café, was het er een komen en gaan van (stam-)gasten. De mooiste, wildste en meest ongeloofwaardige verhalen in het Café kwamen van 'vluchteling' Gijs, op de voet gevolgd door mede-loser Harald en blaataap

Juriaan. Als uitbater van het Café wil ik Aad, Bas, Bernd, Edwin, Jeroen F, Jochen, Luc, Tonnis en alle andere klanten bedanken voor de klandizie en het geleuter. RvdG106B was niet alleen uniek door het Café. Het was ook de enige kamer waar de saamhorigheid van S.I.D. naar voren kwam, gesymboliseerd door de blauwe en rode stoel. Jeroen, als eigenaar van de rode stoel bleef je interesse houden in de blauwe kant van de groep. Ondanks enkele zakelijke geschillen (is 0,05 prijsstijging in 3 jaar echt zo veel?) en een soms afwijkende wetenschappelijke visie, heb je me laten zien hoe je dingen wel of juist niet moet doen. Dank ook voor jouw bijdrage aan het Café in de vorm van de nodige entertainment. Verder wil ik al mijn overige (oud-)collega's bedanken voor de plezierige werksfeer, waarbij ik oprecht hoop dat er meer blauw-rode kamers zullen komen..

Verder wil ik alle aio's, postdocs en andere aanverwante artikelen bedanken voor de discussies en gezelligheid tijdens conferenties en workshops in Barcelona, Denver, Glasgow, Nice, St.Malo en Straatsburg.

Mijn oud-AZU-collega's Frank en Stephan mogen hier niet ontbreken. Frank, ons e-mail contact liet mij inzien dat de term 'stuk gaan' een relatief begrip is. Voor mijn fietsmaatje en medetrompettist Stephan: die 72 uur wachten in 3½ jaar is ruimschoots goedgemaakt door 25.000 km fietsen van Schalkwijk naar de Uithof en goede gesprekken over sociale, economische, politieke, milieugerelateerde, muzikale en andere 'belangrijke' onderwerpen.

Alex en Zoebaida, de etentjes met een hoog botte Delftenaren gehalte en oude koeien als TLJ en de staafmixer waren OK!

Ondanks dat ik vanwege een 'skiduim' mijn keepercarrière heb moeten beëindigen, wil ik V.V.Schalkwijk 4 bedanken voor de broodnodige verbale, fysieke en mentale uitspattingen. Het organiseren van een verdediging heeft wel wat weg van het schrijven van een boekje…

Bij Fanfare St. Caecilia Schalkwijk en dweilorkest SchOr kon ik altijd 'uitblazen'. Ik wil vooral de leden met wie ik heb samengewerkt in het bestuur en de M.C. bedanken en natuurlijk mijn medetrompettisten. Voor de 'trillipbrigade': het wordt weer tijd voor een Play-In!

Mijn ouders hebben het mogelijk gemaakt dat ik altijd mijn eigen weg kon gaan. Ik wil hen, samen met mijn zus, bedanken voor de belangstelling voor mijn onderzoek en hun niet aflatende steun.

Mijn lieve blauwogige gifmengstertje Jessica wil ik bedanken voor het fantastische afgelopen jaar; waar muziek maken al niet toe kan leiden. Na het slopen van mijn betonnen bunker heb je me de andere belangrijke dingen in het leven laten zien.

Groetjes, Patrick

Curriculum vitae

Patrick Adrianus Thomas Theodorus van Veenendaal werd op 11 november 1973 geboren te Schalkwijk (Utr.). Na het doorlopen van het St. Bonifatius College te Utrecht, studeerde hij vanaf 1992 Materiaalkunde aan de Technische Universiteit Delft. Tijdens zijn studie liep hij gedurende 3 maanden stage bij groep Laser Material Processing van Philips CFT te Eindhoven, waar hij werkte aan het laser-sinteren van keramische coatings op plastics. Na deze stage begon hij met zijn afstudeeronderzoek bij de vakgroep Toegepaste Anorganische Chemie. Zijn afstudeeronderwerp betrof de depositie van nanogestructureerde silicium deeltjes met behulp van laser-CVD en in-situ Raman spectroscopy tijdens die depositie. Hij studeerde af op 11 november 1997 en de ingenieurstitel werd behaald op 9 december 1997.

Hierna werkte hij gedurende drie maanden als stagiaire met behoud van uitkering op de afdeling Nucleaire Geneeskunde van het Academisch Ziekenhuis Utrecht, alwaar hij zich bezig heeft gehouden met het vergroten van de kennis van neutron- en foton-bestraalde organisch weefsels en de karakterisatie van holmium-gelabelde microsferen voor de behandeling van lever metastasen.

In mei 1998 trad hij in dienst als Junior Onderzoeker bij de sectie Grenslaagfysica van het Debye Instituut van de Universiteit Utrecht. Hij heeft daar gedurende 4½ jaar onderzoek gedaan aan dunne film polykristallijn silicium gedeponeerd met behulp van Hot-Wire CVD. Dit onderzoek werd gefinancierd door de Nederlandse Organisatie voor Energie en Milieu (NOVEM). De resultaten van het verrichte onderzoek staan beschreven in dit proefschrift. In september 2001 heeft hij een maand onderzoek gedaan bij de groep Physique des Interfaces et des Couches Minces van de Ecole Polytechnique te Palaiseau (Fr.).